TECHNISCHE UNIVERSITÄT MÜNCHEN

Lehrstuhl für Physikalische Chemie

The development of a state-of-the-art experimental setup demonstrated by the investigation of fuel cell reactions in alkaline electrolyte

Gustav Karl Henrik Wiberg

Vollständiger Abdruck der von der Fakultät für Chemie der Technischen Universität München zur Erlangung des akademischen Grades eines

Doktors der Naturwissenschaften

genehmigten Dissertation.

Vorsitzender: Univ.-Prof. Dr. W. Domcke

Prüfer der Dissertation:

       1. Univ.-Prof. Dr. U. K. Heiz
       2. Univ.-Prof. Dr. K. –O. Hinrichsen
       3. Prof. Dr. M. Arenz, University of Copenhagen / Dänemark

Die Dissertation wurde am 25.08.2010 bei der Technischen Universität München eingereicht und durch die Fakultät für Chemie am 04.10.2010 angenommen.

For my mother, Ingrid Wiberg (1947-1999)

Table of Contents

List of Figures

List of Tables

1 Introduction

In the last few decades, an increased environmental awareness and escalating energy demand have more recently led focus towards utilising alternative energy devices such as chemical-electrical energy converters (CEECs). For instance electrolyser CEECs could one day be used to enable energy buffering capabilities to environmentally friendly resources such as solar plants and wind turbines. In such a scenario, energy is converted to and stored in the form of hydrogen outside peak energy consumption, and then consumed using another CEEC, the fuel cell, when required. A particularly valuable application of the fuel cell CEEC is in the transport sector, wherein the emission of the greenhouse gas, CO_2, is considerable. By replacing conventional internal combustion engines with fuel cell technologies operating from hydrogen fuel and the oxygen in air yielding water, an improved fuel-to-wheel energy efficiency could significantly aid in reducing overall transport CO_2 emissions. Theoretically, the thermodynamic efficiency of CEECs such as the polymer electrolyte fuel cell (PEMFC) are superior to conventional internal combustion engines [1]. State-of-the-art PEMFCs implement into prototype fuel cell cars, have demonstrated efficiencies in the range of 45 to 55 %, whereas the internal combustion engines operate with a maximum of ~35 % efficiency [2-3]. Despite this advantage, however, PEMFC powered cars are still not commercially available, which can be attributed to a number of apparent obstacles.

The largest of these obstacles is the high cost of the PEMFC, which is more than one magnitude higher per Watt of power in comparison to the combustion engine [4]. A significant proportion of PEMFCs costs arise from the large precious metal content contained in the membrane electrode assembly (MEA) [5]. Strategies to reduce the precious metal content of MEAs include alloying Pt with less expensive metals such as cobalt and forming core-shell particles. By using core-shell particles, not only is the Pt content reduced, but also the kinetics of the oxygen reduction reaction (ORR) are enhanced [6]. It has, however, been shown that these alloys are not stable in the acidic fuel cell environment [7].

A possible alternative to PEMFCs for low power applications are anion exchange membrane fuel cells (AEMFCs). These alkaline fuel cells possess the advantage that non-platinum catalysts, such as silver and even carbon electrodes, are active for the

oxygen reduction reaction [8-10]. Although platinum is still undisputedly the most active material in alkaline electrolyte, the relatively cheap price of non-platinum catalysts in terms of activity per € makes them interesting indeed. In contrast to PEMFCs, the major challenge for the AEMFCs is the poor ion conductivity of anion exchange membranes rather than the cost of the electrocatalyst material. Recent improvements in anion exchange membranes have, however, significantly reduced the difference to proton exchange membranes [11].

There are two approaches toward advancing our understanding of fuel cell reaction processes in order to develop more economical catalysts. The first involves investigating the parameters that influence the activity of catalysts based on model systems such as single crystals and bulk polycrystalline electrodes. The second approach is to investigate the properties of high surface area carbon (HSAC) supported nanoparticle catalysts, i.e. applied catalysts that are developed for fuel cell devices.

Both of these strategies were pursued in this thesis. Although electrocatalytic measurements appear relatively straightforward to perform, both strategies demand highly precise measurements with careful control over a variety of experimental parameters, and a thorough understanding of the measurement system. For instance, the inherent solution resistance between working electrode and luggin capillary introduces a shift in the measured potential relative to the interfacial potential. The magnitude of this potential shift is dependent upon the flowing current, and hence is commonly termed the iR drop. Whilst this solution resistance cannot be completely avoided, it can be measured and compensated for to ensure that it does not introduce an unquantifiable error into the electrochemical measurement. This is particularly important in electrocatalysis, where the exponential potential dependence of the kinetic current can be significantly influenced by uncompensated solution resistance [12]. Concerning HSAC supported electrocatalysts more specifically, an additional factor comes into play. These catalysts are typically inhomogeneous, and it is therefore important to investigate a considerable number of samples in order to accurately characterise and compare their properties. An important property for instance, is the electrochemically accessible surface area. Using a standard electrochemical working station an experienced experimenter, along with a

considerable amount of time, is required for the experimental measurements and their analysis. Consequently, an automated measurement system, with a higher throughput, such as the one developed in this thesis, is extremely beneficial.

The aim of this thesis can be divided into three main objectives, which were:

i.   to design, build and optimise a state-of-the-art electrochemical measurement and analysis setup, which is largely automated and thus easy to operate, even by inexperienced students. In addition, the setup should be flexible, extendable to other electrochemical techniques, compatible with different potentiostats, and suited for investigations in different acids, as well as alkaline solutions.

ii. to study the influence of surface oxide formation on the catalytic properties of polycrystalline Pt towards the hydrogen oxidation reaction (HOR), oxygen reduction reaction (ORR) and finally, the oxidation and reduction reactions of peroxide. This is of fundamental interest because polycrystalline Pt serves as a benchmark due to its high activity towards these reactions.

iii. to characterise a nanoparticle Ag catalyst for the ORR in alkaline solution. The standard methodologies applied for characterising platinum based catalysts, are not applicable to non-platinum particles, hence a new methodology was developed.

The structure of this thesis is as follows. In the first section, theoretical aspects of the electrochemical setup will be discussed (Chapter 2).This is followed by a description of the development of an state-of-the-art electrochemical setup with respect to hardware (Chapter 3) and software (Chapter 4). In the remaining sections, the characterisation of Platinum (Chapter 5) and nanoparticle silver (Chapter 6) electrocatalysts will be presented and discussed.

2 Theoretical aspects of the electrochemical setup

In the following chapter the theoretical details of electrocatalytic measurements are shortly described. The first part of the chapter deals with the theoretical background of electrode reactions and potential perturbation techniques applied for their investigation. In the following parts the measure system and theoretical aspects of the developed hardware are described along with considerations of how to classify the term catalytic activity of an electrocatalyst.

2.1 Electrode Reactions

2.1.1.1 Faradaic Process

A faradaic process is a chemical process involving the transfer of one or more electrons from an electrochemical active species to an electrode or vice-versa. An electrode is a conductive solid introduced into an electrolyte, a substance containing free ions.

$$A^{-n} \underset{reduction}{\overset{oxidation}{\rightleftharpoons}} A + n \cdot e^{-} \tag{1}$$

As outlined in equation (1) the electron transfer away from the electroactive species is defined as an oxidation process and the species is oxidized, whereas the opposite process is called reduction. Out of convention an oxidation current is defined as positive and a reduction current as negative.

The energy of the electrons (Φ) in the electrode is the decisive factor in which direction the electrons are transferred. If the energy level is higher than that of the lowest unoccupied molecular orbital (LUMO) of the electroactive species, an electron can be transferred and the species is reduced, whereas if the energy level is lower than the highest occupied molecular orbital (HOMO) of the species an electron transfer can occur in the opposite direction and the species is oxidized.
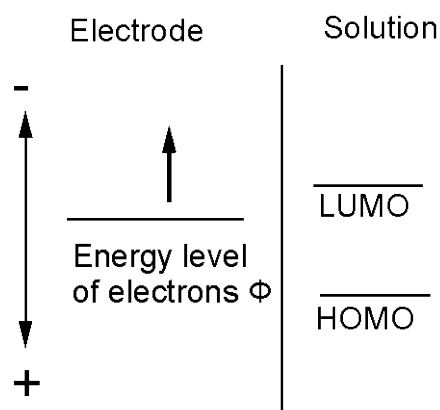
Figure 2.1-1: **Energy diagram. The electrons will transfer over the interface in order to minimise its potential energy.**

If an electrode is inserted into an electrolyte a faradaic reaction might occur, either oxidation or reduction. For every reaction, the interface becomes more and more polarised until an energetic equilibrium is reached. The polarisation of a single interface cannot be determined experimentally, thus, a second electrode is needed.

The potential difference between two electrodes U is then defined as:

$$U = \phi_{E1} - \phi_{E2} \tag{2}$$

The voltage between the two electrodes correlates to the change of free energy ΔG of the system by the thermodynamic relation:

$$\triangle G = -nFU \tag{3}$$

, where n is the number of electrons and F the Faraday constant. Reactions can be forced to proceed in a certain direction by applying a voltage difference between the two electrodes that exceeds the thermodynamically induced potential difference.

Although a reaction might be thermodynamically favourable, the reaction does not have to occur as a result of an activation barrier of the process. The study of this phenomenon – the field of kinetics – is at the heart of electrocatalysis. It is compromised by the fact that two reactions must occur in order to sustain neutrality of the solution. As a result, the current-potential relation of an electrode of interest, i.e. the working electrode (WE), depends on two reactions. A potentiostatic probe, a reference electrode (RE), has therefore to be introduced into the measurement

system, such that current-voltage relationships occurring at working electrode can be studied with respect to the RE, disregarding the second electrode, called the counter electrode (CE). Thus the polarizing current flows through one circuit (which includes the WE and the CE) while the resulting change in potential of the WE is measured with respect to the RE in a different circuit, through which the current is essentially zero. The electrochemical potential can therefore be defined as:

$$E = \phi_{WE} - \phi_{RE} \tag{4}$$

Arrhenius showed that the rate constant k of many chemical reactions can be expressed in the form:

$$k = A'e^{-\frac{E_A}{RT}} \tag{5}$$

where E_A is the activation energy, R the gas constant, T the temperature and A' the so called frequency factor. Deploying the rate constant to an electrochemical system with a red-ox couple one yields the general Buttler-Volmer equation[13]:

$$i_k = FAk_0 \left[C_O\, e^{-\alpha\frac{nF}{RT}(E-E^0)} - C_R\, e^{(1-\alpha)\frac{nF}{RT}(E-E^0)} \right] \tag{6}$$

The Butler-Volmer equation relates the kinetic current i_k of an electrochemical reaction to the interfacial potential E referenced to a standard potential E_0, the concentrations of oxidized C_O and reduced C_R species, the surface area A of the electrode, the standard rate constant k_0 and the symmetry factor α of the energy barrier.
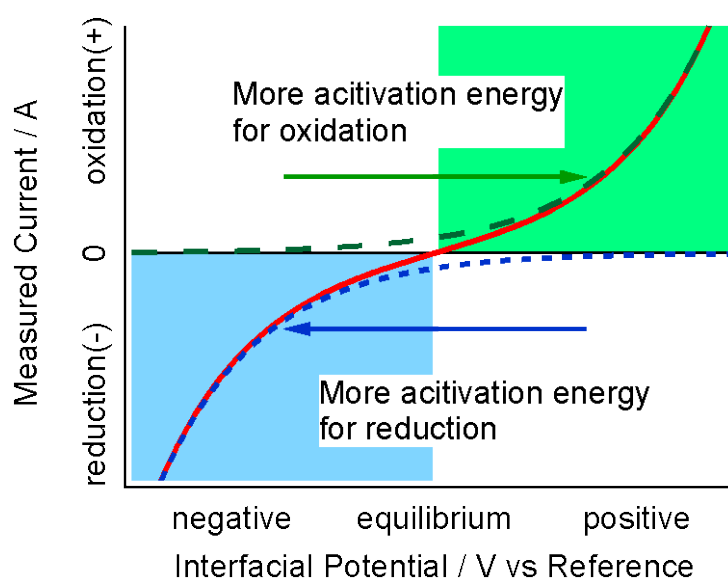
Figure 2.1-2   Visualisation of the Buttler- Volmer equation

A net reaction rate in one direction shifts the concentration of oxidized and reduced species until a potential dependent equilibrium is reached. The standard potential of a process defines this equilibrium under standard conditions.

The equilibrium potential of the process at an arbitrary concentration of the electroactive species is given by rewriting the Buttler-Volmer equation with respect to E, resulting in the Nernst equation:

$$E = E_0 + \frac{RT}{nF} \ln \frac{[C_0]}{[C_R]} \tag{7}$$

, which indicates that the equilibrium potential of a process shifts proportionally to the logarithm of the concentration ratio of the redox couple.

The potential E is always measured relative to a reference electrode and not on an absolute scale. In order to compare different reaction potentials a reaction that defines 0 is required. For that purpose, the standard hydrogen electrode (SHE) defines as 0 V the potential of the hydrogen oxidation- and evolution reaction in 1 N acid electrolyte, or more accurately at a proton activity of 1.

$$2H^+ + 2e^- \rightleftharpoons H_2 \tag{8}$$

For the study of pH-dependent reactions, such as those occurring in fuel cells, it is however more convenient to use a pH dependent reference potential, the reversible hydrogen electrode potential (RHE):

$$E_{RHE} = 0V_{SHE} - 60mV * pH \tag{9}$$

2.1.2 Surface Reaction

A faradaic process can be divided into two classes; continuous and adsorption processes. They differ by the fact that in the second case, the electrochemically active species becomes adsorbed on the surface of the working electrode and blocks it for further reactions (5).

$$A^- + M \rightleftharpoons AM + e^- \tag{10}$$

These processes are distinguishable only by the different current response upon a potential perturbation. This can be exemplified assuming the adsorption process follows a Langmuir isotherm:

$$\frac{\theta}{1-\theta} = Ke^{\frac{F}{RT}(E-E_0)} \tag{11}$$

7

, where K is the adsorption constant and θ the ratio between the number of free and the total number of surface sites. At equilibrium conditions, no net current will flow. However, by perturbation of the system a net current flows in order to establish the new equilibrium. Rearranging the equation and differentiating θ with respect to the time, the following expression describes the current:

$$i_k = Q\frac{d\theta}{dt} = Q\frac{F}{RT}\frac{e^{-\frac{F}{RT}(E-E_0)}}{\left(1+Ke^{-\frac{F}{RT}(E-E_0)}\right)^2}\frac{dE}{dt} \tag{12}$$

where Q is the total charge of a saturated adsorbate monolayer. It is seen that the current response of a surface process does not only depend on the potential, but is also sensitive to the rate of changing the potential, which is in contrast to a continuous reaction.

The difference between a surface and a continuous reaction can be seen in figure 2.1-3, where equation (12) is visualised. Sweeping the potential from a negative potential in positive direction a bell-shaped current response is obtained. The initial exponential increase is inhibited by a decrease in available surface sites. As the surface free sites continue to diminish, a maximum current is reached at a coverage of 50%, followed by an current decline to zero. Sweeping the potential in the opposite direction induces an identical reduction wave. The features discriminates the surface reaction from a continuous reaction, for which the current would exponentially increase as the as potential increases (see figure 2.1-2) until it is limited by the transport of the electroactive species to the electrode surface.
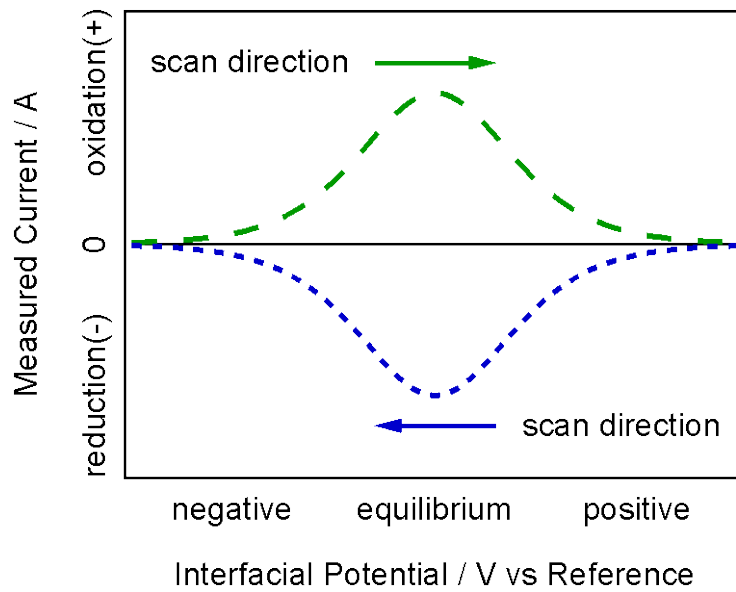
Figure 2.1-3: **Visualisation of a surface reaction during a potential sweep in positive and negative direction**

2.1.3 Perturbation techniques

Several potential perturbation techniques can be used in order to measure faradaic processes. The most commonly used are shown in figure 2.1-4; i.e. triangular waves, steps, sinusoidal, and square wave (SW). In electrochemistry, the techniques are better known as Cyclic voltammetry (CV) for a triangular wave, Chronoamperometry applying potential steps and electrochemical impedance spectroscopy (EIS) for sinusoidal potential perturbations.
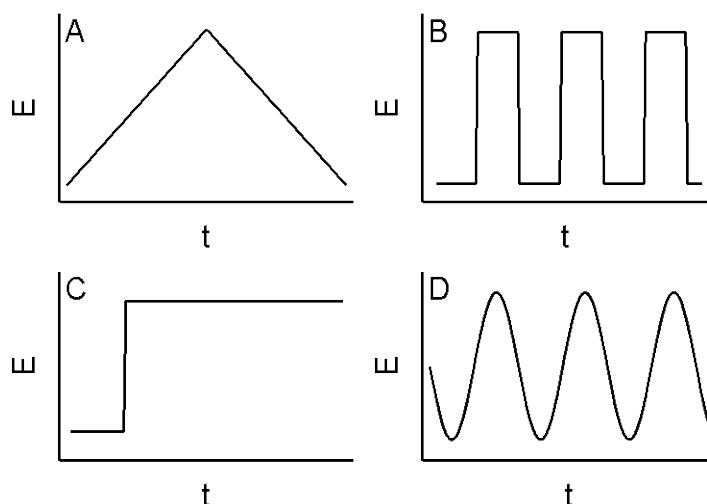
Figure 2.1-4: **Schematic presentation of common potential perturbation techniques.**

Given that the faradaic current is a function of both the potential and its derivative with respect to time, upon applying these techniques from the current response a reaction model can be deduced.

Furthermore, a combination of the techniques is possible, such as Square wave voltammetry (SWV), triangular waves imposed by square waves, AC voltammetry (ACV), or triangular waves imposed by sinusoidal potential perturbations. The technique of choice depends strongly upon the experimental conditions and the reaction variables of interest. In general however, a preliminary CV can give a good "finger print" of the occurring faradaic process.

2.1.4 Mass Transport

2.1.4.1 Introduction

Studying the potential dependent rate of an electrochemical process, i.e. the activity of an electrode material, mass transport limitations of the reactive species have to be taken into account. At potentials where the rate of the reaction is fast, the reactants immediately are transformed as they enter the vicinity of the electrode. The apparent activity, i.e. the activity which is experimentally determined, is only governed by the mass transport rate of the reactants to the surface, not the electrode kinetics. The measured current in such situation defines the diffusion limited current (i_{dl}).
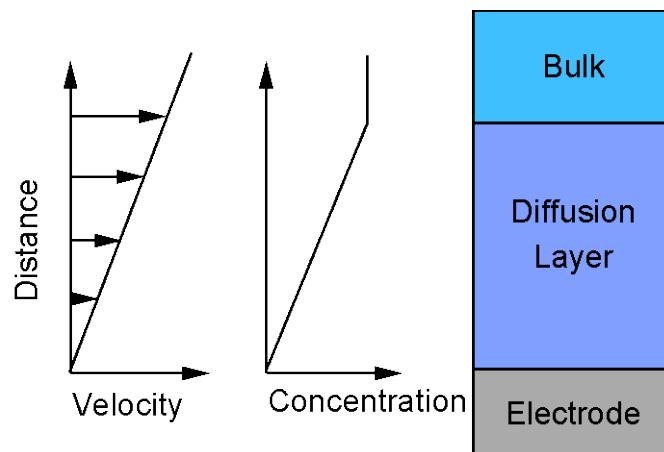
Figure 2.1-5: Scheme of the electrode/electrolyte interface. At the left hand side the concentration profile of the reactants during fast kinetics is plotted as a function of the distance to the electrode surface. For fast kinetics the reactant concentration close to the electrode surface is zero. The observed current is limited by the diffusion of reactants through the electrolyte layer at the interface, i.e. the diffusion layer.

The label "diffusion limited" originates from the pure diffusive mass transport occurring in the in vicinity of the electrode. Close to the working electrode, a volume with a concentration profile of the reactants ranging from bulk to zero concentration at the electrode surface is formed (see figure 2.1-5). Although the solution is stirred, in this diffusion layer there is virtually no convection perpendicular to surface occurs. Thus the reactants diffuse to the surface due to the concentration gradient. The thickness of the layer is governed by the bulk solution velocity. Increasing the convection results in a higher diffusion limited current because of the decrease in the diffusion layer thickness. The flux of the reactants to the surface is proportional to the thickness of the layer, their concentration in the bulk of the electrolyte and the diffusion coefficient.

2.1.4.2 Factors influencing the measured current

The measured current, i_m, is at all times dominated by either kinetic limitation or diffusion limitation. The exact relation between these two quantities depends on the geometry of the electrode and the flow profile. For smooth, planar, and uniformly

accessible electrodes, such as the rotating disk electrode (RDE), the measured current can be described by the Koutecký-Levich equation:

$$\frac{1}{i_m} = \frac{1}{i_k} + \frac{1}{i_{dl}}$$

(13)

As approximation, this equation can also be used to describe the current for some non-uniformly accessible electrodes, such channel flow electrodes, given that $i_k < i_{dl}$, i.e. if the measured current is less than 50% of the diffusion limited current [14].

The smaller of the two, i_{dl} or i_k will control the measured current. In figure 2.1-6, the equation has been visualised together with the kinetically controlled and the diffusion limited current. Three potential regions can be defined depending on which factor controls the current: the kinetically controlled, the mixed and the diffusion limited potential region.
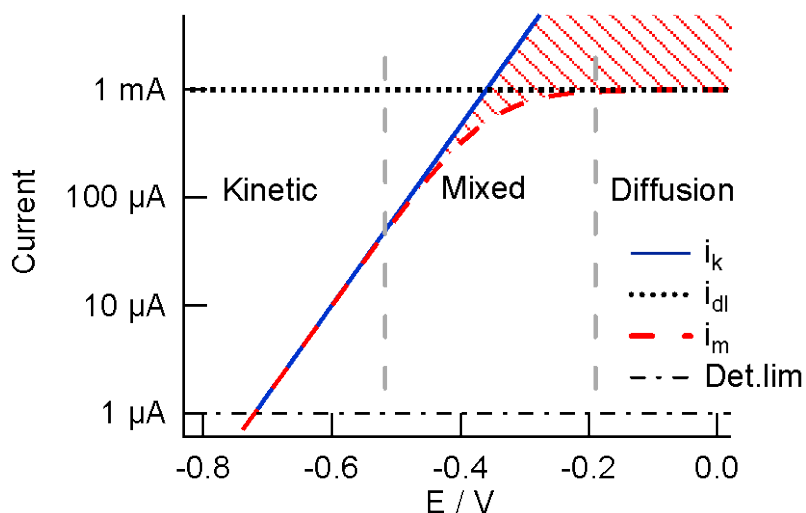
Figure 2.1-6: **Schematic presentation of the Koutecký-Levich equation. The blue line indicates the potential dependence of the intrinsic kinetic current, whereas the dashed red line shows the measured current for a chosen diffusion limited current (dotted line). The detection limit (dashed-dotted line) is determined by the potentiostat.**

It can be seen that the kinetically controlled current can only be measured directly at a current magnitude of at least one order smaller than the diffusion limited current. This is of course a great practical limitation as the potential range where the reaction

kinetics can be studied is quite small as a result of the detection limit of the potentiostat.

2.1.4.3 Extracting the kinetic current in the mixed region

By rearranging the terms in the Koutecký-Levich equation, the kinetic current can also be obtained in the mixed potential region where the measured current is partially limited by diffusion.

$$i_k = \frac{i_m i_{dl}}{i_{dl} - i_m} \tag{14}$$

In other words, the measured current is corrected by the known diffusion limited current in order to obtain the kinetic current. In order to keep the error low, however, it is essential to elucidate the current region where this correction is valid. Differentiation of i_k with respect to i_{dl} and i_m gives the following expression for the relative error:

$$\frac{\Delta i_k}{i_k} = \frac{i_m}{i_{dl} - i_m} \frac{\Delta i_{dl}}{i_{dl}} + \frac{i_{dl}}{i_{dl} - i_m} \frac{\Delta i_m}{i_m} \rightarrow \begin{cases} \dfrac{\Delta i_{dl} + \Delta i_m}{i_{dl} - i_m} & i_m \rightarrow i_{dl} \\ \dfrac{\Delta i_m}{i_m} & i_m \ll i_{dl} \end{cases} \tag{15}$$

The absolute error of the potentiostat is in general low, i.e. 0.1% of the chosen current range. The relative error due to the diffusion limited current can however be considerate, especially when the source of convection is not stable. From the error estimation, we can see that if the measured current is small, the error on determined kinetic current is dominated by the error of the potentiostat (neglecting any capacitive currents). At the other limit, where the measured current approaches the diffusion limit, the relative error of the determined kinetic current is dominated by the pre-factor, which approaches infinity. As a rule of thumb, no kinetic data can therefore be extracted from a measured current that is larger than half of the diffusion limited current.

In order to obtain a kinetic current over a broad potential and current range, the experimental setup should be optimized for a diffusion limited current that is as large and stable as possible.

2.2 Measure system

2.2.1 Potentiostat

The electrochemical experiments are conducted using a Potentiostat; an electronic device with a controllable current source, an electrometer and an ammeter.
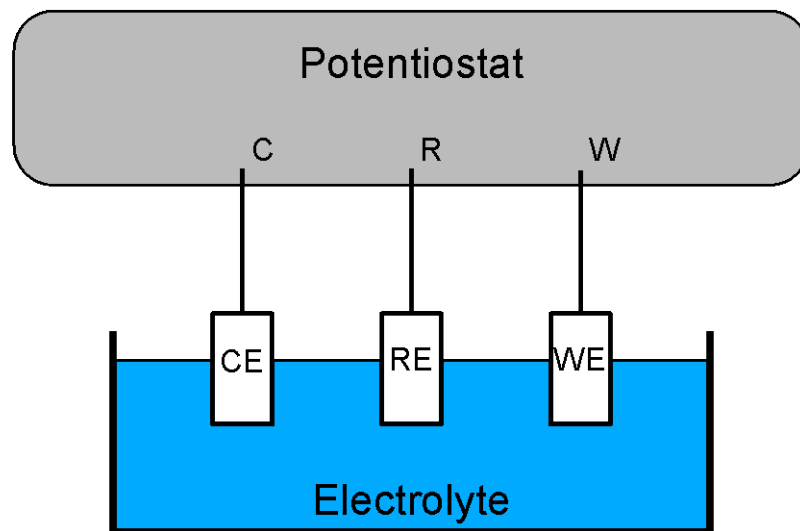
Figure 2.2-1:   **Scheme of an electrochemical 3-electrode setup**

The Potentiostat operates by passing a current through the counter (CE) to the working electrode (WE), where the current is measured. The potential difference, required to force the current between the electrodes, depends on the potential drop over the two interfaces as well as the solution resistance between the electrodes, see figure 2.2-2.
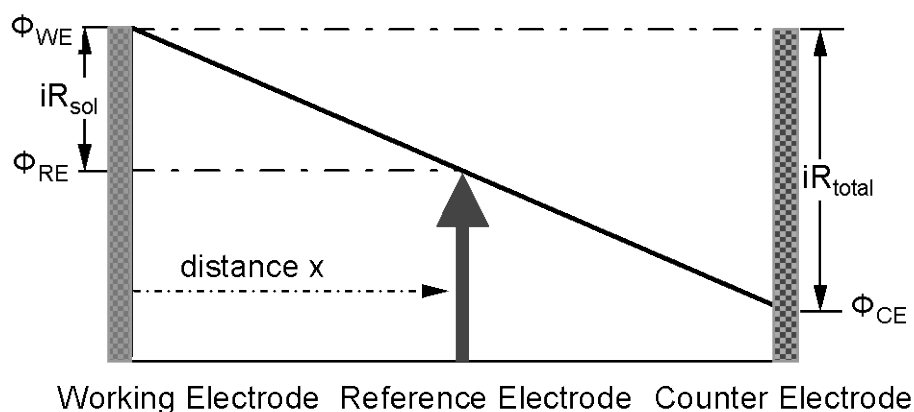
Figure 2.2-2: Scheme of voltage drop between the electrodes in a three electrode setup

In order to exclusively study the reaction at the WE, a potential probe is introduced between CE and WE. The probe, the reference electrode, is usually placed in a small receptacle containing a high concentration of ions in order to have a stable red-ox couple of the electrode and thus to fix the interface polarisation. The receptacle has a small porous glass frit to allow the ion exchange with the main electrolyte. This ensures an electrical contact, but minimises the anion diffusion/convection from the receptacle to the main electrochemical cell. The current-potential relation of the WE with the respect to the RE can thus be measured disregarding the interfacial potential difference of the CE. Thus the WE is considered to be examined in a so called "half-cell"(see chapter Half-Cell Model).

For the elucidation of the interfacial potential difference of the WE and its influence on the electrochemical reactivity, one of the quantities, current or voltage can be controlled by the potentiostat, i.e. the potentiostat operates in galvanostatic or in potentiostatic mode.

2.2.2 Half-Cell Model

Using a three electrode setup, the so called half cell model, shown in figure 2.2-3, can be used to describe the measure system.
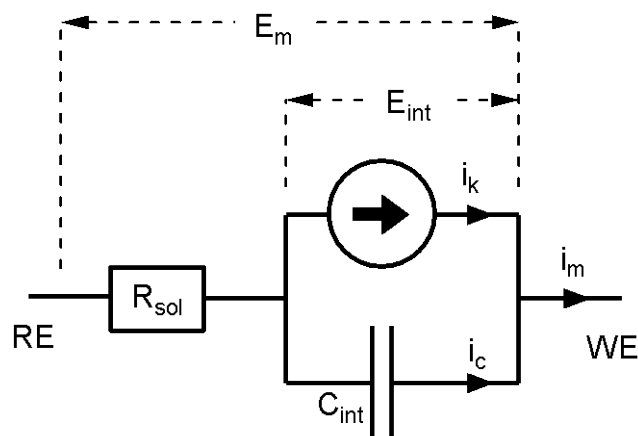
Figure 2.2-3:   The half cell model – an electrical circuit representation of the measured system

E_m corresponds to the measured voltage difference between WE and RE, and i_m to the measured current, i.e. the current floating through the working electrode. The resistor (R_{sol}) corresponds to the part of the total solution resistance due to the spatial distance between RE and WE (see also figure 2.2-2). As a consequence, the interfacial potential difference (E_{int}) can only be measured directly in absence of any current, else it is given by:

$$E_{int} = E_m - R_{sol} i_m \qquad (16)$$

The current source symbolizes the faradaic processes occurring on the WE and its vicinity. The current (i_f) provided by the source is a function of the interfacial potential (E_{int}) and the rate of change of the potential (dE_{int}/dt).

The interface capacitance (C_{int}) is in parallel with the current source. It describes the ion movement as a result of a change of the interfacial polarisation. Although symbolised by a standard capacitor, it can still be a function of potential [13]. This effect, however, in most cases is small and can be ignored.

The measured current i_m is the sum of the current floating through the capacitance (i_c) and i_f. This complicates the determination of i_f and hence a so called "background measurement" can be necessary to determine i_c.

2.2.3 Measure System Errors

The accuracy, in terms of the capability of the electronic system to measure both voltage and current is in general quite high in any modern measure system. Hence, often the major source of error in a measure system comes from the physical

16

limitations of the cell setup. Therefore, it is important to optimise the cell setup in such a way that electronic interference and sources of statistical noise become negligible.

In addition systematic errors occur as the interfacial potential cannot be directly measured. In order to elucidate systematic errors an analysis of the coupled system with the respect to the potential and current can be performed.

2.2.3.1 Potential Error

The interfacial potential has been defined in equation (16), as the difference between the applied potential and the potential over the solution resistance. The systematic error of the potential can therefore be defined as the difference between measured and interfacial potential, thus we get

$$\Delta E_{int} = -R_{sol} i_m \tag{17}$$

The error is a linear function of the measured current, thus its value can be both positive and negative depending on the experimental conditions. The impact of this error on a continuous faradaic process is exemplified in figure 2.2-4.
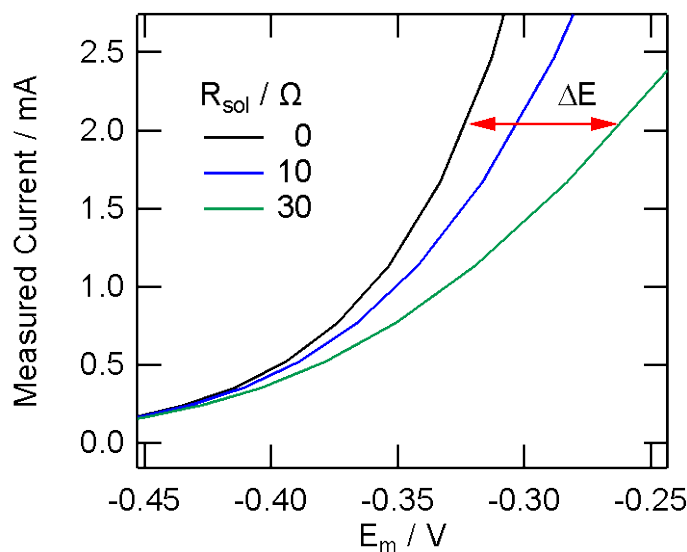
Figure 2.2-4: **Simulation of the systematic potential error resulting from an uncompensated solution resistance. A faradaic current is plotted as a function of potential without (black line), with 10 Ω (blue line) and 30 Ω (green line) solution resistance.**

Figure 2.2-4 illustrates the influence of the solution resistance on the i-v-characteristics for 3 different values of solution resistance (0, 10 and 30 Ω). It can be seen that at low currents, the curves coincide, whereas at higher current magnitudes the curves deviate from each other due to the potential error. Explicitly, at a current of 1mA the resulting potential deviation is 10mV and 30mV, respectively.

The linear error term clearly causes the two latter curves to significantly deviate from the expected exponential form of the "real" current curve, especially at large currents. The underestimation of the solution resistance can thus lead to the conclusion that the exponential slope of the kinetic current changes with potential, although it is not.

2.2.3.2 Scan Rate Error

A conventional potential perturbation technique is to sweep the potential at a certain rate (v) and record the resulting current, i.e. a so called cyclic voltammogram. The solution resistance introduces also a systematic error in cyclic voltammetry. As the potential cannot be measured directly at the interface, the apparent scan rate can deviate from that seen by the interface. Defining the interfacial sweep rate:

$$v_{int} = \frac{dE_{int}}{dt} \tag{18}$$

, and substituting E_{int} by using equation (16), the following expression is received:

$$v_{int} = v_{app} - R_{sol} \frac{di_m}{dt} \tag{19}$$

where v_{app} is the apparent scan rate applied by the Potentiostat. Again, the error can be defined as the difference between the interfacial and apparent scan rate:

$$\Delta v_{int} = -R_{sol} \frac{di_m}{dt} \tag{20}$$

From this equation we can see that a solution resistance and fast current change can indeed cause an error in the real interfacial sweep rate. Compared to the constant sweep rate of the potentiostat, the interfacial rate will either be "inhibited" or "accelerated", depending on the sign of the time derivative of the current. For example, assuming a current change of 2mA/s as the potential is swept with 100mV/s, for a solution resistance of 10 Ω a relative sweep rate deviation of about 20% is expected.

This effect can be visualised by a simulation, based on the current voltage relation in figure 2.2-4. In the simulation, the apparent voltage sweep is applied in positive

direction with a rate of 100mV/s and the current exponentially increases. The results assuming different solution resistances are depicted in figure 2.2-5, where the real interfacial scan rate has been plotted as a function of the apparent potential.
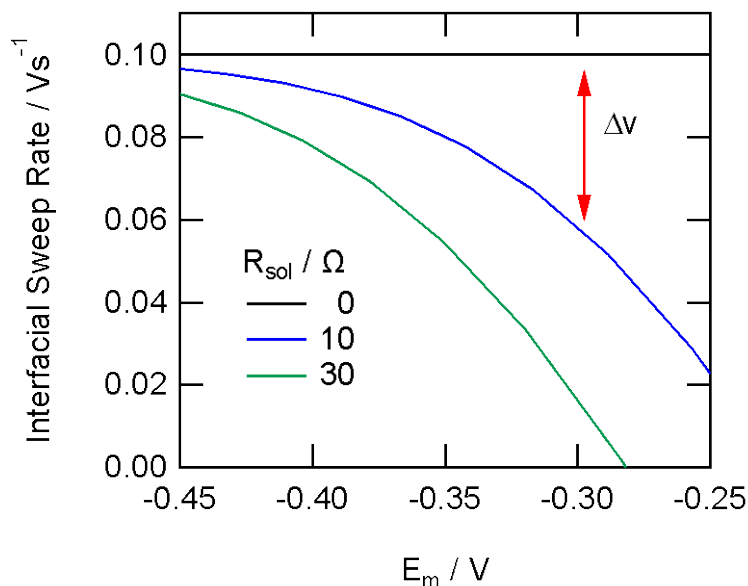
Figure 2.2-5: **Visualisation of the systematic scan rate error as a result of an uncompensated solution resistance using i-E-data from figure 2.2-4. The effective (real) scan rate is plotted as a function of potential without (black line), with 10 (blue line) and 30 Ω (green line) solution resistance.**

Obviously, as the potential and current increases, the interfacial scan rate decreases drastically – the larger solution resistance, the larger the deviation. Notice that at a certain point in the simulation the interfacial sweep rate curve crosses the 0 line, which is an artefact and an indication of the limitation of the linear approximation. In a real system such an effect cannot occur. Instead the interfacial scan rate would approach 0.

The described effect creates a fundamental problem in the correlation between the result of a measurement and a reaction model. The assumption that the sweep rate is constant over time does not hold anymore. Thus fitting a mathematical expression derived from a reaction model which uses this assumption can lead to erroneous results.

2.2.3.3 Apparent Current Error

The measured current has in general no systematic errors given a correct experimental setup. As a consequence the measured current is a fingerprint of the real conditions at the interface.

Because of the previously described potential and scan rate errors, however, the actual conditions at the solid-liquid interface are unknown. The systematic error induced by the potential and scan rate error can be interpreted as a systematic current error using an error propagation. The measured current is a superposition of faradaic and capacitive currents, which are both functions of scan rate and potential difference.

$$i_m = i_f(v_{int}, E_{int}) + i_c(v_{int}, E_{int}) \tag{21}$$

A differentiation with respect to potential and scan rate results in the following expression:

$$\Delta i_m = \sqrt{\left(\frac{\delta i_m}{\delta v_{int}} \Delta v_{int}\right)^2 + \left(\frac{\delta i_m}{\delta E_{int}} \Delta E_{int}\right)^2} \tag{22}$$

From this equation we can see that the error of both potential and scan rate causes a deviation from the measured and the expected faradaic current. This is exemplified in figure 2.2-6, where the expected current-potential relation of a faradaic process is given assuming different solution resistances.
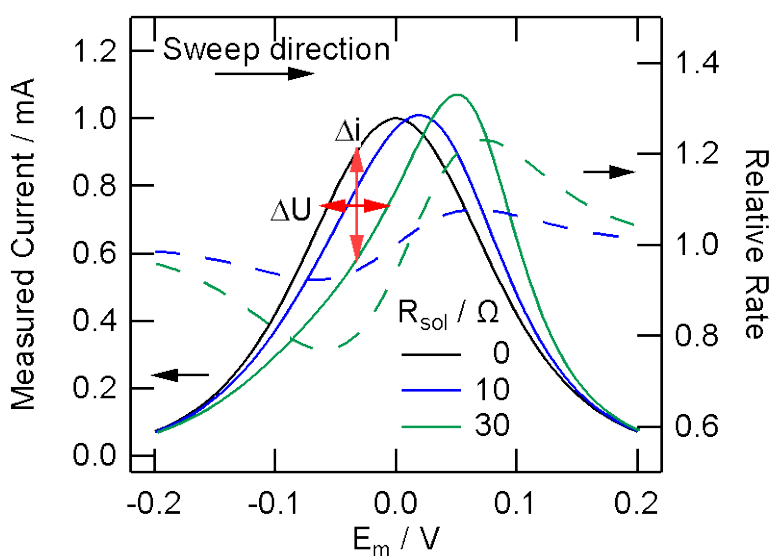
Figure 2.2-6: **Simulation of current response from a surface reaction in the presence of an uncompensated solution resistance. The**

faradaic current is plotted as a function of potential without (black line), with 10Ω (blue line) and 30 Ω (green line) solution resistance. In addition, the relative scan rate for the respective R_{sol} is plotted as dashed line. It is seen that as a result of the non-constant scan rate and the scan rate dependency of the surface reaction, in addition to the potential error a current error is induced by the solution resistance as well.

In figure 2.2-6, the i-v-characteristic of a faradaic surface reaction which follows a Langmuir isotherm is plotted for a constant potential sweep. Although always the same reaction is assumed, the apparent characteristics change with increasing solution resistance. As the current is proportional to v_{int}, the measured current in the presence of a solution resistance can be even larger than the current measured in the absence of a resistance.

The measured current-voltage characteristics of a system perturbed by a solution resistance mimics the behaviour of a more complex adsorption isotherm model [15]. Hence, although small, the solution resistance can indeed cause erroneous conclusions.

2.2.4 Minimization of the systematic error

From the error estimation in the previous sections we have seen that a relative small solution resistance can result in large systematic errors. It is therefore essential to determine the solution resistance of the experimental setup and at the same time to find strategies how to minimise it. In doing so, the cell design, electronic compensation and/or post measurement corrections can be considered.

2.2.4.1 Measure the Solution Resistance

Given the model of the half-cell (see figure 2.2-3), the current response due to a voltage perturbation differs depending on the characteristic time scale of the perturbation. This is mainly due to the intrinsic interfacial capacitance of the working electrode. At a long time scale, the capacitance has a large impedance and the current floating through this element is negligible. As a result, the measured current is determined by the faradaic current and the solution resistance. On the contrary, at short time scale the capacitance has a very small impedance and the current

21

measured as a result of the perturbing voltage is only determined by the solution resistance.
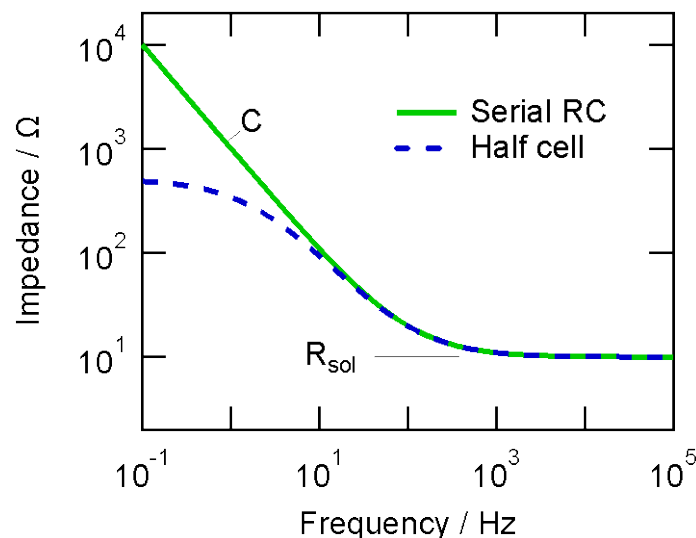
Figure 2.2-7: **Simulation of the impedance spectrum of a half cell model in comparison to a serial RC circuit**

This behaviour is illustrated in figure 2.2-7, where an impedance spectrum is shown. The frequency equals the reciprocal time, thus a low frequency corresponds to a long time period. The spectrum resulting from applying a small sinusoidal perturbation signal ($<10mV_{peak-to-peak}$) to the system is shown for various frequencies ranging from 0.1 Hz to 100 kHz. The small perturbation implies that linear approximations are valid for each component. As a result, the faradaic current source can be approximated as a resistance. In the absence of any faradaic processes, the half cell would resemble a serial RC circuit. The impedance spectrum shows that the impedance decreases as the frequency increases reaching a plateau of global minimum at a value corresponding to the solution resistance.

Once the system is known, in order to determine the solution resistance it is sufficient to apply only one frequency where the plateau is formed. Thus the resistance can even be monitored online while performing other slow EC techniques.

2.2.4.2 Physical minimization of the solution resistance

The electrolyte is an electrical conductor with free moving ionic charges, similar to the electrons in a metal. The resistance of such a conductor depends on the resistivity

(ρ) as well as the geometry and can be described by the following equation in the cylinder approximation:

$$R_{sol} = \rho \frac{l}{A} \qquad (23)$$

where, d the length and A the cross section of the conductor. The resistivity is proportional to the inverted ion concentration and diffusion coefficient.

In order to reduce the resistance, an electrolyte with high ion concentration and, if possible, at elevated temperatures should therefore be used. In cases where this strategy is not adequate, the cell design can be improved. Decreasing the physical distance between WE and RE results in a lower solution resistance. However, in practise this is limited due to the form and size of the electrodes.

Luggin Capillary

Instead, the reference electrode can be placed in a separate compartment which is connected to the main chamber via a thin capillary, a so called Luggin capillary [16-17].

A potential difference over a resistor exists only if a current flows. As virtually no current flows through the reference electrode and thus inside the capillary, no voltage difference exists between the tip of the capillary and the RE. This implies that the effective solution resistance is only proportional the distance between the tip of the capillary and the WE, and not to the distance of reference electrode. In addition, the small capillary does not suffer from size constraints and can be place much closer to the WE.

2.2.4.3 Electronic Compensation

The potential offset resulting from the solution resistance can further be reduced by applying an electronic compensation. With compensation, the potential between working and reference electrode will no longer be the same at the output of the potentiostat. Instead, a compensated potential E_{comp} is given and defined by

$$E_{comp} = E_m - R_{comp}i_m \qquad (24)$$

, where R_{comp} is the compensation factor. As a result, the compensated voltage will be smaller than the applied value for a positive current. Substituting E_m in equation (16) gives:

$$E_{int} = E_{comp} + (-R_{sol} + R_{comp})i_m \qquad (25)$$

23

If R_{sol} is known, R_{comp} can be set if not fully to cancel out the solution resistance, but at least to reduce the error. A full compensation is in general difficult due to the induced instability of the control system of the potentiostat and the increasing noise level.

With the help of the compensated voltage rather than the one measured in the control loop of the potentiostat, the interfacial voltage can be probed with minimal influence of the solution resistance. With a measure system which is entirely analogue, the compensation scheme also works for high frequencies up to the frequency limitation of the potentiostat, which is in contrast to a digital potentiostat. The remaining uncompensated part of the solution resistance can thereby be determined in-situ as an effective resistance (R_{eff}) just as it would be the "normal" resistance.

$$R_{eff} = R_{sol} - R_{comp} \qquad (26)$$

Thus while monitoring the impedance at high frequencies, the compensation can be tuned during the measurement until an optimal value for the compensation is found. This also prove the functionally of the compensation system. The small error due to the remaining R_{eff} can be corrected after measurement if required.

2.2.4.4 Post measurement correction

Alternatively, the potential can be corrected after the measurement, given that R_{sol}, or the remaining uncompensated part of it, R_{eff}, is known. The compensation can be performed by using equation (24).

The accuracy of a post measure correction, however, suffers from the fact that part of the measured current depends on the rate of potential change as capacitive currents are always present. For a large solution resistance thus equation (24) might not hold anymore. For surface reactions also the measured current has to be corrected (see figure 2.2-6) as it is proportional to the rate of potential change, which might not be constant.

In conclusion, in order to avoid a post correction treatment of the data the cell design and active compensation should always be applied if possible.

2.2.5 Rotation disk electrode

As discussed previously, a major experimental goal in kinetic measurements is to provide a steady and high convection rate of the reactants to the electrode in order to

minimise the error induced by the diffusion limit and its determination (see Mass Transport chapter). For that purpose a rotating disk electrode can be used. The RDE consists of a flat electrode inserted in a cup of insulating material which is attached to a rotating shaft.

An advantage of the configuration is that the radial symmetric geometry enables an analytic approximation of the Navier-Stokes equation at the surface. This, together with Fick's law, results in the so called Levich equation

$$i_{dl} = (0.620)nFA_{geo}C_O D^{2/3}\nu^{1/6}\omega^{1/2} \tag{27}$$

where n is the number of transferred electrons per reaction, F faradays constant, A_{geo} the geometric electrode surface area, C_O the concentration of the active species in the electrolyte, D the diffusion coefficient, ω the rotation rate, and ν the kinematic viscosity of the electrolyte. The Levich equation gives an analytic expression between the measured diffusion limited current and the rotation rate, which enables the study of diffusion phenomena with high accuracy.

A_{geo} should not be confused with the active surface area A_{real} of the electrode. Due to the "averaging effect" of the diffusion in general the same diffusion limited current is measured although the real surface area can largely deviate from the geometric one, especially if electrodes modified by nanoparticles catalysts are used. This is the case if A_{real} is about the same size as or larger than A_{geo}. However, for $A_{real} \ll A_{geo}$ a decrease in the diffusion limited current is observed because some active species arriving at the surface do not reacted and but return to the bulk electrolyte. A similar effect occurs if the WE is covered by a membrane which hinders the diffusion.

2.2.5.1 Diffusion phenomenon

Diffusion phenomena such as diffusion through membranes or arrays of pin holes can readily be studied by RDE. In such a case, the diffusion limited current becomes

$$\frac{1}{i_{dl}} = \frac{1}{B_0\omega^{1/2}} + \frac{1}{i_{dl\_e}} \tag{28}$$

where B_0 is the pre-factor of the Levich equation and i_{dl_e} the supplementary diffusion limitation. The plot $1/i_{dl}$ vs. $1/\omega^{0.5}$ known as the Levich-Koutecký plot allows us to calculate i_{dl_e}. The magnitude of i_{dl_e} can be extracted by extrapolating the measured points to the interception of the y-axis. At $1/\omega^{0.5} = 0$ or in other words at infinite rotation rate, the diffusion limitation is purely dominated by the i_{dl_e}.

2.3 Comparing Activities

One of the main experimental tasks of this work is the study of electrode kinetics, which involves the determination of the faradaic current of a reaction as a function of the interfacial potential difference between the catalyst and the electrolyte. Given that the solution resistance error has been compensated for, the kinetic current is acquired by correcting the measured current for the diffusion limiting current using equation (14). As the kinetic current has an exponential potential dependence by nature, the data are best visualised in a log i-E-plot, normally referred to as Tafel plot. The characteristic reaction parameters to be determined are the voltage dependent exponent of the exponential function as well as the current at a certain potential value. These two values are enough to describe the i_k-E relationship.

The exponent factor can be extracted by fitting the Tafel equation (29) to the data,

$$\log i_k = c + \frac{1}{b} E_{int} \tag{29}$$

where b is the so called Tafel slope and c is a fitting-constant. This equation is a simplified form of the Buttler-Volmer relation, see equation (6), hence b corresponds to the exponent in the exponential function and c to the logarithm of the prefactor.

2.3.1 Activity

For a long time only flat, polished electrodes has been used for RDE measurements due to the easy calculation of the surface area. The measured current density has been referred to as the activity:

$$J_k = \frac{i_k}{A_{geo}} \tag{30}$$

However, although the electrode is flat on a macroscopic level, the surface can exhibit an intrinsic roughness on a microscopic level. Disregarding this effect would result in a higher apparent activity with increasing surface roughness. For this reason only on single crystals the correct activity can be directly determined from RDE measurements without measuring the surface area accessible for the reaction.

2.3.2 Specific activity

The electrochemical active area (ECA) has been introduced in order to compare polycrystalline materials of different surface roughness. The ECA can be defined as the ratio between the charge required to remove (oxidize/reduce) a monolayer of an

adsorbed species (Q_{sample}) and the charge measured by the same procedure for an ideally flat poly-crystalline surface of the same material ($Q_{reference}$) and multiplied its area ($A_{reference}$).

$$ECA = \frac{Q_{sample}}{Q_{reference}} A_{reference} \tag{31}$$

For example in the case of polycrystalline platinum, 195 µC is used in our group as the standard charge required to remove a monolayer of adsorbed hydrogen atoms from a surface of 1cm². This value has been experimentally determined using for electrode preparation the so-called flame annealing preparation procedure [18]. It is noteworthy to point out that this value depends on the preparation procedure as during preparation different ratios of crystalline phases on the surface can be induced.

The specific activity, $J_{k:s}$, i.e. activity normalized to the electrochemical active surface area is:

$$J_{k:s} = \frac{i_k}{ECA} \tag{32}$$

This quantity is of fundamental importance and can be used for example in the study of the size effect of nanoparticlulate catalysts of a certain material.

One intrinsic problem arises however in the activity comparison between catalysts of various materials. The experimental procedure of determining the electrochemical active area is material specific. As mentioned, for Pt based catalysts, which are the most studied class of catalysts for hydrogen oxidation and oxygen reduction, the ECA is calculated with respect to the stripping charge of hydrogen atoms from a PC Pt sample of 1cm² [18]. For many non-platinum catalysts hydrogen atoms do not adsorb on the catalyst surface. Thus, for a fair comparison, it can be discussed whether non-platinum catalysts should be normalized to the same charge value as that of Pt samples or to that of a poly crystalline sample of the same material. For single metal substrates, it would not be a problem to determine such a number, however, for alloys it probably would.

2.3.3 Turn over frequency

In order to avoid some of these definition problems, the turn over frequency (TOF) can be introduced in electrocatalysis, analogue to the definition used in

heterogeneous gas phase catalysis, namely: "molecules reacting per active site in unit time" [19]. In electrochemistry, the number of reacting molecules is given by the kinetic current, divided by the number of electrons transferred in the reaction of interest, z_A, The exact number of active sites for a catalyst is often unknown, hence each electrode atom which is electrochemical accessible can be considered as an active site. The number of electrochemical active sites (NECAS) can therefore be determined by an adequate in situ EC technique; thus resulting in a charge Q divided by the number of electrons for that surface reaction, z_B. The mathematical definition of TOF is therefore given by equation (33).

$$TOF = \frac{\text{molecules per unit time}}{\text{NECAS}} = \frac{\frac{1}{z_A} i_k}{\frac{1}{z_B} Q} \tag{33}$$

The TOF can easily be related to the specific activity of platinum by multiplying with defined normalization constant for the ECA and the number of transferred electrons in that reaction.

2.3.4 Mass Activity

With the introduction of high surface area catalysts, the material required for a reaction can be decreased due to the more advantageous surface-to-volume ratio compared to a flat surface. For such catalysts a practical definition of activity is the mass activity:

$$J_{k:m} = \frac{J_k}{m} = \frac{J_k}{\sigma_m \times A_{geo}}, \tag{34}$$

where m is the catalyst mass and σ_m the catalyst loading applied in the measurement. The activity is easily accessible with a minimum of measurements.
However, care has to be taken that all the catalyst applied in the measurements is indeed accessible for the reaction. Furthermore, this definition does not give any information about the material properties as it is highly proportional to the characteristic size of the particles. On the other hand, it is crucial for engineers planning electrocatalytic devices. A significant fraction of the device price is associated to the catalyst; hence a maximised mass activity is commercially important.

3 Technical hardware developments

In the following chapter the technical developments achieved as part of this thesis are described. The first part of the chapter deals with the experimental details of the applied techniques and the description of the available instrumentation. It is described which improvements of the commercial tools have been performed as well as which experimental hardware was entirely developed within this thesis. A basic description of the necessary theoretical background is given in the respective chapters.

The general goal of this part of the thesis was to create a measurement platform for electrocatalytic investigations where all the experimental parameters can be controlled by the computer in order to facilitate the measurements and increase their reproducibility even for less experienced student users.

3.1 Rotating Disk Electrode

In the following first the design of the commercial RDE device used in this thesis is described and then the improvements of the setup, which were performed as part of this work. As discussed in the section "Theoretical aspects of the electrochemical setup" of this thesis all electrochemical reactions are to a certain degree influenced by mass transport limitations of the reactants to the electrode surface. The rotating disk electrode setup is very practical tool to control mass transport in an electrochemical cell thus enabling in a certain potential window the extraction of the kinetic parameters of certain reactions.

3.1.1 Design of the commercial RDE device

The design of a rotating disk electrode device is exemplified by the commercial available RDE setup (EDI101) from Radiometer. Figure 3.1-1 shows the device, which consists of four parts; a rotating shaft, a middle part, an electric motor and the electrode tip.

Figure 3.1-1: **Drawing of a rotating disk electrode including shaft and electrical motor.**

The rotating shaft consists of stainless steel, which is covered by Teflon (polytetrafluorethylen). The inner part is a stable mechanical rotation transfer, but also acts as electrical conductor between the sample and potentiostat contact. The chemical inert and electrically isolating Teflon protects the inner shaft from corrosion and thereby prevents a possible source of impurities in the measurements.

The middle part contains the ball bearings, which restrain the movement along the axis and allow a friction free rotation of the shaft. The conical lower part permits a fixed and easy fitting into the lid of an electrochemical cell. In order to ensure a good electrical contact and to enable the rotation of the shaft, a soft spring pushes a contact against the shaft. The spring is connected to an external banana plug for an easy connection to the potentiostat.

The electric motor induces the mechanical rotation of the shaft. The rotation rate is measured by an optical switch, which permits an accurate rotation control with only ±0.1% deviation. In the case of the EDI101 this design permits rotation rates up to 5000 rpm.

At end of the shaft, the working electrode tip is screw-mounted. The tip consists of a Teflon cap, in which the working electrode is embedded.

This system permits a fast exchange of samples. This is very advantageous in the research on high surface area catalysts, where sample preparation is in general quite time consuming. The exchange of tips permits that the characterisation and preparation (of new) RDE tips can be done in parallel.

3.1.2 Commercial RDE Tip

The commercial electrode tips from Radiometer for the rotator used in this thesis consist of a radial symmetric conductive cone encapsulated in a Teflon shell, see figure 3.1-2(A). The cone acts as the working electrode and is commercially available as glassy carbon, platinum, or gold tip. In principle, however, it can be made of virtual any solid, conducting material. In order to contact the working electrode to the electrical conductive inner part of the shaft when mounted, a spring pushes a steel needle on to the back side of the electrode cone. The experiments showed that the electrical contact of the commercial glassy carbon electrodes was not optimal and with time the commercial RDE tips degenerate, independently of the working electrode material. Typically, the edges of the cone are not sealed by the Teflon anymore. The degeneration can severely influence the experiments, as will be discussed in the section "General tip issues". As an effect, new expensive tips have to be frequently purchased, which is an economical burden.
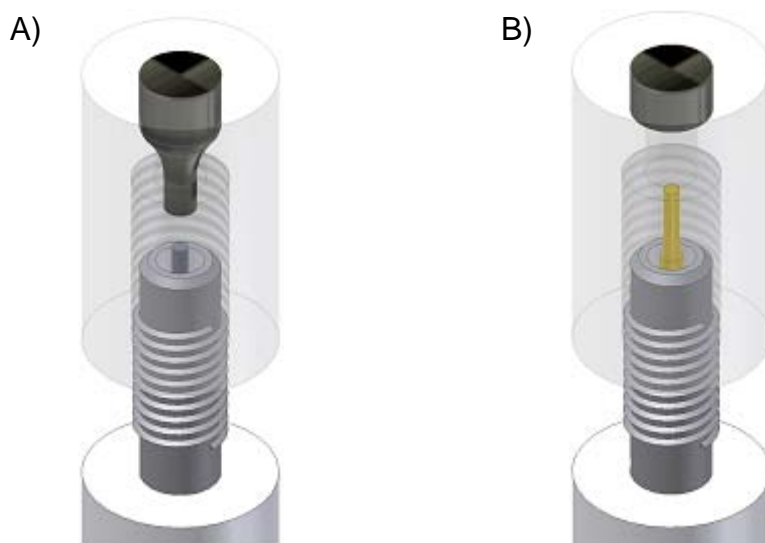
Figure 3.1-2:   **Drawing of the top part of the RDE shaft with half unscrewed tip: A) Commercial B) Homemade.**

3.1.3 Developed in-house RDE tip

In order to improve the performance and reduce costs, we decided to develop and manufacture a homemade version of the RDE tip.

The homemade tips consist of a Teflon cap in which a cylinder of the working electrode material is embedded, as shown in figure 3.1-2(B). Using cylinders of the

working electrode material rather than cones is advantageous as cylinders are easier to manufacture and use less material. This is especially important if the working electrode is made of a precious material, such as high purity platinum, gold or silver.

The working electrode tip is assembled by heating the Teflon cap with a heat gun to temperatures above 250°C. At this point, Teflon becomes semi transparent, soft and expands. The cylinder can then easily be inserted. As the cap cools down, the Teflon contracts and mechanically seals the cylinder. This entails that the cylinder is constraint and cannot fall out of the cap if a force from the electrical contact of the back side is applied. Furthermore, the tight enclosing mechanically hinders the electrolyte to get into contact with the side area of the cylinder; hence, the only part in contact to the electrolyte is the flat, outwards facing disk area.

In order to ensure a low electrical resistance, the contact of the working electrode to the electrical conductive inner part of the rotating shaft was improved. The original steel needle with spring is exchanged by a inexpensive, commercially available and replaceable gold plated steel spring and with a sharp needle tip, which pierces into the backside of the electrode material. Thus the electrical resistance was lowered to less than 1 Ω.

3.1.4 General tip issues improved by in-house design

There are two important issues with the tips that can interfere with the experimental results and have been considerably improved by our in-house design; a large contact resistance and the lateral seal failure.

3.1.4.1 Contact resistance

The electrical contact resistance ($R_{contact}$) between the needle and working electrode cylinder can largely deviate from the ideal value of 0 Ohm. In such a case, as shown in figure 3.1-3, the extra resistance contributes to the measured resistance which can further increase the systematic error.
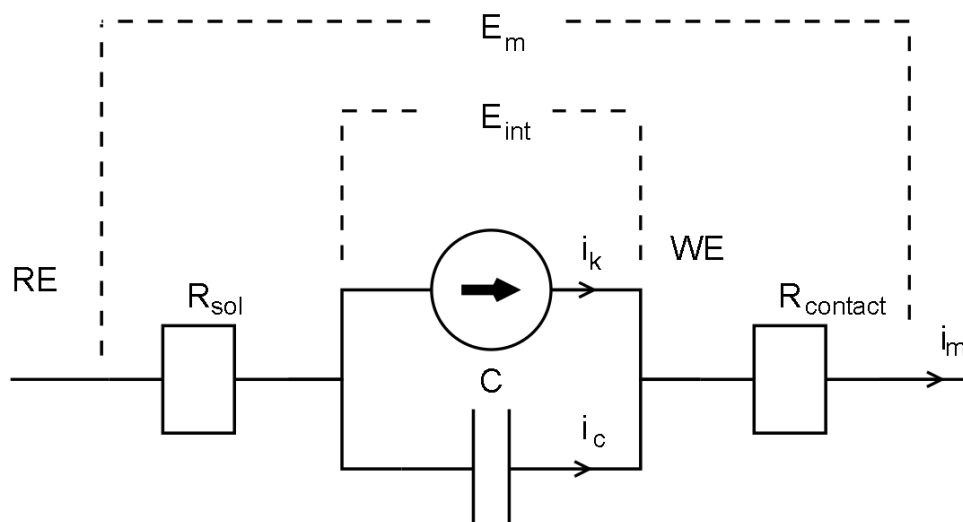
Figure 3.1-3: Scheme of the half cell model including a contact resistance between the working electrode and the potentiostat cable.

A large contact resistant may occur if the needle contact or the backside of the working electrode is corroded. Although these parts are never in direct contact with the acid or alkaline electrolyte, water vapour can enter into the cap and cause corrosion. This is almost impossible to avoid. Frequently visual and resistivity controls are therefore needed to ensure that the contact is low. If the spring contact is corroded, in the in-house design the inexpensive gold plated steel spring can be easily replaced. It is also advantageous of implementing a practice of repeatedly screwing a newly mounted tip in and out in order to remove corroded layers at the metal connection.

3.1.4.2 Lateral seal failure

The second issue with the RDE tips is that the lateral part of the working electrode cylinders can get in to contact with the electrolyte. The effect of such a contact is demonstrated in figure 3.1-4(A) where the cyclic voltammogram of two glassy carbon electrodes are displayed. In this potential window, no specific faradaic process occurs; hence the measured current is dominated by capacitive currents. Although having the same geometric size, the two electrodes exhibit quite distinctive behaviour. For the electrode GC2 the capacitive current is increased by a factor of 5, indicating that more than just the flat disk area is in contact with the electrolyte.

Furthermore, the capacitive current is superpositioned by a linearly increasing potential dependent offset.

A)

B)
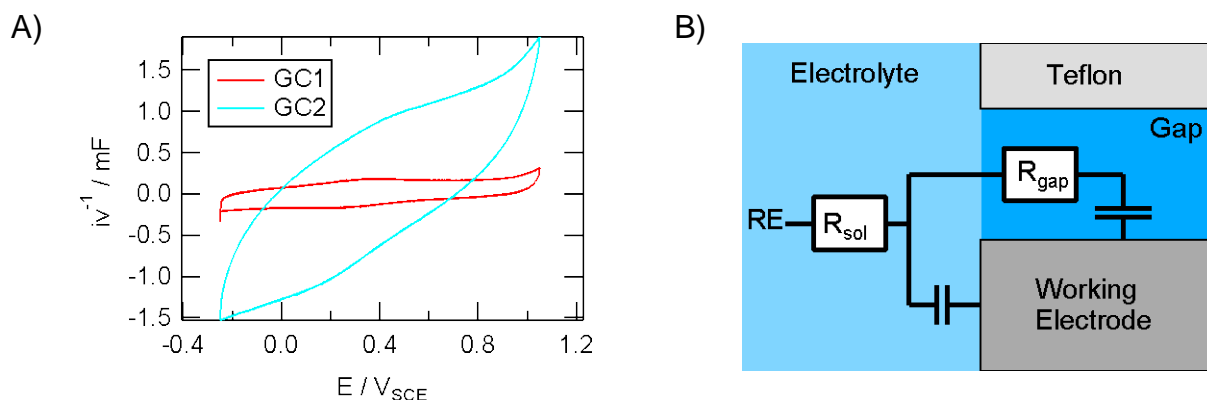
Figure 3.1-4:   A) Cyclic voltammograms of two bare glassy carbon electrodes in acid solution; one of the tips has a failed lateral sealing (blue line). B) Electric model of failed lateral sealing.

In the absence of any faradaic processes, the potential dependent offset can be explained by the electrical model shown in figure 3.1-4(B). The light blue colour symbolises the bulk electrolyte, while the dark blue symbolise the microscopic gap filled with electrolyte between electrode and the Teflon cap. In addition to the half-cell model in the absence of any faradaic process (light blue area), a resistor and a capacitor (dark blue) have been added to the model. The resistors symbolise the immobilised electrolyte in the gap, while the capacitor symbolise the newly contacted interface.

Given this model, the measured linear offset is due to the current passing through the gap, R_{gap}. Upon a potential sweep, the current cannot flow fast enough through the resistor. A potential difference therefore builds up between the bulk electrolyte and gap, which forces more current through as the voltage sweep continues. Taking the average between the positive and negative going sweep a straight line is obtained and the reciprocal slope constant corresponds to R_{gap}. An estimation of R_{gap} for both tips in figure 3.1-4(A) , results in a value of 60 kΩ and 0.6 kΩ for tip one and two, respectively. Ideally, the resistance should be infinitely large.

Seal failures are wear and tear and cannot be avoided. In the developed design, however, the glassy carbon (or metal) tip can be used further, by reassembling the tip and exchanging the Teflon cap.

Furthermore, it is possibility to extend the life time of a tip if the working electrode by coating it with an electrical isolation and chemical stable layer before assembling the tip. Such a coating can be made of epoxy adhesive or Teflon lubricant. The two component epoxy adhesive is easy to apply and the isolating coating is stable after drying so that the tip can be assembled as described above. In the second case, the Teflon lubricant is sprayed onto the electrode and a white dust is formed on the electrode. After heating the tip to about 250 degrees with a heat gun, the Teflon dust particles melt together and form an almost transparent layer. Over heating has to be avoided, as this can damage the Teflon and change its chemical and isolation properties.

3.2 Developed multi working electrode (MWE) array

The RDE is a useful tool for studying electrocatalytic reactions. One disadvantage for the study of nanoparticles high surface area catalysts, however, is the low sample throughput which complicates the statistical investigation of data. This disadvantage can be overcome by the use of multi working electrodes (MWEs). As such devices are not commercially available a MWE was therefore developed as part of this thesis. In general, the sample throughput rate of an electrochemical setup is not only governed by how many samples can be measured in parallel, but also the time it takes to exchange the samples and to perform another measurement. In that respect, the RDE setup, as previously described, is a good model. The easy assembly of the setup, as the RDE device enters the electrochemical cell through the lid, and the fast tip exchange are very advantageous. A similar system for the MWE would therefore be very beneficial. Hence, the MWE was designed with a shaft of exchangeable tips.

3.2.1 MWE tip

For the design of the MWE tip, several points were considered. Taking into account that the solution resistance is proportional to the distance of the working electrodes to the Luggin capillary, the electrode was designed as compact as possible. Additionally, by placing the electrode symmetrically around the Luggin capillary it was ensured that the electrodes have a similar solution resistance. Furthermore, the tip

should be easily attached to the shaft, favouring a screw system. The tip material has to be chemically stable both in acid and alkaline and easy to machine. As the primary use of the MWE is to facilitate the characterization of high surface area catalysts, the working electrodes should be of a chemical inert, conductive material.
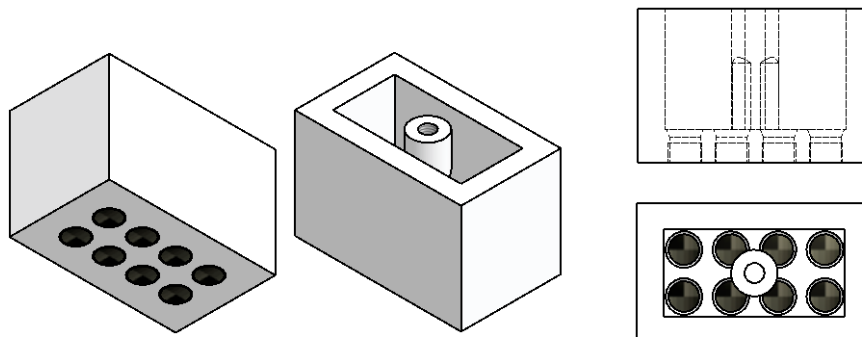
Figure 3.2-1   Drawings of the MWE tip from different angles

The MWE tip design developed in this thesis is displayed in figure 3.2-1. The tip composes of 8 working electrodes arranged in an (2x4) array. The electrical device does not have any restrictions on the amount of electrodes (see section "Multi-Working Electrode system"), but rather as a compromise between the number of samples and compactness of the MWE this number was chosen. In addition, this basic design facilitated the machining of the tip.

As working electrode material glassy carbon (GC) was chosen, as it is stable in both acid and alkaline solution. The GC electrode are cylinders d=5mm x h=3mm in size. Thus the same GC electrodes can be used in the MWE and RDE setup, facilitating the comparison of both methods.

The cap is made out of a Teflon block of the dimensions 21mm x 35mm x 23mm. The inside of the cap has been extruded, except for a cylinder in the middle, so that the tip can be mounted on the shaft top. The cylinder has a threaded hole in which a screw can attach the tip to the shaft. The diameters of the holes for the working electrodes are 4.6 mm, which is slightly smaller than the working electrode cylinders (d=5mm) and the next neighbour inter-hole distance is 7mm. On the inside of the cap, these holes are conical in order to facilitate the assembly of the tip and to ensure a proper sealing of the GC tips in the Teflon block.

The tip of the MWE is assembled similar to the previously described procedure for the homemade RDE tips. After heating the Teflon cap to about 250°C, the GC cylinders are inserted from the back side. Great care has to be taken that the cylinders are inserted straight. The heated Teflon is very soft and is easily irreversibly deformed. After cooling the latter seal might not hold. This will not only affect the experiment, see description in RDE tip paragraph, but might also lead to electrolyte flooding. The flooding could short circuit the electrical contact of the individual GC electrodes, resulting in incorrect current signals.

After its assembly, the height differences between the individual GC electrodes in the MWE tip has to be reduced. The tip might not be totally flat as the GC cylinders are larger than the holes, which slightly deforms the tip. Therefore, after assembly the tip is first polished with sand paper of different grain size and thereafter with aluminium oxide powders.

3.2.2 MWE shaft

The MWE shaft, similar to the RDE shaft, extends the tip so the setup can be introduced into the electrolyte. It also provides the electrical contact between the 8 working electrodes and a connector. The shaft consists of several pieces displayed in figure 3.2-2.
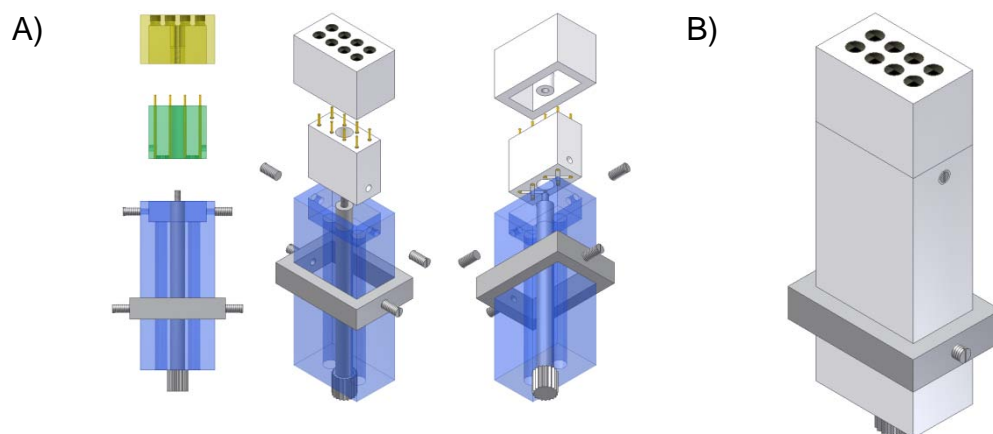
Figure 3.2-2:   Drawings of the MWE shaft assembly including the MWE tip

The main body of Teflon (blue) has an extrusion and three additional holes. Into the extrusion, another Teflon piece, the shaft top (green), is mounted and mechanically restrained in place by two countersinked Teflon screws. This piece has the same size as the inner diameters of the tip; hence it is used to hold the MWE tip. It has 8 holes

corresponding to the centre of the working electrodes of the tip. Into these holes the electric gold contacts are placed. In order to embed the electrical cables so that the shaft top piece can be fully inserted into main body extrusion, diagonal trenches are made from the holes to the closest off centred hole of the main body.

A centred hole is drilled through the assembly in which a PVC rod with a grooved head and a threaded tip is inserted. PVC was chosen for this piece due to its better mechanical strength compared to Teflon. With the help of the PVC rod, the tip can be screwed onto the shaft and be held firmly in place.

To ensure good electrical contact between the glassy carbon electrodes and the MWE device, 8 gold plated spring loaded steel pins pierce the backside of the working electrodes. The pins are mounted in receptacles which are soldered to a shielded electrical cable. Soldering the cables to the receptacles rather than to the pins enables an easy exchange of the pins in case of corrosion. Each cable runs in the trench to the centre of 4 pins. From here, the cables exit through one of the two holes in the shaft on either side of the rod. The cables end in a 9-pin D-sub (DE-9) connector, for the connection to the MWE device. Note that the two holes are placed in the centre of 4 contacts. Their diameter is smaller than the distance between the pins. As a result the pins are supported from the backside, as a reaction force must act upon the pin so that the pin head can pierce the working electrode.

Additionally, the immersion depth of the electrode into the electrochemical cell (see chapter 3.3.3) can be adjusted by the PVC rod, which can freely move along the shaft. Tightening of the two screws, fixes it to one position. When inserted into the lid of the electrochemical cell, the PVC piece blocks the shaft from further intrusion.

3.3 Electrochemical cells

The design of electrochemical cells can be rather simple and in some cases a standard glass beaker is adequate. More practical glass cells with holder for the different electrodes are commercially available [20]. Such cells are in many cases sufficient for the study of electrochemical reactions. For an accurate determination of fuel cell reactions, however, they are not suitable. Therefore, in this thesis several homemade electrochemical cells were designed and built.

Fuel Cell catalysts are in general very sensitive to impurities and even small amounts can greatly influence the determined activity [21-23]. The most common sources of

these impurities are the reference electrode, the counter electrode, the electrolyte and the cell material. Furthermore, the cell design and the inter electric properties between the electrodes (see previous chapter) can also have an influence on the measurement [24]. Thus a good cell design, which is optimized for a specific use, can considerably improve the quality of the measurements.

The design of new electrochemical cells requires the consideration of different design parameters. In general an optimum design is reached only by an "evolutionary try and error approach". In the following the different designs of electrochemical cells developed in this thesis are presented.

3.3.1 Glass RDE cell

The built electrochemical glass cell for RDE measurements is based on a common design of more advanced 2-compartment-glass cells. It was specifically designed for the EDI101 rotator and is schematically introduced in figure 3.3-1. As can be seen, the cell is composed of five separate parts. All parts are made of glass, except for the cell lid, which is made of Teflon.
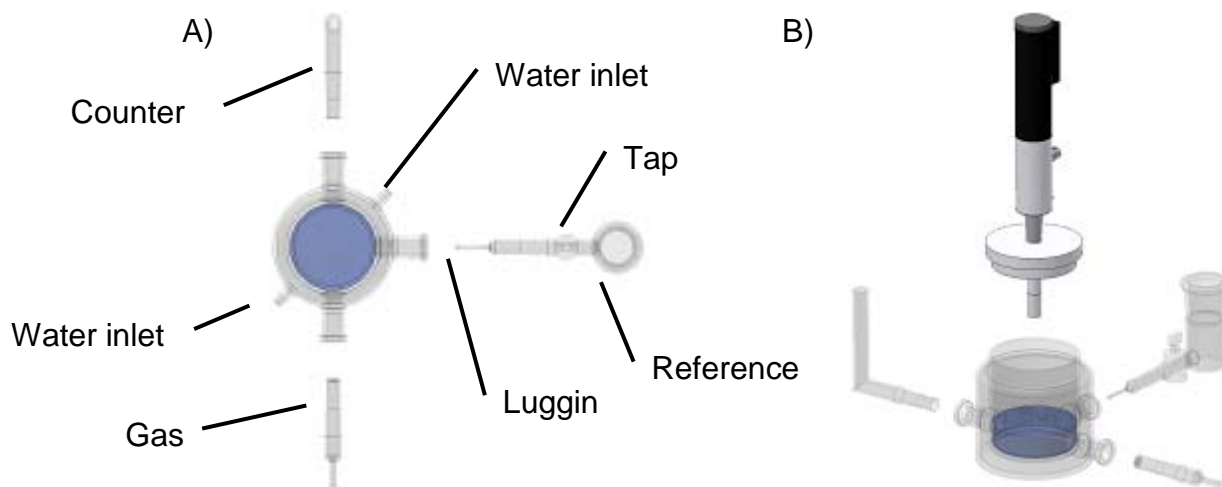
Figure 3.3-1: **Drawing of the electrochemical glass cell designed for RDE measurement.**

The working electrode on the rotating shaft of the RDE is held in the centre of the main compartment by the cell lid. The counter electrode is placed in the L-shaped glass part on the side of the cell. Furthermore, a glass tube with a porous glass frit is placed on the side, in order to saturate the electrolyte with different gases. The elongated tip of the reference compartment ends at short distance to the working

electrode. The closed tap impedes the diffusion of ions from the electrolyte of the reference electrode to the main compartment. The elongation of the reference compartment is referred to as the Luggin capillary [12, 16-17]. As no current passes through the capillary and the reference electrode, only the electrolyte between the end of the tip and the surface of the working electrode contributes to the solution resistance of the cell. In addition, the cell has a water jacket; hence the cell temperature can be controlled by a thermostat.

Most electrochemical cells are made out of glass. Although it has several advantages, such as being easy to clean and transparent, it has some disadvantages as well. From a constructional point of view, for an electrochemical cell different glass pieces must be molten together and bent into the special shapes. The manufacturing of these advanced glass cells is difficult and time demanding, and less accurate than mechanical machined parts. Thin glass pieces are also very fragile and can easily break. From an electrochemical point of view, glass has the disadvantage of not being stable in alkaline solution. In work connected to this thesis, it could be shown that in alkaline solution small amounts of silicates and metals ions are leached out of glass into the electrolyte. It was demonstrated that even such small amounts of impurities can considerably influence the measured reaction rates [22-23]. Hence, an alternative material for electrochemical cells was needed.

3.3.2 Teflon RDE cells

Teflon is a material with excellent chemical stability in both acid and basic solution. This makes it more suitable for our experimental requirements. Furthermore, in contrast to glass, Teflon parts can be mechanically machined with high precision from a Teflon block. This enables the fast and easy production of different, customised cells.

3.3.2.1 RDE cell version 1

The first version of the all-Teflon cell developed in this thesis is almost a direct copy of the glass cell, see figure 3.3-2. A difference, however, is that the water jacket has been removed because the machining of such a piece is very problematic. Another change is that the tap on the reference compartment is removed as well. The hydrophobic nature of Teflon caused considerable problems. A closed tap resulted in

a too large resistance between WE and RE which hindered the potentiostat to operate.
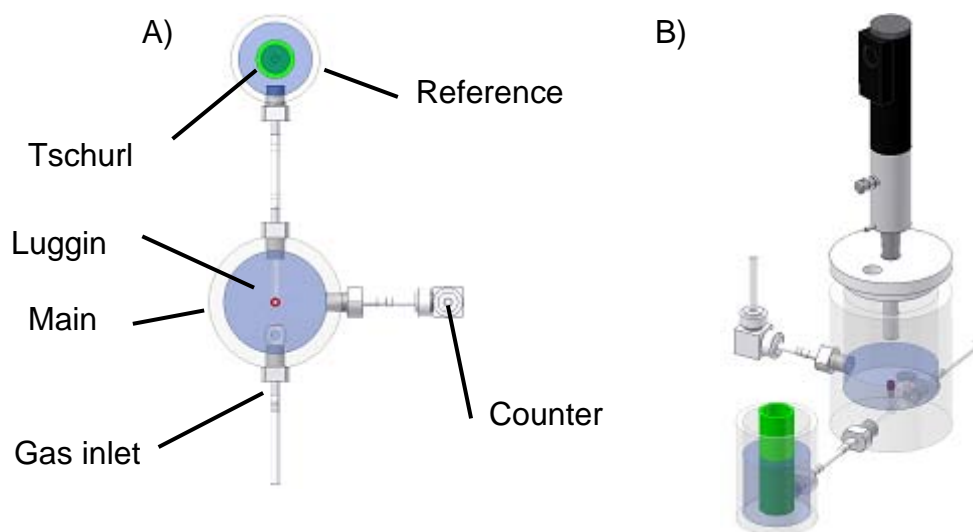
Figure 3.3-2: **Drawings of the RDE Teflon cell design version 1. The cell is a Teflon adaptation of the glass cell.**

Furthermore, the conically tapered joints, often used in glassware, are not feasible for Teflon. Therefore, the different compartments are connected by Teflon pipes and tubing connectors with threads.

The Luggin capillary (red) is integrated in the main compartment, rather than being a part of the reference compartment. The pipe is positioned in the centre of the cell, underneath the working electrode, and a horizontal hole connects it to the reference compartment.

In order to inhibit diffusion between the main compartment and the reference electrode, an additional Reference electrode side compartment is placed into the reference cell compartment [25]. This is the green object depicted in figure 3.3-1 (See chapter Reference electrode side compartment).

In the absence of a water jacket, a new solution for temperature control is required. For this purpose a direct heating device consisting of a Teflon encapsulated heating coil entering the cell from the lid was designed. A digital temperature control unit manages the current through the heating wire using a Teflon coated standard thermal sensor (Pt100) [26]. A drawback of this setup is that the cell lid gets crowed with cables. Another drawback is that only the main chamber gets heated, similar to the case using a water jacket. As a result of heat diffusion to the reference

compartment, the temperature of the reference electrode might be deviate from room temperature and a careful adjustment of the reference potential is necessary.

A major source of electrical noise in the measured signals is due to the purging of the electrolyte with gas. Significant improvement is observed if the gas purging is turned off, especially if small currents are measured.

There are several weaknesses with this cell design: i) The cell has a relative large cell volume and for measurements, at least 150ml of electrolyte is required of which more than half is located in the reference compartment; ii) the large distance between the electrodes results in a high resistance, requiring more operation power of the potentiostat, which can cause artefacts [24]; iii) the cell is not a closed system and small amounts of impurities could enter. Therefore, the design was improved in a second version of the electrochemical cell.

3.3.2.2 RDE cell version 2

The main aim of this improved version of the electrochemical RDE cell was to reduce the cell volume compared to that of RDE cell version 1. Rather than continuing to optimise the design of the assembled cell type, we decided to design a totally new type where all the compartments are extrusions from the same block of Teflon. An advantage of a one-block-cell design is that the Teflon pipes and tubing connectors are no longer needed, which reduces the overall space needed for the cell. Additionally, the cell becomes very easy to handle as the amount of moveable parts are reduced. The realised 2-compartment cell is shown in figure 3.3-3.
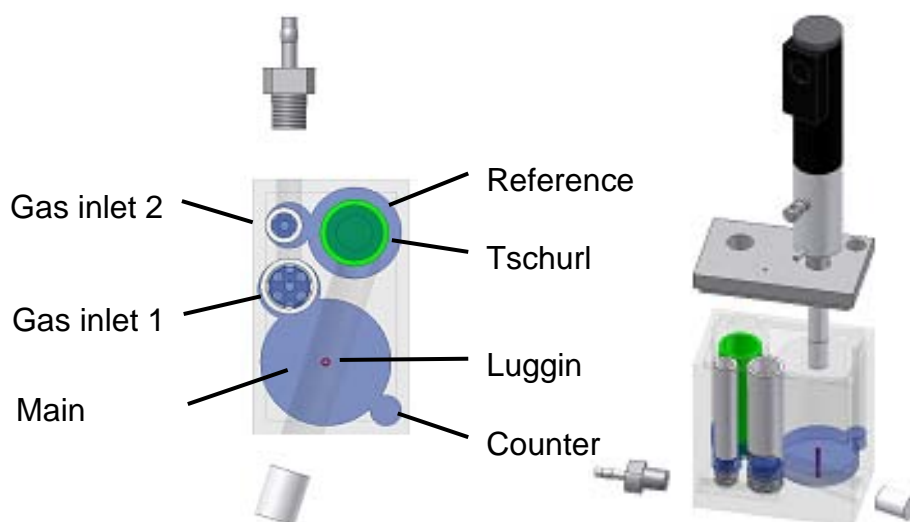
Figure 3.3-3: **Drawing of the RDE Teflon cell design version 2. All compartments are made out of one block of Teflon which results in a very compact design.**

Two vertical main holes are drilled into the cell body to be used as compartments for the working and reference electrodes. A small Teflon pipe (red) in the middle of the main compartment acts as Luggin capillary. The capillary is connected to the reference compartment via a horizontal hole. The entrance of this hole at the side of the cell is sealed so no electrolyte can exit. The counter electrode is placed in a small semi-circular hole.

The two gas bubblers for saturating the electrolyte with a specific gas are made of two vertical holes entering each compartment; one for the main and one for the reference compartment. The holes are horizontally connected to each other by an inlet into which a tubing connector made out of Teflon is screwed in. The purging gas passes through a piece of porous Teflon before entering the electrolyte. In addition, a semi-cut Teflon pipe hinders gas bubbles to enter the main compartment.

This cell has a significant smaller cell volume than version 1. Only 40ml of electrolyte is needed, a reduction of 70%. Another advantage of this cell is that all compartments are purged with the same gas, which should reduce the amount of air entering the cell. However, after continuous Ar purging in some cases traces of oxygen could be still detected. A possible reason might be gas evolved at the counter electrode during

the measurement. Therefore a third design of the all-Teflon electrochemical cell was developed.

3.3.2.3 RDE cell version 3

In this version of the electrochemical all-Teflon RDE cell, the focus was to build a 3-compartment cell and to implement a temperature control by a heating bath. In order to avoid any impact of gas evolution on the counter electrode, a separate counter compartment was implemented into which a Tschurl compartment can be placed. The whole cell can be placed into a large beaker filled with water, which facilitates the heat control as an ordinary heating plate can be used. The resulting design can be seen in figure 3.3-4.
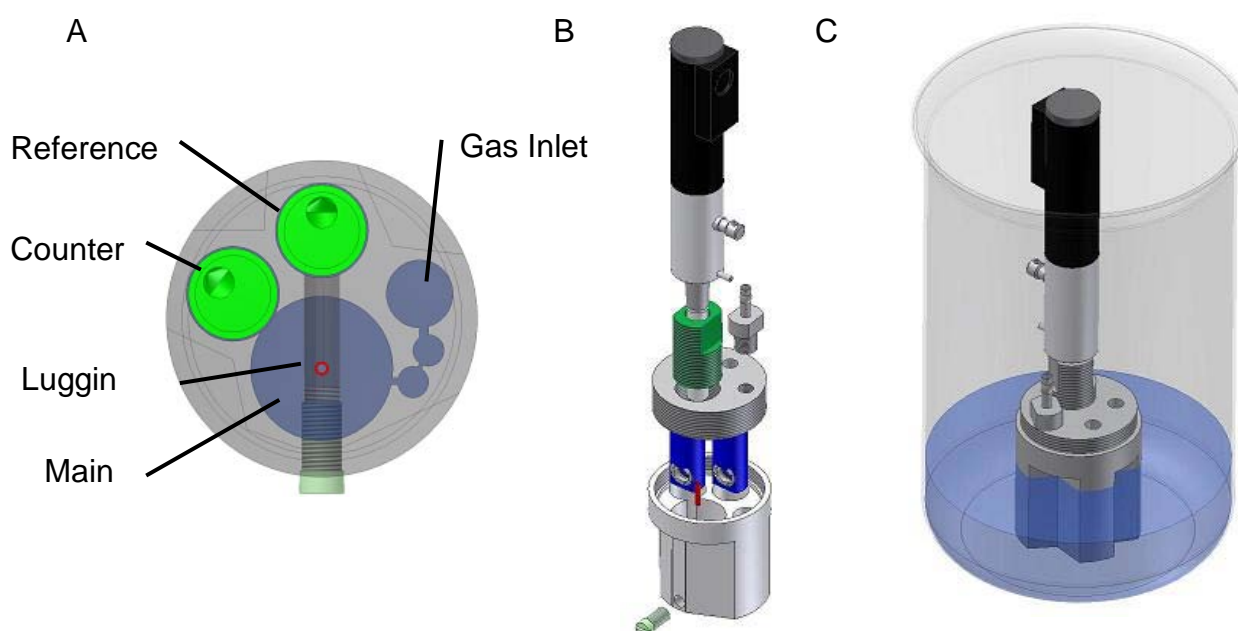
Figure 3.3-4:   Drawing of RDE Teflon cell design version 3. The cell is a membrane separated 3-compartment cell designed to be used in a heat bath.

The design is similar to the RDE cell version 2 as it is machined from one Teflon block. The compartments are interconnected to each other via a small hole in the middle of the main compartment which also acts as Luggin capillary. A modified Modified Tschurl compartment (green) is placed in the reference compartment. An additional third compartment is placed in the semi-hole, tangent to the main compartment. Here the counter electrode is placed.

All compartments are positioned as close as possible together in order to minimise the cell volume as well as the resistance between the electrodes. The cell requires about 40ml of electrolyte for operation, which is similar to that to RDE cell version 2.

A new feature of this cell version is that in order to make the cell more robust the lid is screwed onto the main body. Furthermore, the RDE can be adjusted in horizontal direction. The vertical distance of the working electrode to the Luggin capillary can thereby be optimised after cell assembly, thus minimizing the solution resistance without introducing a disturbance to the convection of the electrolyte.

The inlet of the gas purging is placed in the cell lid in order to make the cell fit into a beaker. Gas enters the electrolyte through a Teflon pipe in a side compartment, which is connected to the main compartment by a series of holes which should avoid turbulences in the electrolyte. As all compartments are connected under the lid, all experience the same atmosphere.

Teflon has a large heat capacity. In order to avoid a sluggish response of the electrolyte temperature to the water bath, the heat capacity of the cell was minimized. The cell walls are made very thin (2 mm) and any "dead weight" is cut away. As a consequence, the cell obtained an edged form of the lower parts, see figure 3.3-4(B). Figure 3.3-4(C) shows the assembled cell together with the RDE in a water beaker. Using a heating plate it takes about 15 min to heat the electrolyte from 25°C to 60°C.

3.3.3 Teflon MWE cells

The MWE array is not directly compatible with the previously presented designs of the RDE cells due the rectangular electrode array. As a consequence a modification of the design for an electrochemical MWE cell was required.

A general problem in using a MWE array is that the experimentally important convection of the electrolyte to the electrode cannot be generated by rotating the electrode. In contrast to the RDE, the shaft of the MWE is mechanically fixed. Instead of rotating the working electrode, convection of the electrolyte could be generated by a mechanical stirrer. However this would require a complicated setup. Instead, a magnetic stirrer was used, which was placed underneath the electrochemical cell.

3.3.3.1 MWE cell version 1

In its first version, the MWE cell design was based on RDE cell version 1, which was adapted to the MWE array. Further modifications were needed in order to implement the magnetic stirrer. The cell design is shown in figure 3.3-5.

With its increased size compared to the RDE, a centre position of the MWE array in the main cell chamber would result in decreased distance of the gas inlet to the working electrodes and thus the Luggin capillary. This could yield to distortions when purging the electrolyte. Therefore, the Luggin capillary (red) was shifted off centre to maximise the distance between the gas inlet and the MWE. Additionally, two holes have been placed in to the bottom of the main body to place the magnets in. The holes are located directly underneath the MWE, to create a strong and relative steady convection of the electrolyte. Rather than using standard Teflon coated magnetic rods, a cylindrical Teflon casing for the rod was designed, which fitted perfectly into the holes. Thus the "wobbling" of the stirrer at high rotation rates was minimized. Furthermore, the convection of the electrolyte to the electrode surface became more uniform as the rod consisted of several "blades" in contrast to standard magnetic rods.

The lid of the cell was re-designed as well. The rectangular extrusion of the lid is positioned in way that the centre of the MWE array is placed directly above the Luggin capillary.
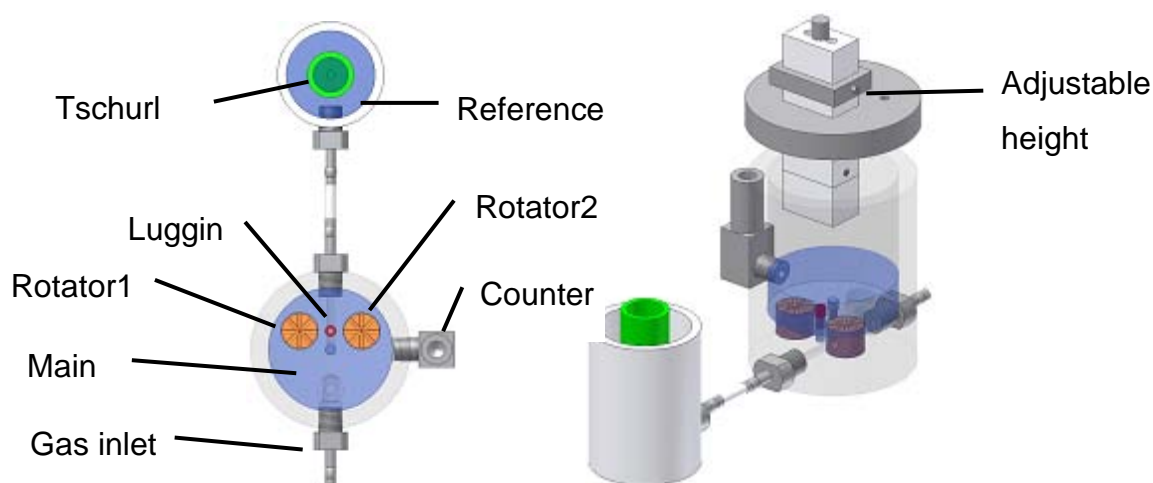
Figure 3.3-5:   Drawings of the Teflon MWE cell design number 1 - an adaption of the Teflon RDE cell model version 1 to the MWE.

With this cell design, measurements under similar conditions as in a RDE setup could be performed. For example, by a rate of 1000 rpm by the magnetic stirrer the average diffusion limited current in ORR measurements was equivalent those measured in a RDE setup at 1600rpm. The individual diffusion limited currents at the MWE electrodes, however, showed differences up to 50%. Furthermore, the noise level is in the current signal was significant larger than in the RDE setup.

It was found that the noise was strongly influenced by the magnetic stirrer, as well as the angle between the pipe leading to the reference compartment and the radial vector from the centre of rotation magnet.

The noise was could be minimised if the cell was placed in such a way that the pipe had a 90°-angle to the radial vector. This can be explained by a Lorenz force acting on the ions [27]. The magnetic field of the stirrer induces oscillations in the radial direction of the ions in the pipe. The ion movement invokes an oscillating potential drop between the reference electrode and the working electrode. Although a potential error is induced, the feedback system forces a current through the working electrode in order to cancel out the disturbance. Hence, the disturbance is observed as an oscillation of current.

With the help of the adjustable shaft of the MWE, the solution resistance could be minimised. In 0.1M perchloric acid, the typically obtained resistance is 2Ω, although in some cases values of up to 20Ω were determined. These deviations most likely can be related to a contact resistance to the electrode back side. They cause relatively large systematic errors as the MWE device cannot be electronically compensated for the resistance. Furthermore, it was observed that the resistance of the electrodes closer to the counter electrode is smaller than for those further away. The addition of supplementary counter electrodes to the setup, which were located close to the MWE, reduced the differences.

3.3.3.2 MWE cell version 2

The aim of this improved cell design was to solve the problems identified for the MWE cell version 1. In addition, a temperature control of the electrolyte and a 3-compartment cell was introduced as well as the overall cell volume was reduced. The cell design can be seen in figure 3.3-6.
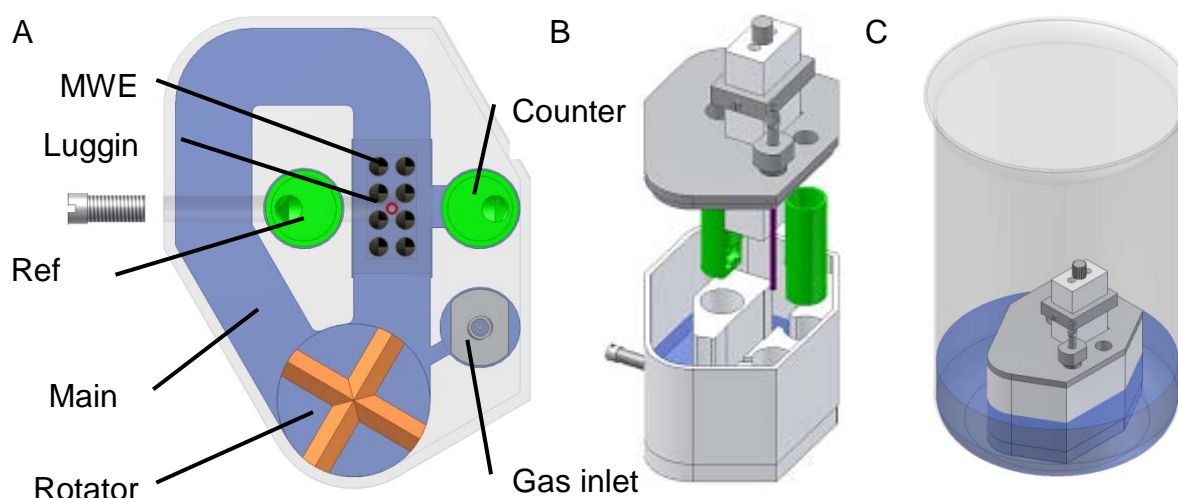
Figure 3.3-6: Drawings of the Teflon MWE cell design version 2. The cell is a membrane separated 3-compartment cell designed to be used in a heat bath.

The cell design includes many features of RDE cell version 3. The cell is made out of one Teflon block. Both the counter and the reference electrodes are placed in removable modified Tschurl compartments (green), which are placed in the holes, positioned on each side of the MWE array; the reference compartment to the left, the counter compartment to the right.

In order to reduce the fluctuation of the diffusion limited current resulting from non uniform electrolyte convection, the small stirrers were exchanged by a large one. During rotation the electrolyte flows in a channel loop in clockwise direction before reaching the electrode in order to reduce turbulences. Thus the electrolyte convection becomes more laminar before reaching the electrodes.

In order to reduce the current oscillation due to the rotating magnetic field, the Luggin capillary (red) and the reference compartment, are placed in a way such that the channel between them is directed transient to the rotation of the magnetic field, which is centred underneath the magnetic stirrer.

The gas inlet and all electrical cables enter the cell from above as shown in figure 3.3-6(B). The cell can be placed in a large water beaker where the temperature can be controlled by a heating plate. Thus a combined heating and magnetic stirrer device can be used. The cell walls are made very thin (~3mm) in order to enhance the heat transfer through the cell walls. Also the amount of electrolyte required to operate the setup is reduced to about 70ml. This is about 50% less than in the

previous version, MWE cell version 1. This reduction could be achieved by the removal of the external reference compartment. Using this cell design catalytic measurements with the MWE setup could be performed under similar conditions as those in a RDE setup. Measuring the ORR, it was observed that a maximum electrolyte flow is already reached at a rotation of the magnetic stirrer of 600 rpm. Higher rotation rates did not increase the diffusion limited current, which equals the one obtained in a RDE setup at 900 rpm rotation speed. Although this is slightly lower than the limiting current obtained in MWE cell version 1, the differences of the individual electrodes were significantly smaller. Furthermore, the current fluctuation resulting from the magnetic stirrer is significantly reduced as a lower stirring rate can be used and the magnet is placed perpendicular to the cell connection between Luggin capillary and reference electrode.

The typical solution resistance using 0.1 M perchloric acid in this cell is 10 Ω. However, the working electrodes which are situated close to the counter electrode exhibit in general a significantly smaller value than those working electrodes in the second row.

3.3.4 Reference electrode side compartment

In an electrochemical glass cell, a closed electrolytic bridge between the reference compartment and the main compartment can be used in order to reduce the diffusion of chloride ions from the reference electrode into the main compartment, while still providing electrical contact. In the case of an all-Teflon cell, because of the hydrophobicity of Teflon a closed electrolytic bridge does not provide sufficient electrical contact between the two compartments. As an alternative diffusion barrier for the chloride ions in the reference compartment in this work a Nafion membrane was utilised. The conductivity of the membrane is sufficient to provide an electrical contact, but blocks any convection between the cell compartments. The attachment of a Nafion membrane to a small Teflon vial, was coined as a Tschurl compartment [25].

3.3.4.1 Tschurl compartment

The first version of a Tschurl compartment is shown in figure 3.3-7.
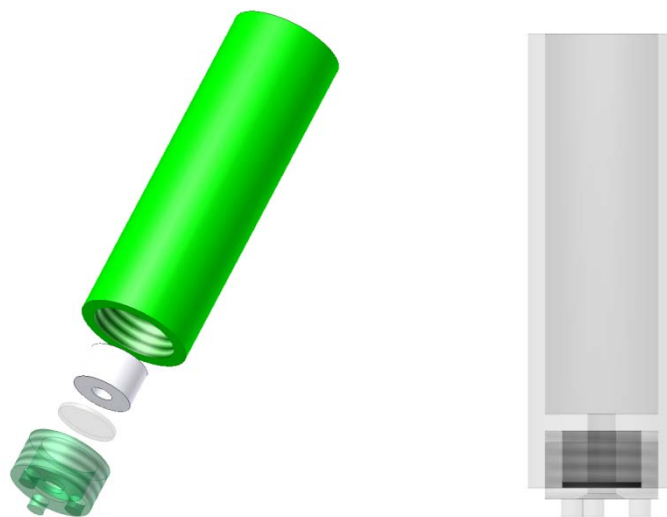
Figure 3.3-7: Drawings of the Teflon made Tschurl compartment. A Nafion membrane is separating the inner compartment from the outside in order to reduce the diffusion of larger ions although permitting good electrical properties.

The Tschurl compartment is composed of a Nafion membrane and 3 Teflon parts, i.e. the main compartment, the screw-in bottom and the spacer. The parts are assembled as shown in figure 3.3-7. By screwing in the bottom, the Nafion membrane is tightly pressed against the main body, thus preventing any electrolyte flow. The "legs" on the screw-in bottom guarantee that enough electrolyte is located between the bottom of the Tschurl compartment and the reference compartment of the cell into which it is introduced. This should ensure that a loss of electrical contact is avoided. The measurements showed that nevertheless in some cases an air bubble was trapped below or above the membrane, which lead to a loss of electrical contact.

3.3.4.2 Modified Tschurl compartment

In order to reduce the occurrence of such air bubbles, a new design of the Tschurl compartment was adopted, as shown in figure 3.3-8. This new design also allowed the use of the Tschurl compartment in the RDE cell version 3 and the MWE cell version 2.
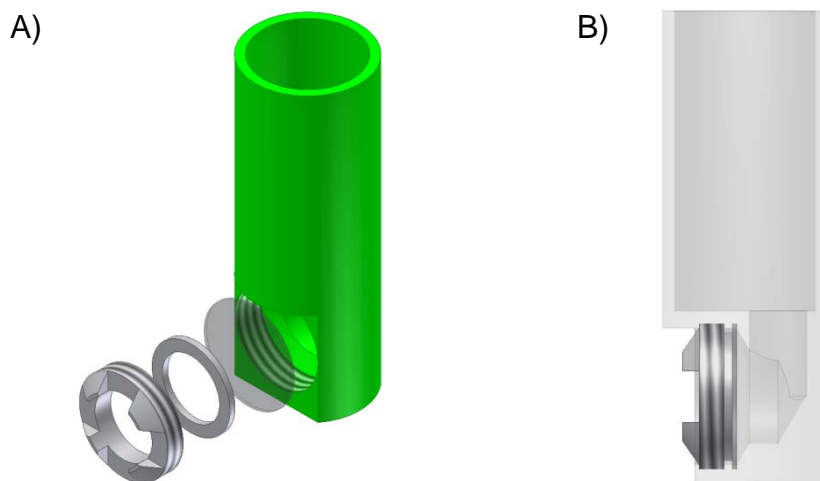
Figure 3.3-8: Drawing of a modified Tschurl compartment. The position Nafion membrane is altered and position vertically in order to avoid the trapping of bubble.

The main difference to the first version is that the membrane is vertically positioned in the compartment, which allowed wider holes and inhibited the trapping of air bubbles.

3.4 Automatic gas changer

For a complete electrocatalytic characterization of a fuel cell catalyst in a RDE or MWE cell, the electrolyte has to be saturated several times by different gases, such as O_2, Ar, H_2, CO. A computer controlled gas changer for the purging gas thus can greatly reduce the time demanding manual work during the measurements. Furthermore, the reproducibility of the measurements can be greatly enhanced as programmed measure protocols can be executed, which guarantee that always the same procedure is used in a catalyst characterization. A complete commercial gas changing system suitable for our setup was not available. Nevertheless, a large market exists regarding gas and gas flow elements; hence the gas system could be build in-house by combining several commercially available elements.

For our purpose only a gas selection device without gas mixing was required. Hence bipositional gas valves, which start and stop the gas flow in each gas line, are sufficient for the setup. In order to incorporate them into the existing setup, the gas

valves should be monitored by a digital electrical control system. For the flow rate of the gas no computer control was required, as only a fixed flow for the different gases is used which should be constant in time. As a result of the single gas inlet in the electrochemical cell, the different gas lines have to be joined before the inlet. Thus a single control device which fixes the gas flow was sufficient.

A multi position valve was chosen rather than several bi-positional devices. The multi position valve has a fixed housing with several gas inlets and one outlet. Inside the valve is a movable cylinder with holes. Depending on the position of the cylinder, a hole interconnects a certain inlet with the outlet. The cylinder is turned and positioned by an electrical step motor with gear box, and an actuator which can be controlled by computer.

There are various gas flow controllers commercially available. One of the properties to be considered is whether the mechanical flow controller should use up-stream or down-stream pressure as reference. In our case, the gas is provided from gas bottles with pressure reducers. The gas lines are relatively long and the pressure in the respective lines can differ. As the gas pressure and flow at the inlet of the electrochemical cell should be stable, a flow controller with a feedback reference pressure in the downstream was preferable.

The knowledge of the exact flow rate of the gas, however, was not crucial. Therefore a basic analogue flow meter was sufficient, such as the rotameter used in the setup.
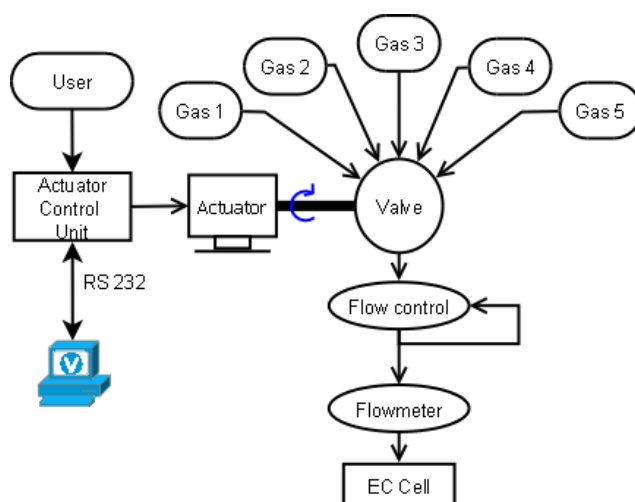
Figure 3.4-1:   Schematic outline of the assembled gas changer system.

The schematic outline of the gas system design can be seen in figure 3.4-1. All gas sources are connected to the valve inlet, while the flow control in connected to the

outlet. Further downstream the flow meter is placed. The system uses a flow controller (model 300) and gas actuator (Microelectric actuator) with a multiposition valve (6 positions) from Vici AG. The actuator has a control module with both a user interface and a RS-232 interface for computer control. The flow rate is adjusted manually. The flow meter is a "Mini-Master" from "Dwyer instruments inc.".

A drawing of the build gas changer built in this thesis is shown in figure 3.4-2. All parts are attached to an underlying board. On the front panel are the user-interface of the actuator control module, the analogue flow controller as well as the flow meter attached. The gas changer can thereby also be manually operated.
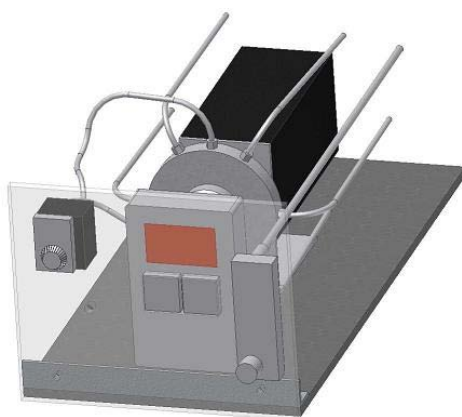
Figure 3.4-2: **The drawing of a gas changer, assembly of an electronic controlled gas actuator, flow control and a flow meter.**

3.5 The potentiostatic measure system

3.5.1 Measure system

In electrochemical experiments an active measure system is used. In other words, a black box, i.e. the partly unknown physical system of interest, is actively perturbed and the response is recorded. Thus a more complete understanding of the physical system can be established. For the EC setup, the system is divided into three parts as shown in figure 3.5-1: the voltage perturbation source, the potential control device connected to the EC cell and the recorder device. It is therefore important to keep in mind that any element in the "black box" can be the origin of a certain response. Hence it is important to understand each element of the measure system and its limitations.
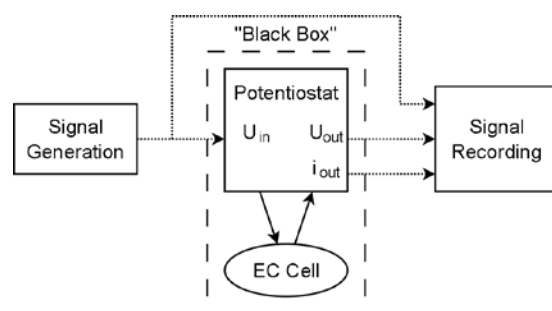
Figure 3.5-1: **Outline of an active electrochemical measure system comprising a signal generator, a "black box" and a signal recorder.**

3.5.1.1 Perturbation signal generation

Prior to the digital era, analogue signal generators were used to generate the perturbation signal. As a result of their complexity in design and construction, these devices were limited to only a few specific perturbation techniques which can be easily generated in an analogue way (square waves, sinusoidal etc.).

With the introduction of fast digital-to-analogue converters (DAC) with high resolution, virtually any arbitrary analogue waveform can be generated. This is a great advantage for the electrochemist because a whole range of perturbation techniques is nowadays available without supplementary investments in hardware. Several techniques can easily be super-positioned, which decreases the time of sample characterisation and results in an increased amount of information about the measured system.

3.5.1.2 Signal monitoring

Each perturbation technique has a characteristic signal response with corresponding key values; hence the visualisation of the measured data must be done with respect to the specific technique.

Similar to the case of signal generation, the development of high speed analogue-to-digital converters (ADC) with high resolution made analogue instruments for monitoring redundant. For example, formerly a CV was visualized with a XY-plotter, while the current transient after a potential step was better observed on a standard plotter. Furthermore, with a sinusoidal signal of a specific frequency, it is only the amplitude and phase of the response signal that is of interest and not the real signal.

Hence, these values have to be extracted prior to the visualisation. With an ADC, once the measured signal has been digitalized, the data can be mathematical filtered. Albeit several perturbation signals are superposed, data treatment can extract the key values. The key values can then be displayed in a suitable manner.

3.5.1.3 Potentiostat

A potentiostat is an electric device that can replicate an input signal to a perturbation of the interfacial potential of the working electrode. The current-potential response is monitored in order to elucidate the characteristics of the system. Physical constraints of the potentiostat can cause measure artefacts, hence being aware of their limitation is vital for correct measurements.

The potentiostat operates by sending a variable current through the counter electrode to the working electrode. At the same time the voltage between the Reference contact and the WE is measured. The current source is controlled by a feedback loop, see figure 3.5-2 and figure 3.5-3, which enables either the control of the voltage (potentiosatic mode) or the current (galvanostatic mode). In the potentiostatic mode, the supplied current is adjusted until the E_m equals the desired voltage E_{want}. The current-potential relation of the WE with the respect to the RE can thus be measured disregarding the potential needed to drive the current between CE and WE.
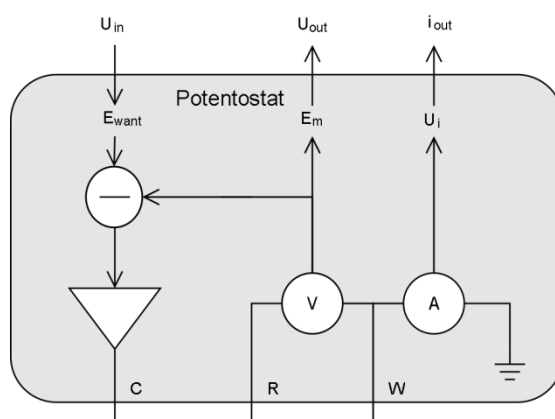
Figure 3.5-2: **Scheme of the control system of a potentiostat in potentiostatic mode. The voltage difference between the working and reference electrode is fed back.**

Alternatively the potentiostat can operate in the galvanostatic mode. In this mode, instead of the voltage the measured current (U_i) between the WE and CE is fed back into the control loop, i.e. the potential between WE and CE is adjusted until the desired current flows through the system.
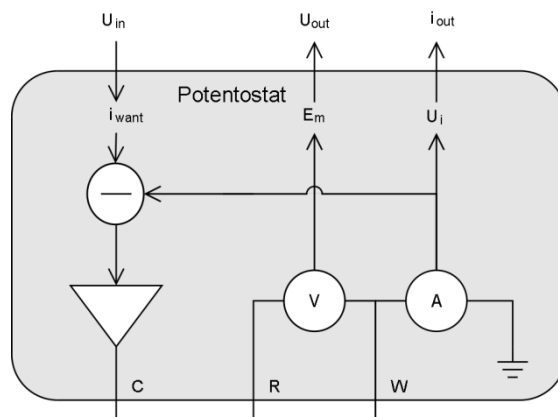
Figure 3.5-3:   Scheme of the control system of a potentiostat in galvanostatic mode. A voltage representation of the current is fed back.

3.5.1.3.1 Solution compensation

As described in the chapter "Theoretical aspects of the electrochemical setup", in a three electrode setup the interfacial potential difference cannot be directly measured. Instead, E_m is shifted by a quantity corresponding to the potential drop of the solution resistance between reference and working electrode. Several steps, e.g. using a Luggin capillary, can be taken in order to minimise the solution resistance. Nevertheless for highly accurate measurements an electrical potential compensation is indicated to further reduce the voltage divergence.

56
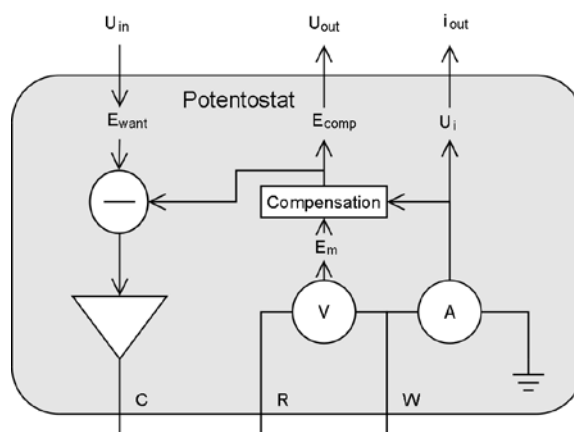
Figure 3.5-4: **Scheme of the control system of a potentiostat with an additional loop for compensating the solution resistance in potentiostatic mode.**

The compensation operates by adding a voltage quantity to the measured potential difference in such a way that it cancels out the expected solution resistance. The resulting E_{comp}, instead of E_m, is then fed back into the control loop, as shown in figure 3.5-4.

In order to evaluate the required compensation voltage, there are two main schemes available: the positive feedback and current interrupt scheme.

Positive feedback

The most straight forward compensation scheme is the positive feedback. Given that the measured current is converted in the measure system into a voltage, a quantity of this voltage corresponding to a negation of the expected potential drop of the solution resistance is added to the measured voltage.

The advantage is that a rather simple electronic circuitry can be used in order to implement this scheme in the potentiostat. Furthermore, it operates reliable even at high scan rate / high frequencies. In addition, the effective solution resistance, i.e. the part of the solution resistance that is not cancelled out, can be determined during the measurement thus indicating to the user if the compensation scheme works. The drawback, however, is that the solution resistance has to be determined prior to an experiment, which should not be changing during the course of a measurement.

Current interrupt

With the current interrupt scheme, the potential drop over the solution resistance is measured and feed into a control loop; hence no prior knowledge of the solution resistance is needed. This method is very useful if the solution resistance changes largely over time, which is the case for example in dropping mercury electrode (DME) experiments.

The potential drop over the solution resistance is measured as the difference of the measured potential prior and after a current interrupt. Hence, a relative complex circuitry is needed as the compensation signal is desecrated in time. In general the method has an updating frequency in the order of 100 Hz or less [28]. It is therefore not adequate for measurements at scan rates above 100mV/s. Furthermore, large capacitances of the EC cell can interfere with the accuracy of the method and hence it should be used with care.

3.5.1.3.2 Technical difficulties of potentiostats

The feedback based control system of the potentiostat can generate problems. Not only can measure artefacts be created, but in some cases it can lead to damage or even destruction of the electrodes.

Measure artefacts can be created due the power limitation of the potentiostat. If the potentiostat is not powerful enough, the required potential cannot be supplied to the CE in order to adjust the desired potential difference between WE and RE. With potentiostats that only measure the current signal, this potential artefact is in general not noticed by the user.

Furthermore, it is vital that the RE and the CE have good electrical contact. If the contact is lost, the current adjusting the desired potential difference between WE and RE is not controlled anymore. In such a case, the potentiostat will supply its maximum voltage/power to the system and can cause considerable damage to the working electrode.

Additionally, the potentiostat can start to oscillate. In such a case the potential control is lost, which can damage the working electrode as well. Oscillations can occur if the solution resistance between reference and working is too small or if the applied positive feedback compensation is too large.

3.5.2 Commercial measure system

Analogue potentiostats have been on the market since the 1970s, and in order to complete the measure system (see figure 3.5-1), additional instrumentation was required. Beside the signal generator, plotters or oscilloscopes were needed as well.

In later years, in commercial potentiostats the signal generator was integrated into the device in order to reduce the amount of different instruments. With the introduction of affordable high resolution and fast DAC and ADC fully computerised systems became available. Although the design and control of such an apparatus requires a skilled programmer, the development of the software and computer interface resulted in "plug-and-play" electrochemical setups.

On the other hand, the integrated system limits their customization. As all components are integrated, in general the computer controlled measurements have to be performed using the software developed by the manufacturer. These programs are often inflexible and can seldom be customized in order to incorporate additional devices such as gas changers or temperature control units if these items are not provided by the same company.

In addition, the intersystem data exchange is often problematic too. The software restrains the user to only the mediocre data analysis software of the potentiostat developer, rather than a specialized data analysis program with a wide range of features.

In order to set up a fully computerized experimental platform, it is vital that all the different systems; gas change, temperature control etc. are compatible, both on hardware and software level. A commercial measure system would consequently not be suitable.

3.5.3 In-house developed measure system

Due to the limitations of the commercial system discussed in the previous section a measure system was build in-house. The schematic outline of the system is shown in figure 3.5-5. As signal generator and recording device, a commercial DAQ card from National Instruments was chosen. In order to produce the perturbation wave and monitoring the experiment a software based on Labview was developed (See chapter 4. Software development for more details).
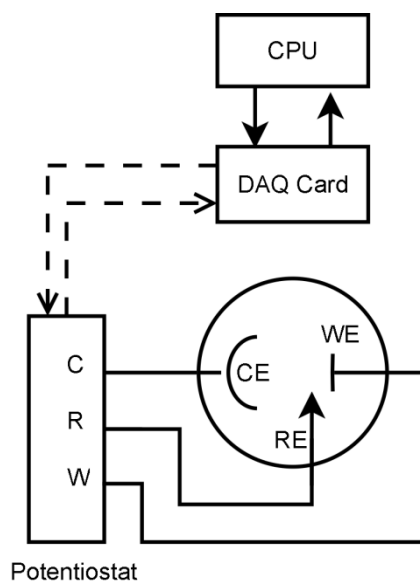
Figure 3.5-5:   Outline of the setup for electrochemical measurements.

An advantage of the chosen layout is that it permits any potentiostat with analogue in and out channels to be used. This was a requirement as two different commercial potentiostats were already at our disposal: the semi-digital Princeton 263A and the analogue Bank POS2. Additionally, the flexible design facilitated the implementation of the in-house developed potentiostats.

The reason for developing an in-house build potentiostat was that the performance of the two commercial potentiostats at our disposal; the semi digital Princeton 263A and the analogue Bank POS2 Potentiostat, was not entirely satisfactory. For example, POS2 lacks an adequate solution resistance compensation scheme, whereas the semi-digital 263A exhibits only a digital positive feedback compensation as well as a current interrupt system. In the typically performed RDE measurements, the current interrupt scheme does not offer an adequate compensation. It was found that the measurements with and without active compensation only differed by a current independent potential offset. The reason for this abnormal behaviour could not be determined. Applying a solution resistance compensation via the positive feedback scheme was feasible, although it was sometimes randomly switched off despite the fact that the potentiostat indicated it to be active. Furthermore, the updating rate of the DAC responsible for the compensation is below 1 kHz, hence the effective solution resistance cannot be monitored in-situ, i.e. during the measurement.

60
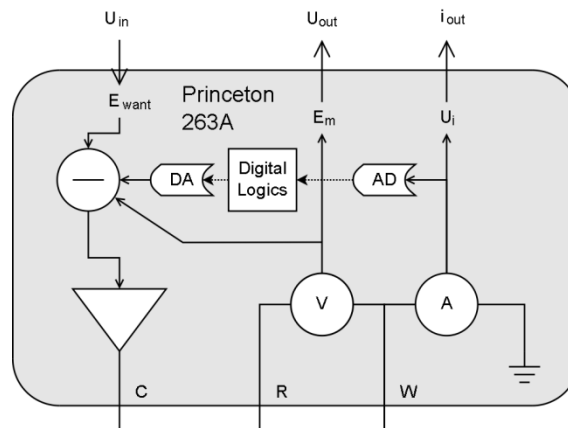
Figure 3.5-6: **Scheme of the control system of the semi digital Princeton 263A potentiostat including the compensation of the solution resistance by a positive feedback scheme [29].**

An additional drawback of the 263A potentiostat is shown in
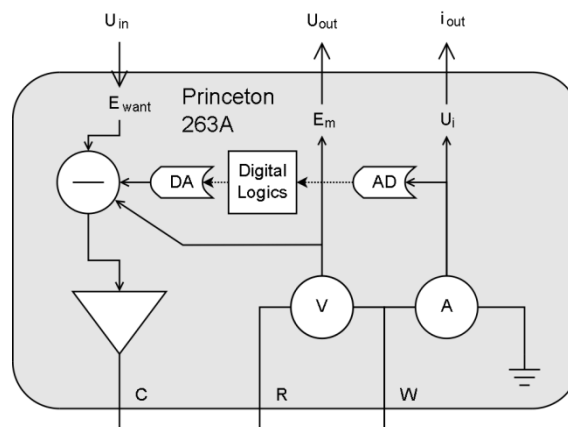
figure 3.5-6, [29]. The compensation scheme used in 263A deviates from the one shown in figure 3.5-4 in the way that U_m is measured instead of the compensated potential E_{comp}. Thus although a compensation scheme is applied to the system, U_{out} is not corrected, thus making it difficult to the user to control the effective compensation. Given the unsatisfactory performance of the two potentiostats, within the framework of the presented thesis an analogue potentiostat was developed which is optimized to our requirements yet flexible in its design to hardware additions.

3.6 In-house designed analogue potentiostat

By constructing our own potentiostat, the design could be optimised for our experimental requirements.

The following requirements were chosen for the in-house designed potentiostat: i) the current supply was limited 10 mA. This value is about a magnitude higher than the typical current in a RDE experiment probing the oxygen reduction reaction (6 mA/cm² on a 0.2 cm² electrode [30]); ii) at the same time the accuracy should be highest in a current range between 10 µA to 10 mA; iii) the current range can be set in remote control by the computer; iv) a positive feedback scheme for the compensation of the solution resistance should be implemented. As discussed in the previous chapter, such a compensation scheme is the most adequate to our requirements as the solution resistance is expected to be constant during the experiment. The scheme is electronically easy to implement and can compensate for the solution resistance even at high frequencies. Hence, its performance can easily be demonstrated and monitored.

3.6.1 Circuit Design

There are numerous examples of potentiostat designs in the literature. Based on the ones given in refs. [13, 31-32], the potentiostat was planned.

The design of many active electrical systems is based on operational amplifiers (OP amp). An op amp is an active component that produces a voltage at the output that is several million times larger than the voltage difference at the two inputs. By connecting different passive electronic components (resistor, capacitor and inductor) to the OP amp, several well defined assemblies can be made, such as: an amplifier with fixed gain, a voltage summing device, etc. These can be used as building blocks in order to achieve a regulating system, such as the one needed in the analogue potentiostat [33-34].

The components have to be carefully chosen, especially the operation amplifiers. The characteristics of non-ideal amplifiers deviate largely from ideal ones. Each model has different specifications in order to cover specific areas of operation. For example, an operational amplifier that can deliver a large current is often relative slow compared to an amplifier that can only deliver small currents.
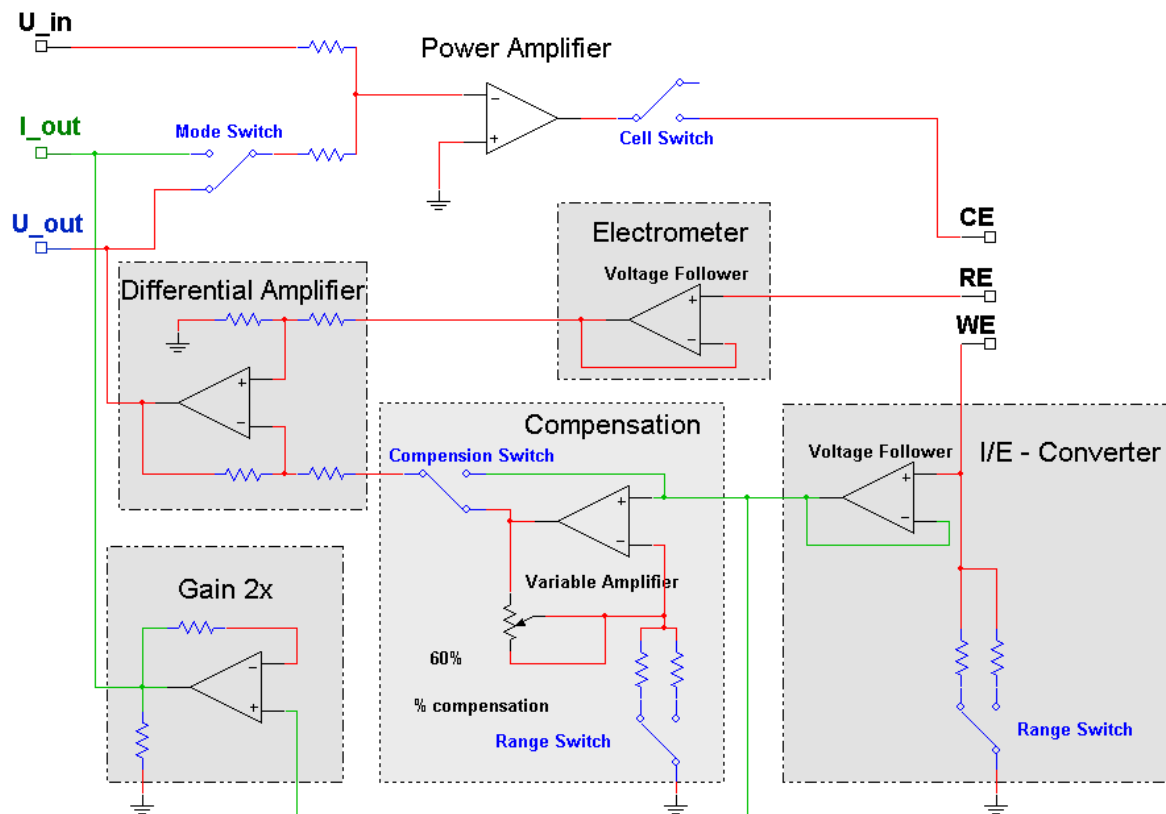
Figure 3.6-1:   Simplified block diagram of the in-house made potentiostat.

The circuit block diagram of the in-house designed potentiostat is shown in figure 3.6-1. The layout corresponds to the one given in figure 3.5-4. The simplified block diagram exhibits the main features of the operation of the potentiostat. Supplementary components, such as the digital control circuitry for the remote switch control has been deliberately excluded. In the following the most important parts are described.

3.6.1.1 Electrometer

The voltage at the reference contact is measured by an electrometer, i.e. a voltage follower. The output is connected to the inverted input (-), hence the output voltage (U_R) is negatively fed back. The op-amp will supply maximum voltage as long as there is a potential difference between the inputs. Because of the negative feedback, the output voltage will dynamically adjust until the voltage at the inverting matches that of the non-inverted input. In other words, the output voltage will follow that of the non-inverted input.

The specific operational amplifier used for this operation has a high input impedance ($>10^{12}$ Ω) such that almost no leak current floats. This is vital for the reference electrode since a current would shift the potential from equilibrium and introduce an offset.

3.6.1.2 Current to voltage converter

In order to measure the current passing through the working electrode, the current has to be converted it into a voltage. Therefore the current is passed through a resistor and it can be calculated following Ohms law. Thus the conversion factor can be chosen freely. As seen in figure 3.6-1, a voltage follower replicates the voltage (U_W) over the resistance. Its high input impedance reduces the current through the secondary path, via the operation amplifier to ground. Otherwise such a secondary path could cause a large deviation.

The ADC, which records the voltage signal, operates in the range [-2,2] volts with 65536 discrete steps (16-bit). In order to minimise the relative measurement error, the current signal has to be conditioned. The maximum reached current/voltage should fit the interval range, while the digital resolution determines the detection limit of small currents. Hence, by switching between different resistances, the current signal can be converted to the optimal voltage value. Four different conversion resistors were chosen: 50 Ω, 500 Ω, 5 kΩ, 50 kΩ. A supplementary amplifier ("Gain 2x") enhances the signal two times. As a result, 1V measured at the output corresponds to a current of 10 mA, 1 mA, 100 µA or 10 µA, respectively, flowing through the WE.

The switching between the resistances is performed by electrical relays (range switches). These relays can either be controlled remotely by computer via the digital channels of the DAQ-card or manually at the front panel of the potentiostat. The known current-to-voltage factor is later used in the program to calculate the value of the current through the WE.

3.6.1.3 Differential Amplifier

A differential amplifier circuit generates a voltage which is proportional to the difference of the voltages at the two inputs. This can be achieved by connecting four resistors of the same size (typically 10 kΩ) to an operation amplifier as shown in figure 3.6-1. In this case the voltage difference of interest is the one between the

reference and the working electrode. Therefore, the two signals from the voltage followers are connected to the amplifier. Thus, independent of the relative ground of the reference or working electrode, the output of the amplifier gives the difference between the two input values.

$$U_{out} = U_R - U_W = E_m \tag{35}$$

3.6.1.4 The solution compensation

In order to compensate for the solution resistance, a voltage proportional to the measured current has to be added to the control loop. In the developed setup, the working electrode is potentially not on ground, but shifted by the voltage over the current measure. Hence if this voltage is fed back not with unity but scaled up, the desired effect is achieved:

$$U_{out} = U_R - (1+\Delta)U_W = E_{comp} \tag{36}$$

where Δ is level of amplification.

The amplification factor of the variable amplifier in figure 3.6-1 linearly increases with the variable resistance. The variable resistor ranges from 0 to 50 kΩ. If the variable resistor is turned to 0 Ω, the amplifier behaves as a current follower, i.e. amplification is 1 (Δ=0).

The amplification factor is furthermore influenced of by the second resistor. In order to avoid that a change in current range influences the compensation, the second resistor has to be changed in accordance to any changes in the current range. For up to 50 Ω compensation, the second resistor is 50 kΩ and 5 kΩ for the current range 10 mA and 1 mA respectively. For the two other current ranges, the potential error would be less than <5 mV if the solution resistance is less than 50 Ω which can be considered negligible.

The compensation of the solution resistance can be disconnected by a switch on front panel which disconnects the output and connects the signal line to ground.

3.6.1.5 Operation Mode and Power Amplifier

The mode switch, see figure 3.6-1, sets the operation mode of the potentiostat. In the potentiostatic mode, U_out is connected to the power amplifier, whereas in the galvanostatic mode, I_out is connected to it.

The power amplifier is an OP amp that can deliver both a high voltage as well as a large current. The amplifier supplies the voltage needed to force a current through the cell until the voltage at the two inputs of the amplifier matches. Hence in potentiostatic mode, the negation of U_in corresponds to the generated voltage of between RE and WE. In the second case, the current applied to the cell corresponds to a fraction of the current range given by the negation of U_in.

3.6.2 Front Panel
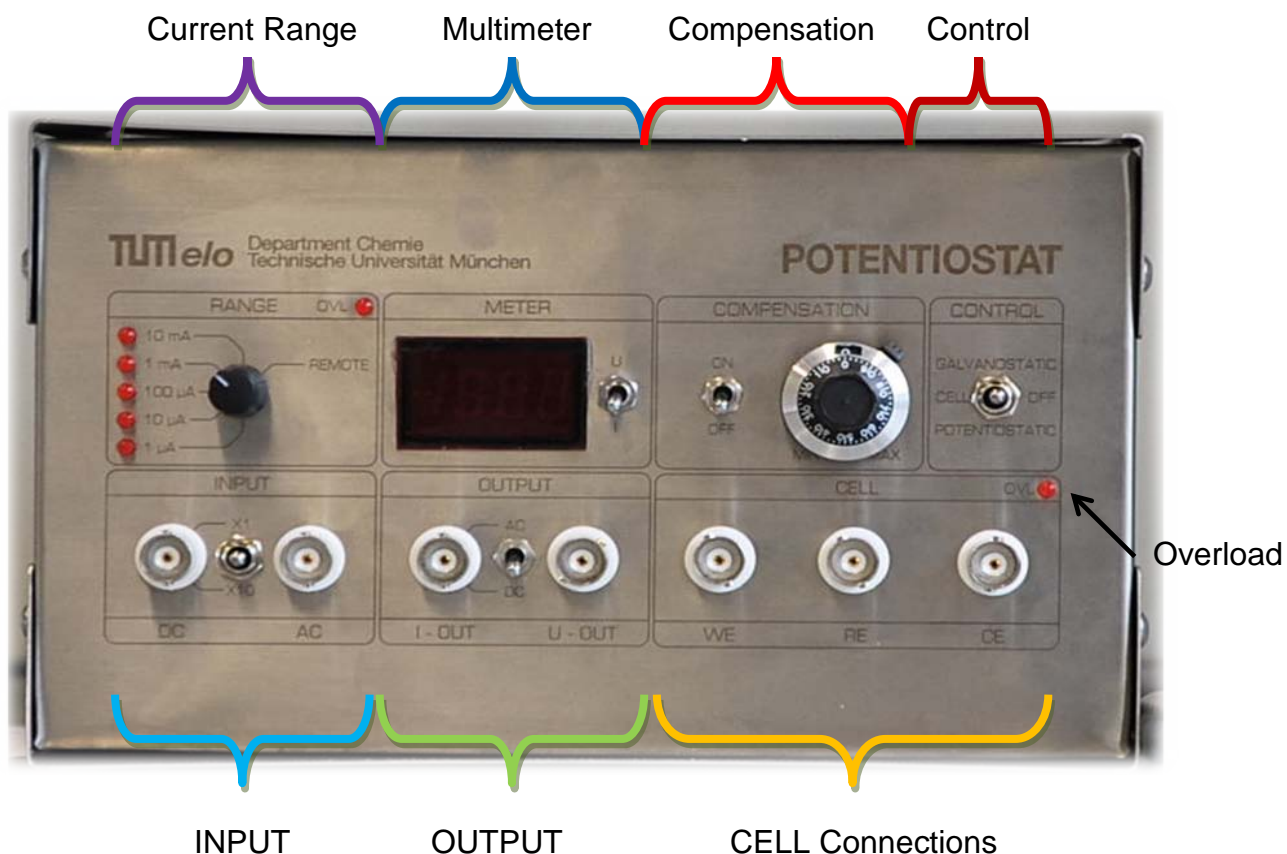
Figure 3.6-2: **Picture of the front panel of the in-house made potentiostat**

The front panel of the in-house designed and manufactured Potentiostat is shown in figure 3.6-2.

The upper part of the front panel features the manual settings. The current range can either be set manually or remotely by turning the black knob to the appropriate position. In either case a small light indicates to the user which current range is currently active. The Multimeter display shows either the voltage between the WE and RE contact or the current trough the WE (expressed as voltage). The solution

resistance compensation can be switched on or off. Its value is set via the potentiometer. The maximum compensation (10-turns) corresponds to 50Ω. The 3-position control switch sets the operation mode of the potentiostat and activates the connection to the electrochemical cell. In the upper position, the potentiostat operates in galvanostatic in the lower position in potentiostatic mode. In the middle position the electrochemical cell is not electrically connected. This switch is over ridden if the current range knob is set to REMOTE.

At the lower part of the front panel the electrical connections to the electrochemical cell, the INPUT and the OUTPUT signals are found. BNC connectors are used in order to shield the signals from electrical noise. There are two connectors available for the signal INPUT, of which one is DC coupled and the other one AC coupled. At the OUTPUT connectors, the voltage between RE and WE as well as the current signal can be measured. The current output can be AC coupled in order to increase the sensitivity of AC signal.

On the front panel there are two LEDs indicating an overload. The LED at the CE connection indicates a voltage overload, whereas the second LED indicates a current overload, i.e. if the range of the I/E converter is exceeded.

3.7 Multi-Working Electrode system

As discussed in the previous chapter, with the invention of high surface area catalysts for low temperature fuel cells a new type of surface to volume optimized catalysts was introduced. The properties of such a catalyst are more complex in comparison to a flat electrode. The active surface area does not correspond to the geometric area, but is rather proportional to the applied amount of catalyst mass and the particle size. Hence, in order to be able to compare the catalytic activities, i.e. the normalized reaction rates of different catalysts, the electrochemical surface area or number of electrochemical active sites has to be determined [35]. In addition, there are also more practical issues concerning the samples. At high loadings not the complete catalysts might be accessible for the reactions anymore. Furthermore, part of the catalyst can be lost upon introducing the working electrode into the solution, but also due to the preparation method. All these factors result in errors for the activity determination. Therefore, the characterization of a significant amount of

samples is required in order to achieve statistically significant results. This can be very time consuming.

3.7.1 Add-On Modular MWE device

In order to reduce the time needed for characterizing a catalyst, the measurements can be conducted in parallel. Multi channel potentiostats featuring a simultaneous individual potential control and current measurement of each electrode are commercially available [36-37]. This permits to conduct different measurement protocols to be synchronously applied to different WEs. As a result of their complex circuit architecture however, multi channel potentiostats are in general expensive, which has impeded their wide spread use. However, if the same measurement protocol is employed, an individual potential control is not necessary, and hence a more basic circuit architecture can be used. As part of the presented thesis a modular add-on device was designed and built, which allowed to use the existing instrumentation for multi-channel measurements.

The outline of the standard EC setup (see figure 3.5-5) with the additional MWE modular system can be seen in figure 3.7-1. The MWE module is added between the working electrode contact of the Potentiostat and the working electrode(s).
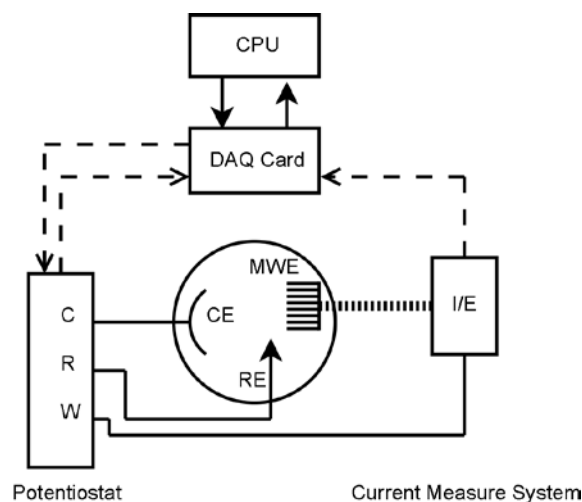
Figure 3.7-1:   Outline of the setup for electrochemical measurements using several working electrodes. In addition to the normal setup (see figure 3.5-5) there is a modular multi-channel I/E converter in between the working electrodes and working electrode connector of the potentiostat.

The operation principle of the active device is to convert the current of each channel into a voltage. Simultaneously, it actively strives to minimise the potential drop between each electrode of the MWE assembly and the input potential of the WE contact independent of the current floating through the electrode contacts. Thus the control circuit of the potential is not affected by the module and the potential at the working electrodes is still controlled by the potentiostat. In the following the design considerations of the add-on modular MWE device and its realization are described in more detail.

3.7.2 Circuit design

In order to realise the MWE system, a circuit design is required that permits an accurate current measurement at an electrode without the addition of a potential drop. This is achieved by an active current-to-voltage converter: a so called trans-resistance amplifier.
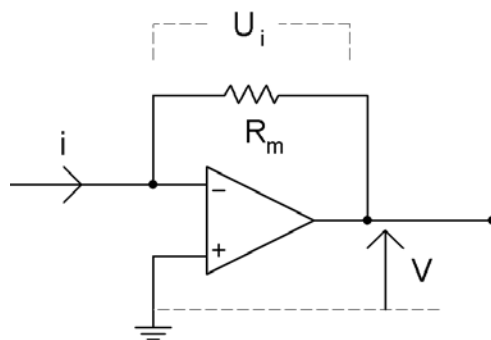
Figure 3.7-2:   **The outline of a trans-resistance amplifier. The current is converted into a voltage by the active element.**

A trans-resistance amplifier, a circuit layout is shown in figure 3.7-2, consists of an operation amplifier and a resistance (R_m). The resistor connects is connected between the output and the inverting input (-), hence the output voltage (V) is negatively fed back. The op-amp will supply maximum voltage as long as there is a potential difference between the inputs. Due to the negative feedback, the output voltage will dynamically adjust until the voltage at the inverting matches that of the non-inverting input. There is only one current path for i, hence in order to keep the voltage of the inputs equal the operation amplifier drives the same current in the opposite direction. As the potential difference at the inputs is virtually 0, the potential

at the output obtains the same value as potential drop over the resistor (U_i). By measuring V relative ground the current can be calculated given Ohm's law.
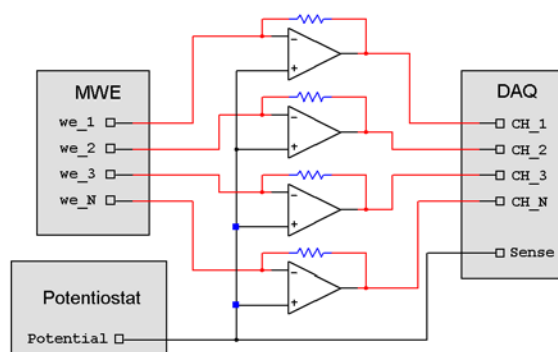
Figure 3.7-3: **Simplified block diagram of the MWE module. The module consists of several trans-resistance amplifiers in parallel, one for each working electrode.**

Several parallel trans-resistance amplifiers, one for each current channel, constitute the add-on MWE module. The block diagram is shown in figure 3.7-3. In contrast to the trans-resistance amplifier in figure 3.7-2, the non-inverted inputs of the amplifiers are not connected to ground but to the working electrode connector of the potentiostat. The working electrode connector of a potentiostat is in general not on ground. Therefore, in order to measure the voltage of the outputs correctly, the DAQ card has to be measured via the sense connection which is connected to all the non-inverted inputs as well as the working electrode connector.

The circuit design is scalable and there is no theoretical limitation of the number of working electrodes that can be used at the same time. However there are limitations due to the power output of the potentiostat.

3.7.2.1 Realization

The MWE module designed and built is shown in figure 3.7-4 together with the MWE shaft and the connection to the DAQ card. Considering the physical size of the MWE assembly, the system features only 8 channels (see chapter "Developed multi working electrode (MWE) array"). The device has a fixed current range of 1 mA, corresponding to the maximum expected current during the measurement of the oxygen reduction reaction. The current is measured over 1 kOhm resistors, thus a current of 1 mA corresponds to 1 V.

The circuit board, on which the operational amplifiers are positioned, is encased in a metal box for shielding electrical noise (figure 3.7-4). Only standard components are used in order to achieve a dynamic range of about 50 kHz. Each OP amplifier can handle currents up to at least 5 mA without saturation.
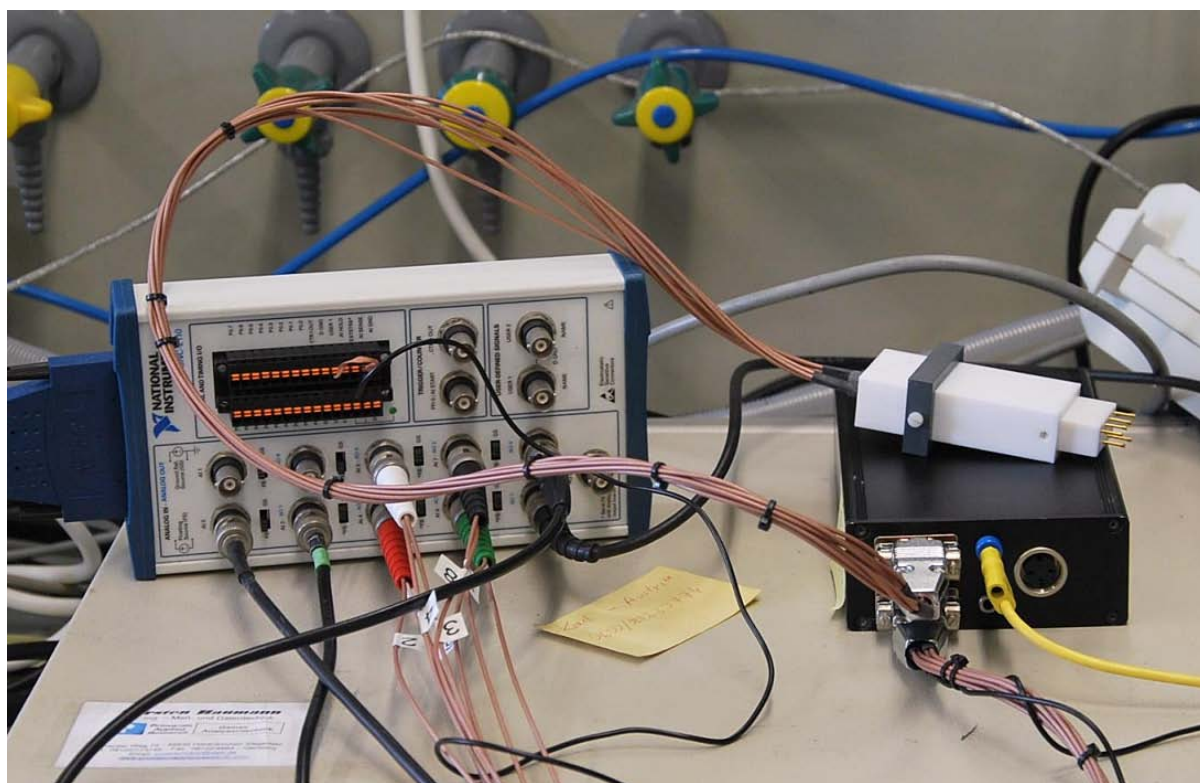
Figure 3.7-4: **Picture of the MWE device, MWE shaft and DAQ connection board**

On the front side of the module, there are two 9-pin D-sub (DE-9) connectors; one male, to be connected to the array of working electrodes, and one female, to be connected to the DAQ. The pin numbering of the connectors corresponds to the matching channel except for Pin 9. On the female contact this pin is connected to the non-inverted inputs of all operational amplifiers hence it should be connected to the WE channel of the potentiostat and the sense channel of the DAC card. On the male contact the 9th pin is connected to ground, to which the outer parts of the coaxial cables connecting the MWE module to the shaft are contacted. Additionally, there are two banana sockets for the current return feed to the potentiostat and the ground.

The DAQ card is set to measure the current channels in a Single-Ended-Non-Referenced (NRSE) mode. Each channel is therefore measured with respect to a

common reference (sense); in contrast to the Single-Ended-Ground-Referenced (GRSE) mode where the signals are measure relative to ground. The NRSE mode is also practical for other reasons. Ground loops which can induce electrical noise can be avoided, as the ground of the DAQ is not connected to the MWE device [38].

During normal operation, ideally no current should float between the MWE device and the potentiostat through the WE cable. However due to leak currents from the non-ideal OP amplifiers a current of a few µA will float. In the case when an excessive current is forced through the device, the amplifiers will fail to work properly and a much larger current will float. In order to identify such an event, during a measurement the current channel of the potentiostat is recorded and monitored in addition to the current channels of the MWE device (See section "4.2.1.1 CV program").

3.7.3 Proof of functionality

In order to demonstrate the function of the device, an electrochemical setup was assembled connecting the device to the Princeton 263A potentiostat. A MWE tip was prepared with 8 samples of equal amount of carbon supported platinum catalyst and the resulting CVs measured in 0.1M $HClO_4$ solution are plotted in figure 3.7-5.
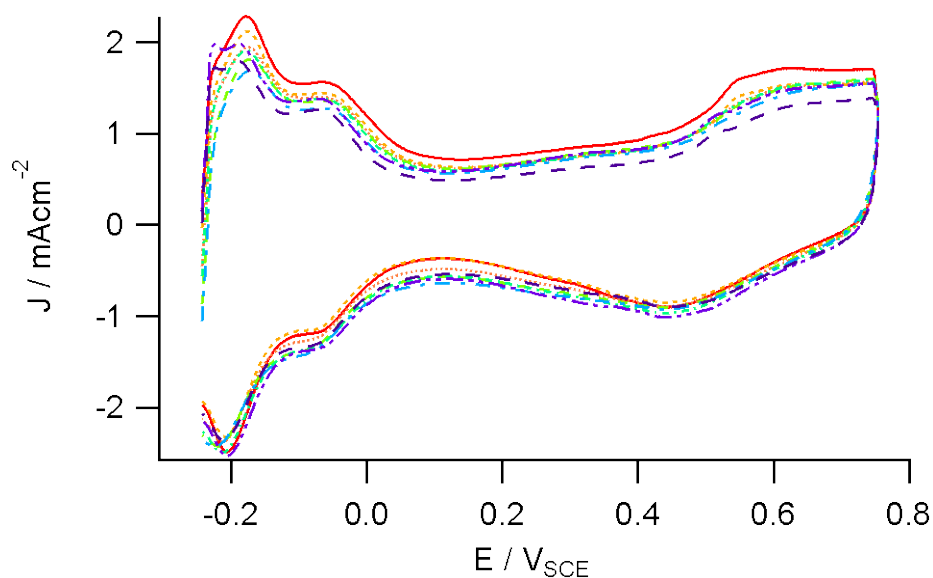
Figure 3.7-5: **Proof of the functionality of the MWE device. Simultaneously recorded CVs of 8 different samples of the same carbon supported platinum HSA catalyst. The scan rate was 200mVs^{-1}, the electrolyte argon saturated 0.1 M $HClO_4$ solution.**

The current response from the 8 simultaneously recorded channels shows almost identical features of same magnitude. The CVs correspond well to the one obtained in a single electrode setup [39]. The small deviations between the CVs are mainly due to the different solution/contact resistances of each channel. The ECA or roughness factor (R_f) of Pt based HSA catalysts can be determined by integration of the hydrogen adsorption/desorption current features or the charge from oxidizing a saturated CO monolayer (CO stripping measurements). In table 3.7-1 the accuracy of the R_f determination by 5 individual RDE measurements is compared to 2 MWE measurements. It is apparent that especially when using CO stripping measurements the standard deviation of the values can be greatly reduced by the MWE. In only two measurements the standard deviation of 16 individual values is as low as 5.1%. As the surface area of a catalyst directly affects the calculated specific activity, the MWE therefore reduces the statistical error in catalytic investigations.

	R_f H_{UPD}	σ	R_f CO stripping	σ
RDE	8.0	40.0 %	8.4	38.1 %
MWE	8.6	36.0 %	7.8	5.1 %

Table 3.7-1: **Comparison of the averaged roughness factors R_f and standard deviation σ of a Pt/C catalyst determined by RDE and MWE measurements. The R_f values were calculated from H_{UPD} and CO stripping measurements. The RDE values were determined from 5 individual measurements, the MWE values from 2 individual measurements equalling 16 values.**

3.7.4 Future Improvements

In its current status the MWE measure system has some limitations compared to a single electrode setup. Due to the simple circuitry, only one current range exists. In general this is no disadvantage because the setup is designed for a specific application with little variation in the currents to be measured. A more critical disadvantage is the lack of an electronic IR-compensation, which requires a good cell

design with low solution resistance. Furthermore, a relative powerful potentiostat is required which can supply the current/voltage to drive the experiment circuitry.

In the following some design improvements are discussed which could alleviate the mentioned short comings of the current setup.

3.7.4.1 Negative impedance converter device

In order to enable an IR compensation of the solution resistance, a negative impedance converter device (NID) could be used. Not only is the voltage corrected, but the device can simultaneously be used as an I-V-converter, hence the trans-resistance amplifier could be replaced by NIDs.
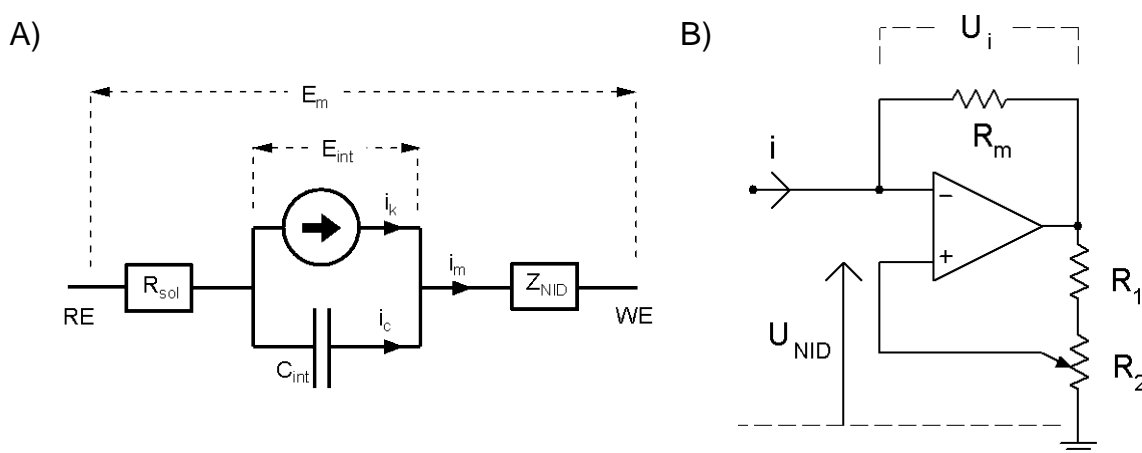
Figure 3.7-6: **The half cell model including the negative impedance converter device (A). The NID introduce a voltage drop which equals out the potential drop over the solution resistance. B) The schematics of the device.**

As shown in figure 3.7-6, the NID is similar device as a trans-resistance amplifier (figure 3.7-2). However, at the NID two extra resistors are added: one between the amplifier output and the non-inverted input and the other one between non-inverted input and ground. The current can be measured as the potential over the resistance R_m. The two additional resistors create an offset to the working electrode corresponding to the size of the resistors and the current:

$$U_{NID} = -i_m \frac{R_m R_2}{R_1} \tag{37}$$

where U_{NID} is the compensation voltage, and the R_m, R_1, R_2 resistors shown in figure 3.7-6(B). The impedance of the device is given by:

$$Z_{NID} = -\frac{R_m R_2}{R_1} \qquad (38)$$

The value of the impedance is always below 0, thus the name of the device.

The NID can be implemented to the circuit of the half-cell model, shown in figure 3.7-6(A). As both the solution resistance and the NID impedance are in series, an effective solution resistance (R_{eff}) is defined by:

$$R_{eff} = R_{sol} + Z_{NID} \qquad (39)$$

If the resistances are correctly chosen, the effective solution resistance is minimized. As prior to an experiment the effective solution resistance is not known R_2 has to be a variable resistor. Applying a high frequency AC signal to the system R_{eff} can be determined.

A drawback of the NID, however, is that the working electrode is no longer at the virtual ground. As a consequence the voltage difference between the amplifier output and ground does not correspond to the voltage drop over the resistor. Hence, in order to acquire the current, the voltage over the resistor must be measured differentially. This increases the complexity of the measure system as well as its price.

3.7.4.2 Extra amplifier stage

In order to enable to use of the MWE module with a low-power potentiostat, an additional amplifier can be added to the circuit board. The amplifier boosts the incoming CE signal from the Potentiostat and enlarges its power range.
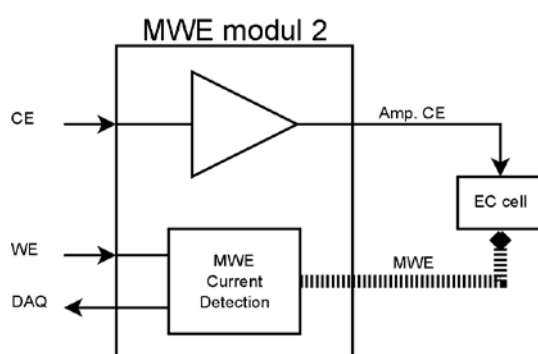
Figure 3.7-7: **Outline of an improved MWE module; an addition amplifier has been added in order to give the measure system an enhanced**

power range. Thereby can the module also be used by low power potentiostats.

4 Software development

In the following chapter the software programs which were written as part of this thesis are described. The first part of the chapter deals with general details and concepts of software programming. The second part describes the data acquiring applications developed to control the electrochemical setup in detail. The third part deals with the data analysis application created to facilitate the data treatment.

4.1 General

4.1.1 Motivation

In order to control potentiostats in electrochemical measurements software programs are commercially available. The programs are in general developed to work with a specific potentiostat and a limited amount of additional hardware. Hence, such programs are not ideal for our purposes due to the lack of support for the specific instruments used in our setup.

In order to use all the advantages of computerized control of the experimental setup, it was necessary to develop our own software, both for the data acquisition application as well as the data treatment.

Performing the experiments under full computer control is advantageous. Not only can different potential perturbation techniques easily be used, but it also enables the control over other experimental parameters such as convection, temperature, gas purging, etc. Additionally, the computer control permits the execution standardized measure protocols considerably enhancing the reproducibility of experiments. In such case, the experimentalist only needs to setup the experiment and click on start.

Another advantage is that all parameters can automatically be saved into the data file. As experimental parameters have a great impact on the measured current, this simplifies both data management and the data treatment.

In order to write the code to our programs, it was necessary to choose the most suitable programming language with respect to both learning curve and development time of the program. In the following first the considerations for the chosen programming language are discussed and then the developed software is introduced in detail.

4.1.2 Programming language

A programming language is an artificial language that is designed to express computations that a machine can perform. Numerous languages have been developed targeting different programming aspects. These are spread out on the ladder of abstraction. The low level languages work close to how the physical processor is working, which permit the programmer a close control of memory and processor usage. Examples of such languages are C, C++, and Assembler. On the other hand, high level languages use a higher level of abstraction. The detailed control of memory processor is automatically handled, which let the programmer focus on the main tasks of the program. This simplifies the writing of larger and more complex programs [40].

A)

```
int x,y;
boolean k;
x=5+8;
y=x*2;
k= (x==y);
```

B)
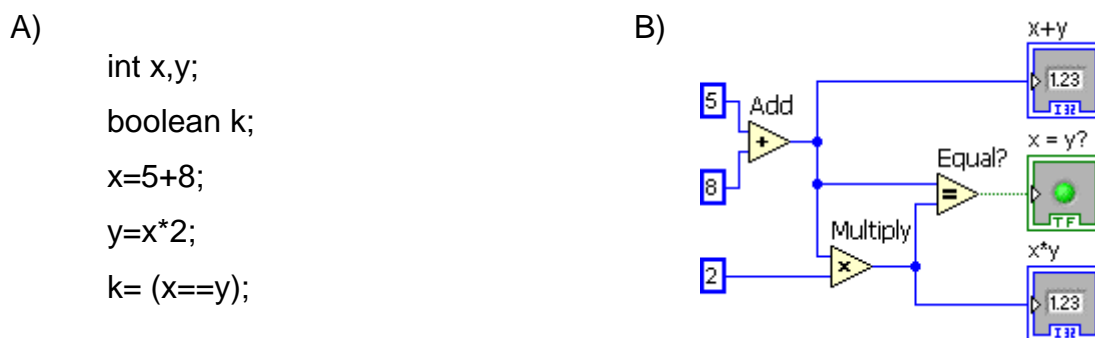
Figure 4.1-1:   Comparison of program syntax: text based program (A) and visual based program (B).

Most languages are based on a text syntax which is more easily "translated" to machine instructions. An example of the text syntax is shown in figure 4.1-1. However, in the last decade visual program languages, i.e. diagrammatic programming, have become more popular. They let the user create programs by manipulate program elements, in contrast to text based program. As shown by the example in figure 4.1-1, this kind of programming is more intuitive and easier to learn also for non-programmers. The greatest advantage is that it facilitates to have a better overview over large and complex programs and the dataflow between different parts [40-41]. This becomes more important in modern programming as it is easy to implement process parallelism, an important feature to optimise the processor usage. Visual programming is also widely believed to increase productivity and thereby reduce development time and cost [42].

LabVIEW from National Instruments; the programming language chosen in this work, is a visual program language that is especially developed for the data acquisition, instrumental control and industrial automation [43]. The language is however not limited to only these aspects but can with favour be used in more general purpose programs such as an interactive tool to learn chemistry and physics [44-46]. Examples of electrochemical experiments controlled by LabVIEW can also be found in the literature [47].

4.1.3 General aspects of the programming

Programming is all about organising simple instructions into complex patterns, and by that, manipulating the computer to perform specific tasks. These instructions are organized in tasks which are subsequently organized in processes. In general, a program consists of a set of instructions that the processor should perform.

In order to build a sophisticated program one has to decide upon a strategy how to organise the processes and in which order they should be executed. Taking the DAQ application as an example, the program can be divided into 3 different processes such as "write", "read" and "treat". While the write process invokes a perturbation of the measure system, the read process records the data. The treat process applies mathematically treatment to the data in order to reduce the large amount of data to less but more characteristic values, which are display value to the user. In order to create such a program, two possible schemes can be used; sequential and parallel. These are shown in figure 4.1-2.
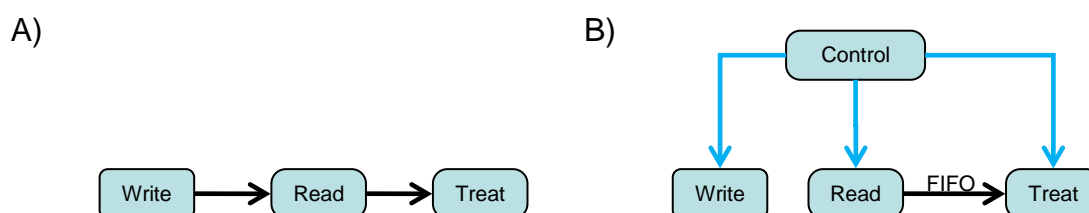
Figure 4.1-2: Illustration of two different execution schemes of processes. In sequential exaction each process must terminate before the subsequent (A). Data which the subsequent process requires is only available at the end of an execution process. In parallel execution, the processes run simultaneously (B). Data flows between the processes are created by FIFO queue systems.

In the sequential strategy, the processes are executed one after another. As soon as one has finished, data can be sent to the following one. As all the instructions have been executed, the program is done, just like a basic calculator. This strategy is very easy to implement, but has the limitation that it cannot be run continuously.

More advanced programs tend to be build based on a parallel scheme. Although more complex, in the case of larger programs the benefits are predominant. Using the example with the DAQ application, the user wants to both continuously measure and in real-time observe the resulting values. This would not be possible in a sequential strategy.

A parallel process scheme can use the processor more optimised. The development of the computer has come to a limit where the processor cycle frequency cannot be increased further because of physical limitations. The processor architecture improvements have therefore turned toward enabling the processor to perform more computations in parallel and thereby increasing its performance [48].

Although the program has a parallel structure the different processes are not necessarily executed in parallel. The operation system of the computer organises the computational tasks into threads, where each program gets one thread per default. As the execution program sends "small packages" of computation task to the processor, the execution is not truly parallel. In order to take full advantage of the processor, the sub processes of the program must be executed in different threads.

A primary challenge of the parallel scheme, which is not present in the sequential scheme, is how to ensure a real time data flow from "Read" to "Treat". As these processes never stop, the data transfer has to be realized over a shared buffer space in the memory. In programming, such a space is called a shared variable, where one process can write to the memory and another read. Such a system is often limited to only one variable. A more advanced form is a First-In-First-Out (FIFO) queue system. One process becomes the producer and writes to the memory space, while another process becomes the consumer and upon reading liberates the used space. Using a queue enables the processes to run desynchronised. As an effect, the size of the queue can change during the time depending on which process runs the fastest. This is a major advantage because non-time critical processes can be set in a way that they are executed when the processor has free capacity which ensures that the time critical processes always have access to the processor.

A major issue when creating parallel processes is the abortion of their execution, especially if an error occurs or if there is no known abort criteria prior to execution. This can be solved by introducing a control process as shown figure 4.1-2. Such a process, one can also be used to abort processes in a certain order.
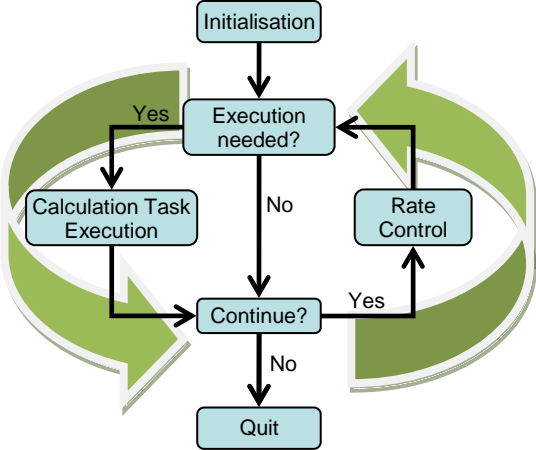
Figure 4.1-3:   **Outline of the general parallel process scheme. The iteration is rated limited in order to economise calculation power of the CPU.**

The outline of the control implementation on a single process level is shown explicitly in figure 4.1-3, which illustrates the outlines of a general continuously executed process. As can be seen the process is built around a loop of four tasks performed in sequence. Firstly, the necessity of an execution of the calculation task is controlled or in other words, the FIFO queue is queried as to whether it contains any data elements. If that is the case a computational task is performed, such as averaging or Fast Fourier Transform (FFT) calculation. Else, the task is bypassed. Subsequently, in the third task, the control process is queried, and the iteration can be stopped. In the fourth task, the iteration rate is limited. On the one hand, a rate limitation reduces the calculation burden of the processor so it can perform other more time critical tasks. On the other hand, having the process iterating very slowly makes the latency between quitting commanded by the user or another process and the abortion of the process to be elongated.

4.2 Developed data acquisition applications

4.2.1 Applications

In order to control the experimental setup by computer, several data acquisition applications were developed in this thesis. Each with respect to the specific electrochemical technique used. The programs were developed in such a way that all the different models of potentiostats to our disposal were compatible to it.

In addition the programs were developed in order to permit the identification of inconsistencies and failure of the potentiostatic control system. Thereby the occurrence of experimental artefacts can be minimised.

4.2.1.1 CV program

The CV program was developed in order to perform cyclic and AC voltammetry, as the latter is a superposition of the cyclic voltammetry and a sinus perturbation. The program exists in two versions: one for single electrode and one for MWE measurements. Screenshots of their front panels are shown in figure 4.2-1 and in figure 4.2-2.

The software program is also a tool to analyse the setup and a help to diagnose any physical shortcomings of the setup. A Fast Fourier transform can be applied to the measured signal in order to elucidate the amplitudes of different frequencies. It also features online monitoring of the solution resistance.

Upon launching the program, the program detects which experimental accessories are connected to the computer. Furthermore, communication with the preconfigured potentiostat is initialised based on the saved settings (see section "Configure Panel").
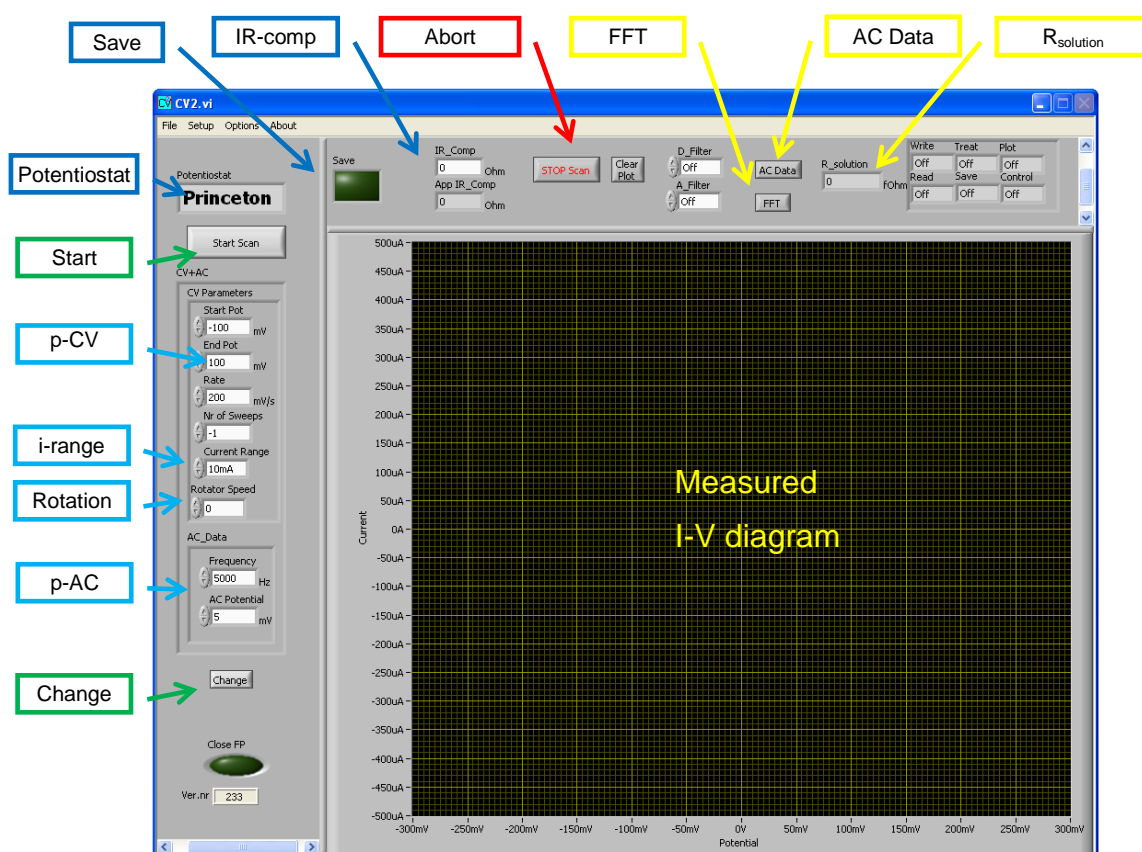
Figure 4.2-1: **Screenshot of front panel of the CV program - single electrode**

The front panel of the CV program consists of three areas. On left most, the experimental parameters can be set such as the start and end potentials as well as scan rate of the CV [p-CV]. In addition a superimposed AC signal of arbitrary frequency and amplitude can be added [p-AC]. While these parameters are only active once the experiment is launched, an adjustment to the rotation rate of the RDE [rotation] and current range of the potentiostat [i-range] are directly executed. The experiment is launched upon clicking onto the start button. In the middle area, the measured data are displayed in an I-V-diagram. Only the three last recorded voltammograms are displayed. In the upper most area, supplementary options are given to the user. Particular voltammograms can be saved by highlighting the SAVE button. The execution of the experiment can be halted [abort]. During the measurement, by clicking on [FFT], a pop up window opens displaying a log-log-diagram of the current and the voltage amplitude versus frequency. The effective solution resistance is monitored in-situ during the measurement in the indicator

[R$_{solution}$]. If the semi-digital Potentiostat Princeton 263A is used, a solution resistance compensation can be applied by adding a resistance value to [IR Comp] (in case of the home-built potentiostats this item is only manually available). By click on [AC Data], a diagram with the impedance and phase versus DC voltage is shown.

Upon the launching the experiment by clicking on start, a popup panel is launched where specific experimental constants can be defined (see Setup Panel). Upon closing, the measurement is carried out and the current and voltage is displayed in the I-V diagram. The experimental parameters can be changed at any time, however, are only applied at the end of a cycle. When the experiment is aborted, a the pop up dialog asks where to save the files (See "Data File" section). Each file corresponds to one cycle.

The information displayed in the FFT-window can be used as an indicator of the system stability. Electrical noise gets picked up and is amplified by the control circuitry of the potentiostat. Ideally, the amplitudes of any frequency should be as small as possible, excluding any applied perturbation signals. If getting too large, noise can jeopardise the potential controlling stability and cause harm to the working electrode.

For the online monitoring of the effective solution resistance an AC-signal of 5 kHz and 5 mV is applied. In the case of the home-built potentiostat the level of solution resistance compensation can easily be adjusted manually. Note that at low values of the effective solution resistance ~2 Ω, the measurement system can become instable because of electrical noise problems. A post correction of the data might therefore be necessary.
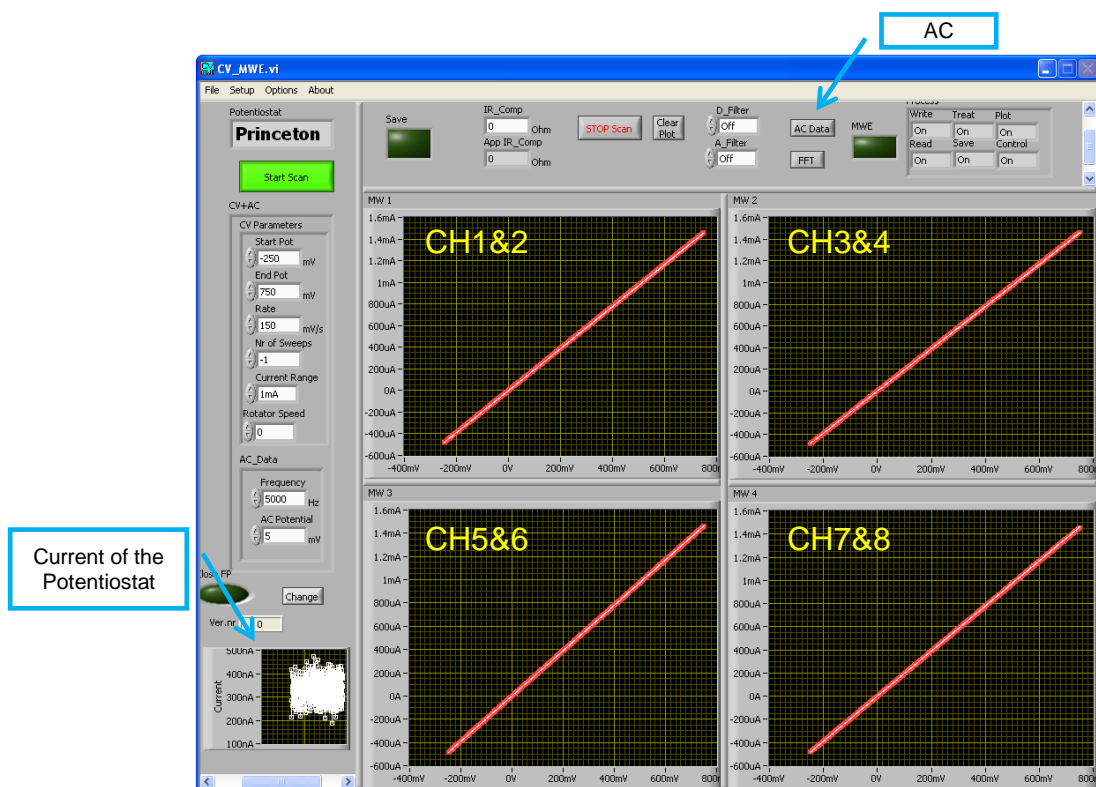
Figure 4.2-2: Screenshot of the front panel of the CV application – multi working electrodes.

The front panel of the CV program dedicated to the MWE setup is shown in figure 4.2-2. This program is almost identical to the single electrode program, except that instead of only one current channel, an additional 8 current channels are measured simultaneously as well. Thus the i-v-diagram is splitted into 4 windows showing two channels each.

The current measured by the potentiostat is shown in the lower left corner. Ideally, this current should be 0 µA, however due to leak currents from the operation amplifiers, an absolute current between 0 and 2 µA is typically measured. In case the MWE box is not able to control the potential of the multi-working electrodes as a result of large currents floating through the device; a large current >>10 µA, will also be measured by the potentiostat and is displayed in the window.

Analogue to the previous case, the solution resistance of each electrode can be measured online if an AC signal is applied. A panel where these values are displayed is launched by clicking on "AC". This feature helps to control that all working electrodes have good electrical contact and low solution resistance. Furthermore, as

the MWE device cannot perform a solution resistance compensation, the resistance values are saved in the measurement file for subsequent correction.

4.2.1.2 DC program

The DC program is used to perform chronoamperometric and chronovoltammometric measurements. The measure current and voltage response upon the perturbation can be monitored on different time scales depending on if transients or the steady state condition is of interest. An AC signal can be added as well similar to the CV program.
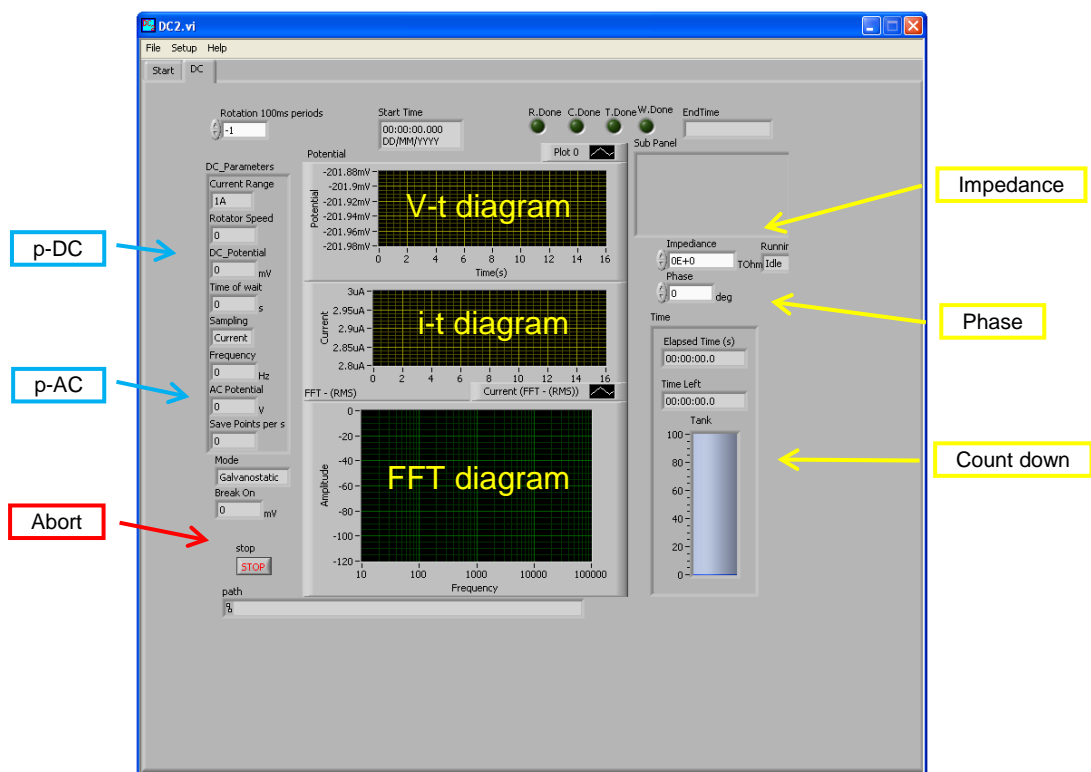
Figure 4.2-3:   Screenshot of the front panel of the DC program

A screen shot of the front panel of the DC program is shown in Figure 4.2-3. As the CV program, it is divided into three areas. On the left sided the technique specific parameters, i.e. the duration and potential, are set in addition to the rotation rate and current range of the potentiostat (p-DC). In the middle part the i-t- and V-t-diagrams of the measured data are displayed together with the FFT in a log-log amplitude-frequency diagram. On the right hand site, the impedance amplitude and the phase

are displayed for the same frequency as the applied signal. A count-down timer is also added for convenience.

Once the measurement is started, reading of the AI channels is launched exactly 100ms before the AO channel is updated. This simplifies the subsequent data treatment as the potential and current level prior to the step is recorded as well and can later be used as a reference.

The user can select how many data points should be saved per second. The maximum number is limited by the ADC sampling rate (see Configure Panel). However, in order to follow current transients resulting from potential steps, a high time resolution is only beneficial on a short time scale. For this reason a dynamic saving mode can be selected. In that mode, 10 points are saved per decade of time up to 30s, after which 1 point is saved per second.

4.2.1.3 Macro Application

A macro application was developed in order to execute a measurement protocol using either a single working electrode or a MWE. The use of measurement protocols is especially useful when performing a sequence of measurements where one or several experimental variables are investigated. This program is best used after previously having controlled the setup and state of the electrode by the CV program.

The program has a build-in protocol editor, which permits the user to quickly create a sequence. Electrochemical techniques that can be applied by the program are:

- CV + AC
- Chronoamperometry (Constant voltage) + AC
- Chronovoltammetry (Constant current) + AC
- SWV and SW
- EIS

In addition, the following variables can be changed:

- Purge gas
- Temperature (heating plate temperature)
- Convection (RDE rotation, stirrer rotation syringe pump)
- IR compensation
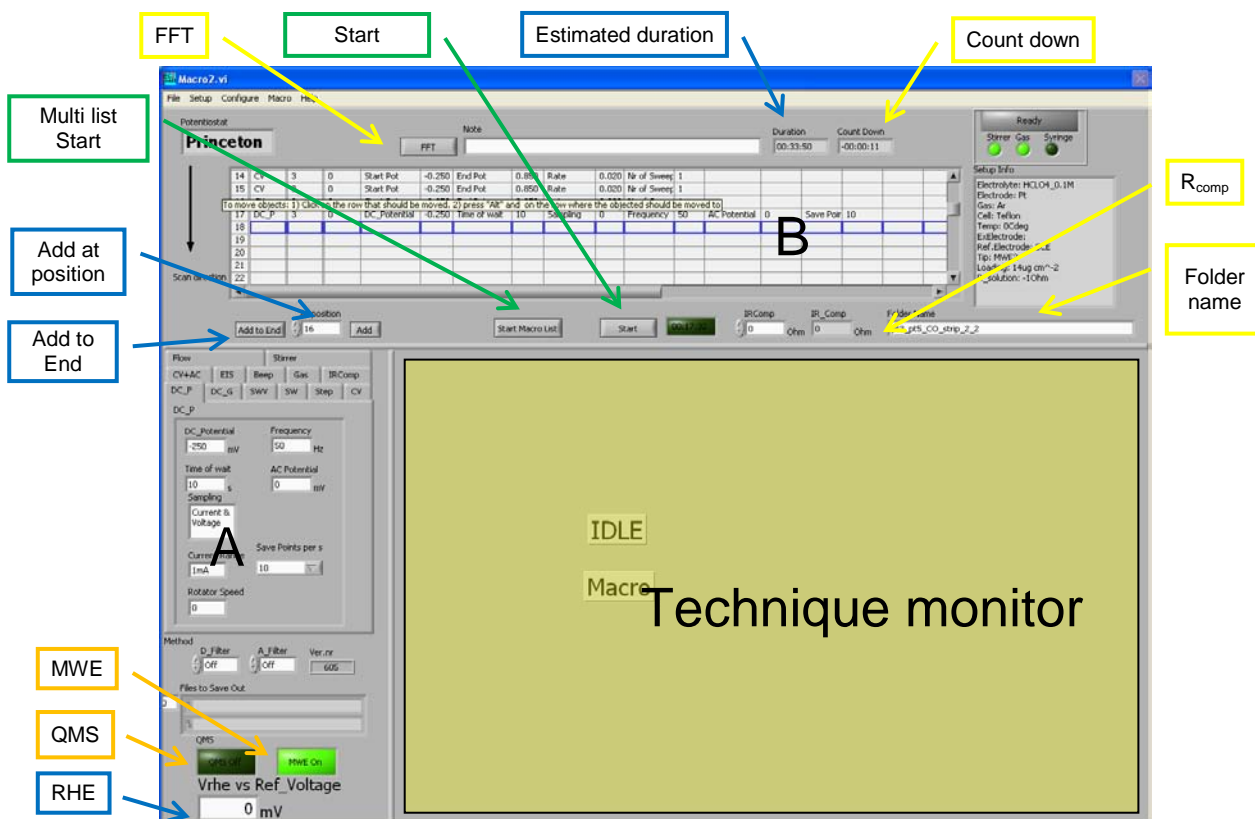
Figure 4.2-4:   Screenshot of the front panel of the Macro application

A screenshot of the graphical window is shown in figure 4.2-4, where the important objects for the operation have been highlighted. The main panel is divided into three areas. The upper area contains a text table (B), where each row corresponds to a technique with all the necessary parameters, i.e. the protocol list. The estimated duration of a protocol is automatically calculated [Estimated duration]. The left part contains a tabbed window (A). Each EC technique or setup adjustment is assigned to a corresponding tab. This window is used to create protocols. Furthermore, the protocols can be expressed with respect to the RHE. By defining the RHE value [RHE] with respect to the reference electrode used in the experiment, the applied voltages are equally shifted. Additionally, the MWE can here be selected as well [MWE].

In the main part [Technique monitor], the front panels of the different techniques will be shown during the list execution.

Prior to launching an experiment sequence, a measurement protocol has to be defined. This can be done either by loading of a pre-made list or by the editor. In order to create a protocol, the user selects a technique in the tabbed window (A) and

defines the parameters. Upon clicking on "Add" or "Add to end", a row is added to the protocol list (B) at the corresponding position. The user can at any time edit the list and change the values, even during the execution of the macro. The duration of the protocol is automatically estimated, in order to keep control of the overall duration of conducting the experiment. At any time, the list can explicitly be saved.

A list is executed by clicking on [start]. The same setup window, as in the previous described programs, pops up and the user can define experimental constants (see Setup Panel). Once closed, a count-down timer [count down] starts based on the estimated duration of the protocol time.

Upon completion, these files are copied to a new folder, which name is defined in the field [Folder Name]. However, if not defined or if the name of an existing folder has been given, the popup window will ask the user for a new folder name (see Data File). In order to reduce the amount of unimportant files, only the last cycle of a CV sequence is saved, independently how many cycles were performed. Additionally, a measure protocol list is generated describing the actual performed techniques and is saved along with the data files.

The program can also execute a succession of predefined measurement protocols. By clicking on the button [Multi list start], a new windows opens. Per new protocol entry, a directory name and path to the saved protocol have to be given. By adding a path, the name of each protocol list is automatically used as directory name, if no other name is given. Being able to perform a series of protocol is especially useful in order to save the measurement files into different folders. This is beneficial when comparing different catalyst under the same conditions.

4.2.1.4 Shared Panels

All applications share two common panels: Configuration and Setup. The panels are used to define the measurement system and the experimental constants, respectively. This information is saved along with the measured data in the save files, which is beneficial for the post treatment of the data as all important experimental parameters are digitally saved. Thus these data do not have to be written into the laboratory book.

Configure Panel

A screenshot of the configuration panel can be seen in figure 4.2-5. The panel consist of two tabs. In the first one, "general", the paths to the directory for temporary data files and the regular data are defined. Additionally, the potentiostat that is physically connected to the computer setup is selected. Each potentiostat differs in how its current range is controlled; hence this control feature enables the use of the program with every potentiostat at our disposal. The physical analogue output channel connected to the rotation can also be selected.
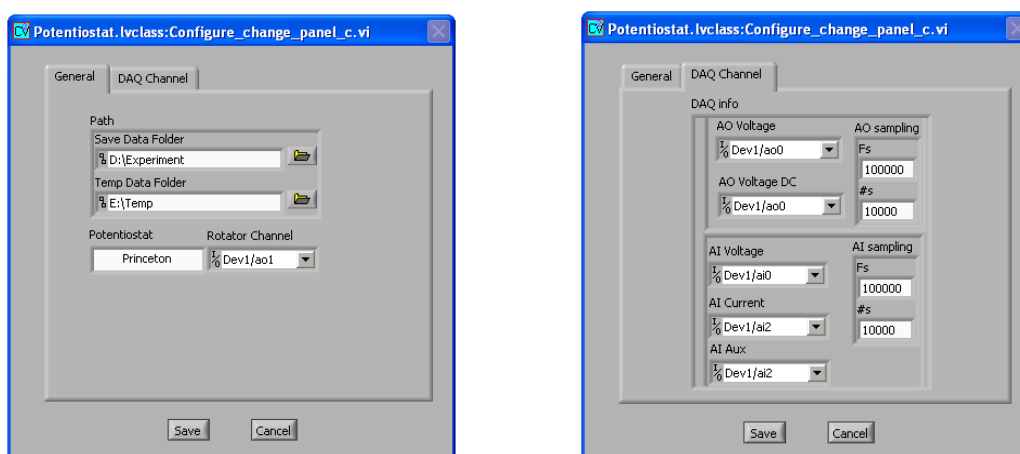
Figure 4.2-5:   Screenshot of the Configuration Panel

In the second tab, the DAC and the ADC parameters are defined. These parameters create a virtual link between the physical channel on the DAQ card and the corresponding digitised quantity. Furthermore, the sampling rate as well as the amount of samples read per iteration of the sub process can be set (see subsection "Write process" as well as "Read process"). In general a sampling rate 10 times higher than the amount of samples read per iteration is used.

Setup Panel

The setup panel, where experimental parameters can be defined in a standardized manner, is shown in figure 4.2-6. This panel has two tabs as well, one is dedicated to the general setup and a single working electrode and the second one to the MWE. On the first tab, the EC cell, the electrolyte, the reference electrode, the solution resistance, and the temperature can be defined. By selecting a new gas, the gas changer device is changed accordingly. Furthermore, additional information about the

working electrode in use can be given, such as its material, the applied loading, RDE tip etc.

A

B
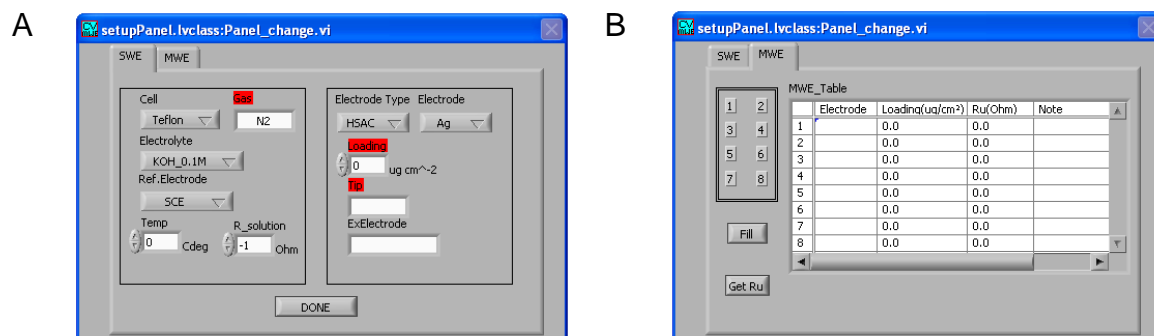
Figure 4.2-6:   Screenshot of the Setup Panel for defining the experimental constants

The second tab is dedicated to the MWE. For each electrode the material, the loading, an additional note as well as the solution resistance can be noted. For the macro and the CV application if the solution resistance is measured, its values can automatically be added to the list by clicking on "Get Ru".

4.2.1.5 Data File

All data files, independent of the EC technique, are saved as ASCII text-files in tab delimited columns, although this format requires more space on the hard drive compared to compressed formats. An example of a data file is shown in figure 4.2-7. The advantage is of using ASCII text is that in general any data analysis program, for example Igor, Origin, Excel, or an in-house developed program, can read the files [49-51]. Hence, it is up to the user to choose the analysis software that is best suitable.
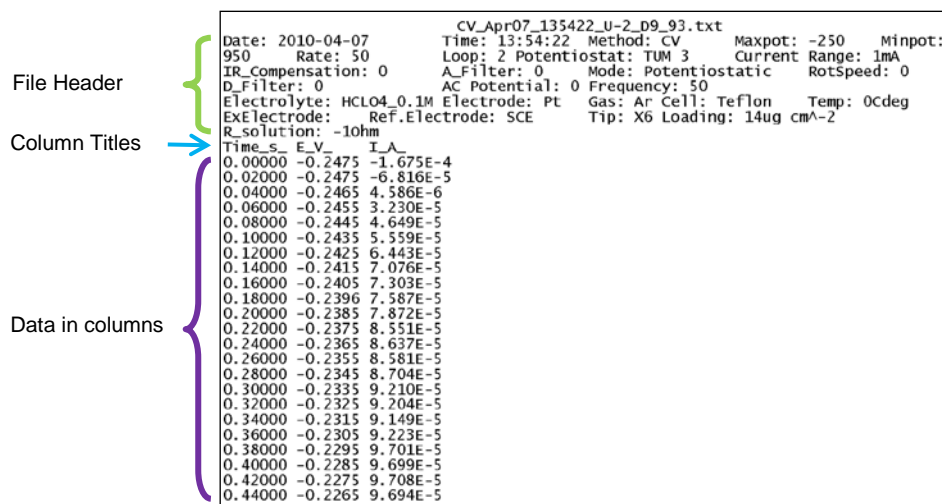
Figure 4.2-7: **Example of the standard formatted data file generated by data acquisition programs. The file is divided into 3 sections: header, column title and data columns, in order to enable standardized import in a data treatment programs.**

The data file consists of three parts; header, column titles and data columns (see figure 4.2-7). In the header, all experimental data is stored. Each entry follows the same pattern according to "<Entry-title>: value<tab>". As a consequence, a data treatment software program can automatically generate lists with these details without knowing in forehand each entry-title. The column titles are given in the form "Quantity_unit_", in order to avoid any confusion about what the file contains and how to store it. The data are listed in columns and the data values are in general limited to 4 or 5 significant digits, in order to reduce the size of the file.

The duration of an electrochemical measurement can last from shorter than a second to hours depending on the technique used. In the former case, a large amount of data files is produced if the technique is repeated over a long period of time. As it is the assembly of data files rather than one specific data point that is important, it is enough to designate the data directories with a rational name rather than each individual file. Therefore, a system to generate standard file names is necessary.

The file names are generated based on the electrochemical technique used, the date and time, some technique specific parameters, and a random number. The following line shows the generated filename from the CV program:

Technique	Date	Time	Tech.paramters	Rand	Ending

CV _ Sep02 _ 153704 _ U-2_D8 _ 61 . txt

The technique specific parameters are in this case the positive and the negative turning points in the CV. Each file has a unique name and can easily be sorted with the usual directory tools.

Each program automatically generates temporary data files with a name based on the rule given above and stores them in the temporary data file directory. The data files are therefore safe even if the host program would crash or the computer stops before the copying phase.

The temporary data files are copied to a new folder when an experimental series has finished. A new folder name will be demanded by a popup window. The folder is thereafter created in the automatically generated folder tree of the structure in the data file folder, as specified in the configuration panel by the following rule:

"data folder" / YYYY_MM / XXXX_YYYY_MM_DD / NN – Name

where Y is the year, M the month, D the day and X the name of the Potentiostat, NN the program name and NAME is the chosen folder name. If the name is already in use in that subfolder, a new name is demanded by the popup window.

4.2.2 General Application Structure

The user comes into contact only with the graphical user interface of the application, without having to care about what is "going on under the surface". Although the previously presented software programs are dedicated to different tasks and are visually different, on a structural level they all share the same main arrangement. The advantage of a common structure is that the code can be reused. Updates of the code will affect all programs using the same code, which saves development time.
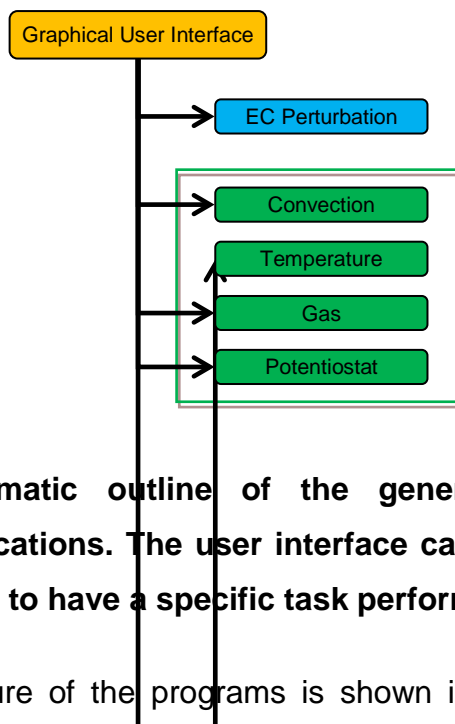
Figure 4.2-8: **Schematic outline of the general structure of the main applications. The user interface calls different sub programs in order to have a specific task performed.**

The hierarchy structure of the programs is shown in Figure 4.2-8. Highest in the hierarchy is the graphical interface, followed by subprograms. The user interface is event based, which means that the program is idle until the user creates an event, such as pushing a button with the mouse. This avoids unnecessary usage of the processor. Upon an event, a subprogram is executed in order to change an experimental parameter or perform a measurement. The sub programs are executed in different threads which permits running them in parallel. For example, the gas can be changed while at the same time a perturbation technique is applied.

Due to their different purposes and internal program structure the subprograms can be separated into two groups: EC perturbation and the accessory controlling. The two next chapters will focus on these groups starting with the EC perturbation.

4.2.3 Potential perturbation sub program

The purpose of this section is to introduce the perturbation subprogram and to point out general aspects on its architecture. There are many considerations which have to be taken into account in order to succeed in writing a DAQ application.

The introduction of fast and high-precision data acquisition cards (DAQ) has facilitated electrochemical measurements because of their digital-to-analogue and analogue-to-digital converter circuitry. The digital-to-analogue converter (DAC) enables the generation of almost any waveform as a quasi analogue perturbation signal, while the analogue-to-digital converter (ADC) records the generated data. The voltage data subsequently has to be converted to the quantity they represent. Rather

than saving all samples recorded by the ADC, a few key values can be extracted in order to reduce the information volume while at the same time preserving its content. Hence, it is important to consider i) what experimental information should be saved, ii) how much data should be saved and iii) where should the data be saved.

4.2.3.1 Overview
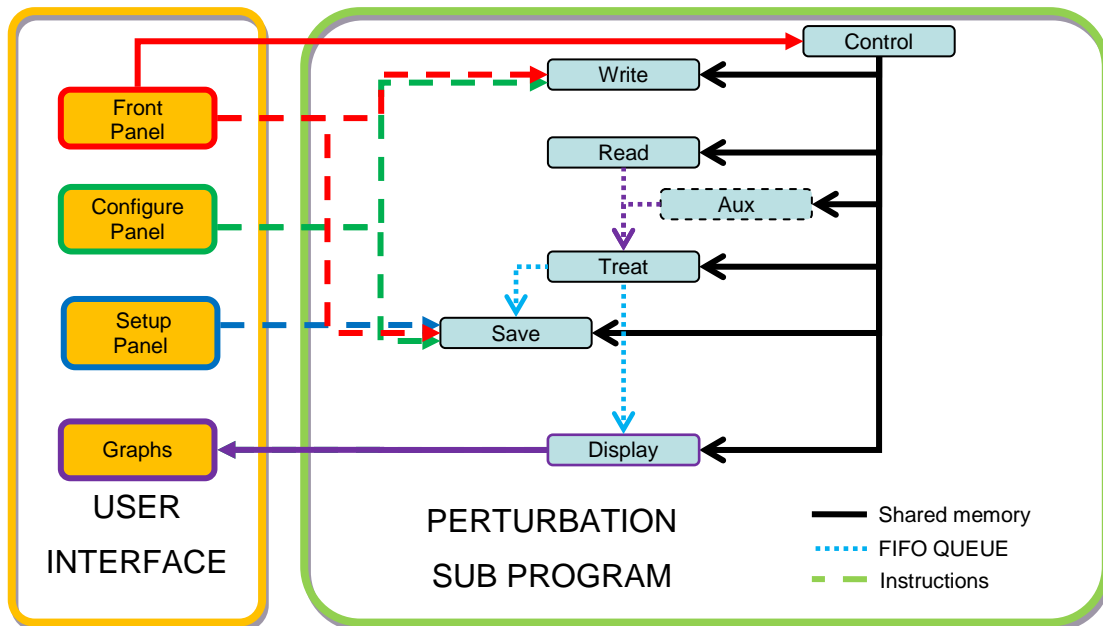
Figure 4.2-9:   **Schematic outline of the potential perturbation program. The arrows symbolise data flow between processes and user panels.**

The schematic outline of the potential perturbation program is shown in figure 4.2-9. The program is divided into 6 different processes; "write", "read", "treat", "display", "save" and "control". They are executed in parallel and run in different threads, as previously discussed. Due to the graphical programming language, the diagram shown in figure 4.2-9 closely corresponds to the actual layout of the program code.

Upon launching one of the sub programs, the technique parameters and the information from the configure and setup panels are sent to the subprogram. The processes are thereafter simultaneously executed.

During execution, there will be a dataflow from "read", via "treat" to "save" and "plot". This is indicated in figure 4.2-9 by dashed arrows, symbolising the FIFO queues. The reading process samples a large amount of data points. The subsequent treat

process refines the data by different mathematical treatments depending on the EC technique. The refined values are subsequently saved in a file and/or displayed to the user.

All of the described applications are based on this schematic outline. However, the differences between them can be observed on the process level. Therefore, the following chapters will be dedicated to explain these more in detail. Note that the basic structure of each process follows the structure shown in figure 4.1-3.

The presented outline also allows an easy implementation of auxiliary data acquisition. One program, controlling the whole experiment, greatly simplifies studies of the correlation between potential, measured current and the supplementary quantity, as it can be monitored online. For example, a modified version of the program has been used in order to build a differential electrochemical mass spectrometer (DEMS) setup.

4.2.3.2 Write process

The Write process controls the analogue output of the DAQ card, i.e. the DAC. The DAC can reproduce almost any arbitrary waveform, as previously mentioned; however, there are some limitations. The analogue representation of a desired value is limited by its quantisation both with respected to voltage and time. The DAC has a given amount of discrete values which can be applied between the maximum and minimum voltage output. In this thesis 16-bit cards were used. This corresponds to 65536 levels over a voltage interval of ±2 V. The smallest possible difference between two voltages is therefore 60 µV. The consensus is that a waveform should be adapted to use as many levels of the card as possible in order to minimise the quantisation error. In addition, a post analogue amplifier might be necessary.

The DAC has a certain sampling rate, i.e. updating rate. In the case of a sinusoidal waveform, this introduces a restriction on the frequency with which analogue signals can be reproduced. Given that at least 10 points are required to make a reasonable representation of a sinus curve, the sampling rate has to be 10 times larger than the desired signal frequency. Typically, the sampling rate is set to 100k samples per second.

As the DAC is frequently updated, a new value always has to be available for the device. The device therefore has a buffer from which the new values are temporary

stored. The software has to frequently provide the DAC buffer with new values otherwise a so-called "buffer underrun" occurs, which stops its execution. The rate, with which the buffer has to be re-filled, depends upon the size of the buffer and the sampling frequency as well as how many new values are written to the buffer in a single writing event. Writing to the buffer is very processor intensive; hence the writing of larger amounts of data less frequently is preferred over single-value writings. Typically, 10k samples are written per event.

In contrast to the DAC, which has an exact and fixed sample rate, the software based loop where the new values are written to the buffer is not 100% deterministic. For certain times the iteration rate can largely deviate from the average because the processor might be occupied with other tasks. In order to avoid a "buffer underrun", the buffer size for the DAC is set to a value corresponding to about 1s of continuous running. The buffer is continuously monitored and if enough space is available, new samples are written. This ensures that the buffer is almost always full and small disturbances would not affect the stability of the program and the stable generation of the analogue signal.

Waveforms suitable for the perturbation of the system, such as potential squares, triangular, sinusoidal or combinations those, are easy to generate with build-in functions in Labview. In order to create a triangular wave for example, the function is given by its frequency, the amplitude and phase as well as the sampling rate and the amount of measured data points. A vector with a discrete representation is generated that can be written into the buffer. Note that if the given sampling rate would deviate from that of the DAC, the analogue signal would be either compressed or elongated.

The outline of this process follows that of a general parallel process shown in figure 4.1-3. During execution, the main process loop iteration is limited to 1 kHz in order to avoid unnecessary processor usage. In each loop repetition, the amount of available samples in the buffer is checked. A waveform is generated according to the corresponding perturbation technique and written into the buffer. In a typical case the length of the waveform corresponds to 100 ms of DAC sampling time.

Once the technique is completed or the control process gives a break command, the process is aborted.

4.2.3.3 Read process

In this process the analogue input channels of the DAQ are controlled.

The operation of an ADC is very similar to that of the DAC. An ADC has the same physical limitation as the DAC, which was described previously. It is therefore important that the analogue signal is conditioned in such a way that as many as possible of the discrete levels are used. In the case of the current measurement, the potentiostat has several current ranges so that the measured voltage always corresponds to a certain interval.

For the sampling of analogue input signals always a distinction has to be made between simultaneously sampled signals and the sequential sampling of channels. In the former case every channel has a DAC, whereas in the latter case, the input signals are re-routed by a so-called multiplexer (MUX) in a way that one DAC can be used for all channels [34]. This has an economical advantage especially for a large number of channels, as a MUX is cheaper than a DAC. The disadvantage, however, is that the maximum amount of samples that can be recorded per channel is inversely proportional to the amount of channels sampled at the same time. Furthermore, the MUX unit enhance cross talk between channels, especially at high sampling rates. This limits the practical sampling rate, which is therefore typically set to 100k samples per second.

During execution, the ADC continuously samples values and places them into a buffer. The ADC buffer has to be repeatedly emptied otherwise the buffer might be full and data points will be lost due to overwriting which will abort the execution. As previously mentioned, the deterministic characteristics of a software loop is limited, hence the buffer size has to be considered in order to avoid a software crash in case of extreme events. The buffer size is set 1 s.

Reading from and analogue writing to the ADC buffer is very processor intensive; hence this should not be done too often. On the other hand, the user wants to see the data in real time and in a steady flow. A reasonable compromise is to read from the buffer about 10 times per second. This can be set in the software program by the user in the configure panel setting the ratio between sampling rate and read samples. The latter is typically set to 10k samples.

The outline of the process follows that of the general parallel process shown in figure 4.1-3. Similar to the write process, the iteration rate of the main loop is limited to 1kHz. The amount of samples in the buffer is controlled in each interaction. If the

buffer contains enough samples, a certain number of samples are read and put into a FIFO queue as one data package.

The read data are packaged in an array of waveforms corresponding to the amount of sampled channels. A waveform contains an array of samples along with a time stamp and the time space between the samples. It is thereby possible to calculate the exact time at an accuracy of $< 1\mu s$, when a specific sample was taken, which is useful for the subsequent data treatment. Furthermore, independent of the technique at least 2 channels are sampling: The potential and a voltage which proportional to the current through the WE. In the case of the MWE, additionally 8 current channels are sampled simultaneously. However this changes not the design of the process.

The process is only aborted if the control process gives out a break command or an error occurs.

4.2.3.4 Treat process

As indicated in figure 4.2-9, after the read process the treat process is next in line in the data flow. The aim of the treat process is to reduce the large amount of voltage samples into a few values containing the key information. In addition, the measured voltage representing the WE current has to be back-converted into a quantity corresponding to the real current. Thereby the current range of the potentiostat has to be taken into account. Although the key information differs depending on which perturbation technique that is used, the general structure is the same.

The process layout deviates somewhat from the general process (see figure 4.1-3) and the two previous processes as the treat process does not need a rate control. Instead, the loop waits for a new item in the data queue. As soon as a data package is in the queue, the item is removed and treated. In average, the rate of the loop mimics that of the "read" process; however, at times a large deviation can exist if the processor is occupied. This poses however no problems to the stability of the program.

After the treatment performance, the reduced data are put into other queues in order to be displayed to the user and saved into a data file in other processes.

Each electrochemical technique demands an individual data treatment, so in the following they are described in more detail.

4.2.3.4.1 CV + AC

In order to compare CVs recorded with different scan rates the vast amount of measured samples has to be reduced. This is done by averaging over a timeframe (t_{avg}) according to the following equation:

$$t_{avg} = \frac{1\,mV}{Rate}$$

where the rate is in mV/s. The amount of saved points is thus independent of the scan rate and is only proportional to the difference between maximum and minimum potential in the CV.

If the potential sweep is superposition by an AC signal, the signals from the potential and current channels are extracted with respect to amplitude and phase using a digital lock-in algorithm. The ratio of these values is subsequently calculated in order to obtain the complex impedance.

Additionally, in order to make a distinction to which cycle the data belongs, a "new cycle" notification is sent via the queues to the display and the save process prior to the start of a new cycle.

4.2.3.4.2 Chronoamperometry, Chronovoltammetry + AC

For the chronometric techniques, i.e. chronoamperometry and chronovoltammetry, the user can decide how many points should be saved per second. The sampled voltage points are then averaged to the correspond timeframe. This permits the user to optimise the time resolution in order to reduce the size of the data files.

In addition the dynamic averaging mode can be chosen as well. In this mode, from the time of the potential step, for the first 30 seconds the data are averaged to 10 points per decade of time and afterwards to one point per second. This mode allows fast transients to be recorded and saved, with a minimum amount of data points, as the time resolution is optimised only in the time frame where it is required.

In the case of an AC signal superimposed to a CV, within the chosen timeframe the signals from potential and current channels are extracted and the complex impedance is calculated.

4.2.3.4.3 SWV

Similar to chronometry, square wave voltammetry has two modes of extracting the data values as well. The sampled values are average to a certain number of points

per second, as defined by the user. In the additional dynamic mode, only one point is saved per potential step. Just before a potential step, a few samples are selected and averaged to one point.

4.2.3.5 Display process

In the display process, the treated data are collected in order to display the measured data to the user.

The rendering of graphs is a processor demanding task, hence this should not be done excessively. On the one hand, a high update rate makes the visual impression smoother, on the other hand the screen has a refreshing rate of about 100 per second [52], which sets the maximum limit for a reasonable rendering rate.

In order to set the optimal update rate, the process has two different main loops. The first loop consumes the queue of treated data and stores it in a "local" memory. The memory space is limited to 5000 items and at each iteration the old value is exchanged by a new one. Similar to the main loop of the treat process, this loop has no rate limitation. It waits on the next element in the queue. The second loop updates the graphs on the front panel. The iteration rate of this loop is limited to 10 times per second. At this update rate, the data are displayed almost continuously, as it would the case for an analogue instrument.

The display process for CVs has an additional feature as a colour distinction is made between the different cycles. The last three cycles are stored in the first loop. At the arrival of a "new cycle" notification, the oldest cycle is discarded and replaced by the more recent one.

4.2.3.6 Save process

The Save process stores the treated data in files. The form of such a file has been shown in figure 4.2-7.

The data file has to be created and in a certain sequence written to. Therefore, upon the launch of the process, a file is created in the directory for temporary files (see chapter Data File). As indicated in figure 4.2-9, setup and technique details are gathered from the user panels and written to the file, followed by the headers of columns. The header names depend on the technique and also the amount of working electrodes.

The main loop corresponds to that shown in figure 4.1-3. A rate control, however, is not required as the loop is paused until a new item is added to the queue by the treat process. As soon as an item is detected in the queue, it is written to the file. In the case of a program failure, the data up to that instant are saved on the hard drive.

A difference exists in the save process of the CV compared to the other programs: A new data file is generated at the start of a new loop. As soon as a "new loop" indicator is sent via the queue, the file is closed for writing. Simultaneously, a new file is created as described previously.

An additional difference in the CV save process is that at arrival of a "new loop" notification, the amount of completed loops is compared to the one set by the user. If all loops are completed, the process is aborted together with the whole subprogram. This abort condition ensures that the data from the complete last cycle are saved.

4.2.3.7 Control process

The main purpose of the control process is to monitor the status of the other processes and to centrally handle a user abort command.

The process consists therefore of a rate limited loop that reads from a global variable. In this global variable all running processes share information about their status via a global variable, see figure 4.2-9. In the case of a failure of one of the processes or the exit command, all processes can be stopped. For the techniques with predestined duration, this process contains a count-down timer and stops the processes when completed.

4.2.4 Accessory controlling sub program

The main program can also open one of the accessory controlling sub programs, as illustrated in figure 4.2-8. This class of programs are exclusively developed in order change the physical state of an experimental setup, such as temperature.

The instrument in our setup has an internal processor with memory. Its internal parameters can be remotely set and controlled. Once set, the setting will stay until a new value is sent.
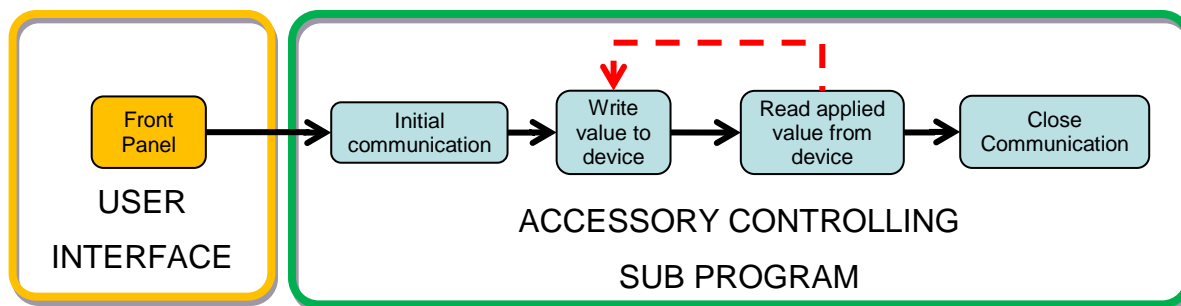
Figure 4.2-10: Layout of the accessory controlling sub programs. A sequential scheme is used due to the required single event action.

The basic structure of these programs therefore differs from the EC perturbations, as only sporadic control is required in case a value needs to be changed. The structure, see figure 4.2-10, is therefore based upon the sequential scheme described previously. The user panel sends a new set of values that should be applied to the sub program. The subprogram starts by initializing a communication session with the device. After establishing contact, the values are sent to the device. Subsequently, the newly set-values are requested from the instrument in order to double-check if the new values have been applied. Lastly the communication is closed and the subprogram exits.

Although the programs share the overall structure, the differences on the sub level are considerate. A short description of the used subprogram is given in the following.

4.2.4.1 Potentiostat – change of current range

This subprogram changes the current range of the potentiostat, i.e. sets the current-to-voltage conversion factor. The input of the program is the new current range of one of the values: 1 µA, 10 µA, ..., 1 A.

Each potentiostat is commanded via different interfaces and has a diverse amount of current ranges. For example, the Princeton 263A is commanded via GPIB and has 5 ranges between 1 µA and 100 mA, while the in-house constructed potentiostats are controlled via the digital channels of the DAQ card and have 4 ranges between 1 µA and 10 mA. Hence, upon execution of the program, a specific code is used based the configuration settings (see Configure Panel) fitting only to the selected potentiostat. Additionally, if the selected current range is not available, the closest existing one is selected. The selected current range of the potentiostat is always double-checked as

previously described. Hence, for the calculation of the current from the measured voltage representation, always the correct conversion factor is used.

4.2.4.2 Gas control

This program changes the position of the gas valve that subsequently a different gas will be used to purge the cell (see chapter "Automatic gas changer"). The user input of the program is the name of the new gas.

The names are mapped with respect to the valve positions of the connected gas lines in order to generate a number. After a serial connection to the control unit of the gas valve is established via the RS-232, the number is transferred and the valve position is changed. Furthermore, a command asking for the applied valve position is sent to ensure that the correct execution of the command.

4.2.4.3 Temperature and magnetic stirrer control

This program changes the temperature and rotation rate of the magnetic stirrer of the IKAMAG from the company IKA AG. The communication with the device is performed via RS-232, as in case of the gas changer. The communication protocol used by the IKAMAG differs however from that used by the gas changer; hence the code from the gas changer cannot be reused.

The user input of the program is temperature in °C and rotation rate in rpm, and the Boolean: "wait on temperature?". A serial connection to the device is established and subsequently both numbers are sent to the device. If the Boolean is true, the program will continuously demand the current values of the temperature and rotation. This is done with a frequency of 1 Hz until the right temperature has been reached (±0.5 deg.). This halts the macro list execution until the new temperature is reached.

4.2.4.4 RDE Rotation control

This program controls the rotation rate of the RDE device from Radiometer. The input of this subprogram is the rotation rate in rpm.

The electrical control unit of the device has an input where an applied voltage is converted to a rpm rate. An applied voltage of 1V corresponds to 1000rpm. Such a voltage can be supplied by the DAQ card. Based on the selected channel (see Configure Panel), the DAC is updated with the calculated voltage.

4.3 Data analysis application

Using an automatic experimental setup, the data treatment can become the bottle neck in the chain of fully characterising a catalyst. The initial data treatment, where the data are reduced to a few characteristic values is in general time consuming. A high sample throughput, especially when using a MWE, demands a fast and easy data treatment.

To give an example: for every catalyst sample, the active surface area and the kinetic activity for a specific reaction have to be determined. Although only rudimentary mathematics is required in order to extract these values, the challenge lies in the combination of the measured data files in order to cancel out unwanted measure effects. Nevertheless, the same extraction procedure can be used for all catalysts. A specialised program for this purpose can therefore significantly reduce the time to treat the data.

Equally important is the data management. Backtracking of old results can be time demanding and a system for fast backtracking is therefore required. For that purpose automatically generated standard HTML reports can be used. Browsing through HTML pages is much faster compared to loading files into any advanced program.

A standard data treatment program, such as IGOR, ORIGIN or EXCEL, can be used for the data treatment as the text data files from the data acquisition program can be read by those programs. The programs feature text based programming of specialised scripts and the creation of customized user panels in order to reduce the amount of specific tasks for the user. Excessive text based programming, however, would be required in order to create a specialised platform for our purposes.

Thus for the purpose of data analysis and data treatment in this thesis a specific software programs based on LabVIEW was written. The software called "EC_Treat" program was developed in order to facilitate the extraction of the characteristic values of a catalyst from the acquired CV data; independent whether a single working electrode or a MWE is used. The characteristic values are calculated with a minimum of user interaction. In order to support further data treatment, the program exports the results directly into Microsoft Excel. A standard html report can be generated as well, which enables a fast verification of the data.

In the following a brief description of the program capabilities is given.

4.3.1.1 Main Panel
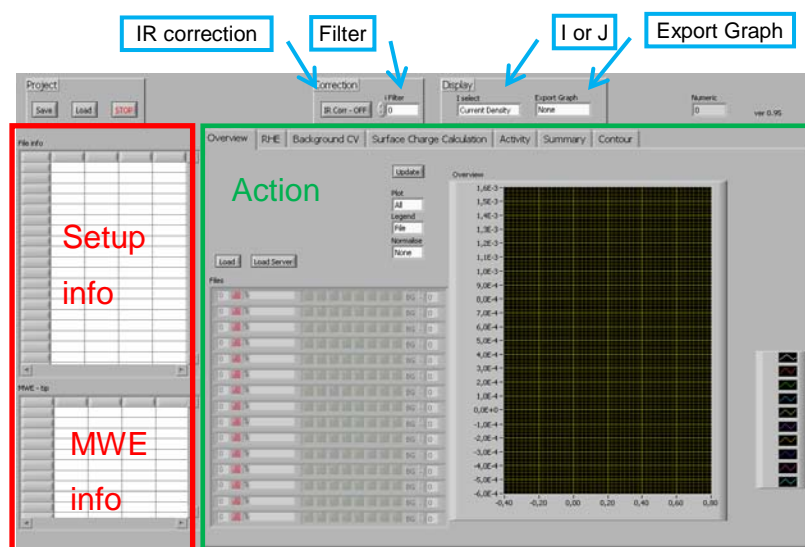
Figure 4.3-1: **Screenshot of the front panel of the data analysis program.**

A screenshot of the main window of the "EC_treat_data" - program is shown in figure 4.3-1. The window is divided into two main parts with tabulated information of the measurement (red) and with the action panel (green). In the setup table, all informations saved in the file, such as date, measure parameters etc. are listed. The MWE specific information is shown in the second table. The action panel contains several tabs or pages: Overview, RHE, Background CV, Surface Charge Calculation, Activity and Summary. Each tab is dedicated to a specific action based on the tab name. A more detailed description of the actions will be given in what follows.

As shown in figure 4.3-1, there are four additional features. The data can be smoothed if necessary. Inscribing any integer except for 0 in "Filter" activates a filter with a left and right range according to the number. The sign of the number determines which filter type is used; a positive value results in a mean filtering while a negative value results in a median filtering. Note that the raw data are never filtered; only the duplication used the rendered images. Furthermore, the voltage can be corrected for the deviation caused by the solution resistance by pressing the "IR correction button". The program uses the solution resistance values given in the file in addition to the current channel data in order to calculate the correction values. Analogue to the filtering, the IR correction only affects the rendered images.

Additionally, the current can either be displayed as current or current density with respect to the geometric surface area. Lastly, every graph in the program can be exported. Selecting a graph in "Export Graph", the specific graph is saved as a .png-file and as a tab separated text spread sheet. The spread sheet subsequently can be loaded into an external program (IGOR, ORIGIN etc.) for the rendering of more visually attractive images [49-50].

4.3.1.2 Overview page
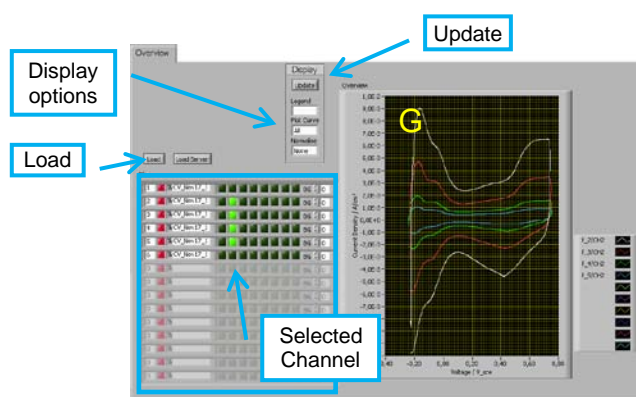
Figure 4.3-2:   Screenshot of the data treatment tool: Overview. From this view files can be loaded to or removed from the memory. The data raw data easily be viewed.

In figure 4.3-2, a screenshot of the first action page, the "overview", is shown. This page is used to load data files and discriminate the interesting ones from a large amount of data files.

The loaded files appear in a list (blue). Each line carries an order number, file name as well as green and dark green squares corresponding to the available current channels in the data file. The order number is used in the subsequent action pages to select a specific file. Furthermore, files can be unloaded by clicking on the red square with an "x".

The data are plotted by marking the specific channels and clicking on "Update". Subsequently, the data will appear in the I-V graph "G". Prior to an image rendering, the user has several display options: i) the current can be normalised to help distinguishing between different effects. The normalisation can be done to the catalyst loading, the rate and rotation rate, as well as to the square root of the rate

and rotation rate; ii) the displayed data can be limited to certain parts of the CV such as the positive or negative sweep. Furthermore, the data can be displayed as the difference between the positive and negative sweep or as the average of them; iii) to each graph per default a legend is generated and the user can choose on which experimental parameter the names should be based. These display options are given in each of the subsequent pages.

4.3.1.3 RHE page
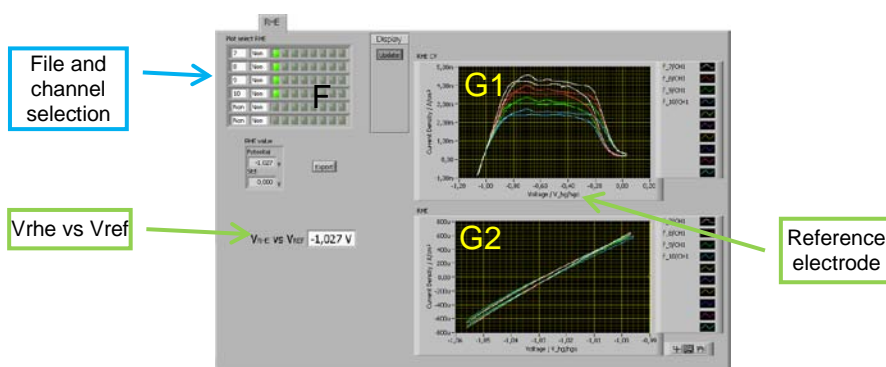
Figure 4.3-3:   Screenshot of the data treatment tool: RHE determination. This view is used to extract the RHE values from measurements.

In the second action page, as shown in figure 4.3-3, the RHE value with respect to the used reference electrode is calculated. Once the RHE value has been determined, all I-V graphs are shifted accordingly in order to display all data with respect to the RHE. In order to avoid ambiguities, the reference electrode to which the voltage is referred is shown in each graph.

In order to select measurement files and channels for the RHE calculation, the user can select a number from a pull down list in listing "F". The selected number corresponds to the order number of the files listed on the "overview" page. Again, the green squares correspond to the available current channels of the specific file. All the subsequent pages follow this prototype of channel selection.

After the selection and a click on "update", the data are shown in graph "G1". The second graph, "G2", automatically shows a zoomed-in area around the current zero crossing. The average voltage of the zero crossing is subsequently calculated and presented in "Vrhe vs Vref".

The user can also define a RHE value if no experimental data files are available. This is done by inscribing the known potential value versus the reference into "Vrhe vs Vref".

4.3.1.4 Background CV page
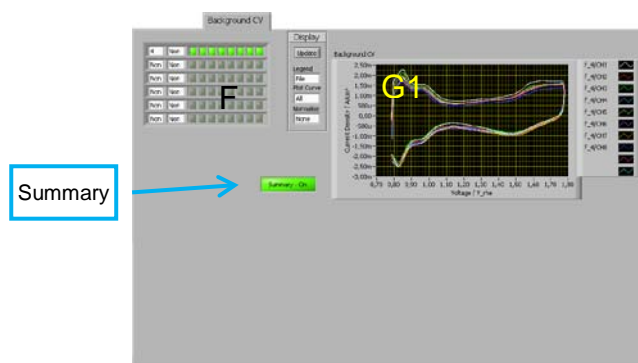
Figure 4.3-4: **Screenshot of the data treatment tool: Background CV in Argon. The displayed graph will be part of the generated summary report.**

The third action page "Background CV" (figure 4.3-4) is dedicated to render an image of the catalyst in the absence of a continuous reaction for the HTML report.

Like in the previous cases, specific current channels can be selected and normalised before visualised. Moreover, a legend to the graph is generated based on a chosen experimental parameter. A copy of the graph "G1" will appear in the report (see figure 4.3-8). Nonetheless, this section can be excluded from the report if required by setting the "summary" button to the off position.

4.3.1.5 Surface Charge Calculation page
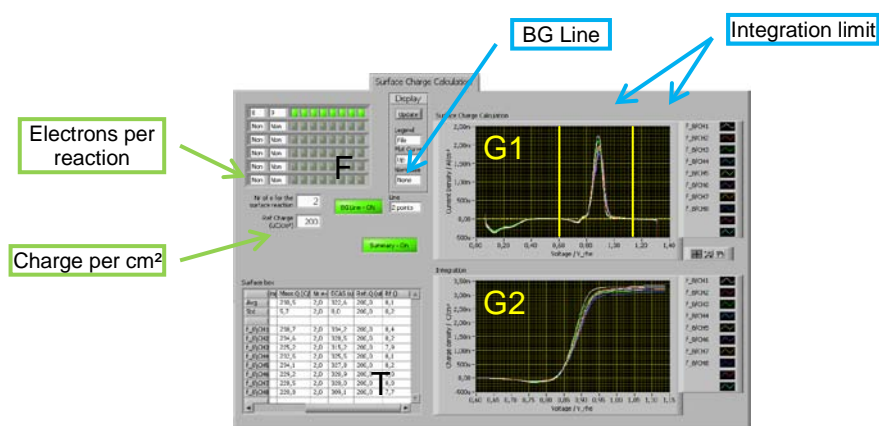
Figure 4.3-5: Screenshot of the data treatment tool: Calculation of surface charge. The integration limits are manually set at "G1". The resulting integral function "G2" and value of the integral "T" are shown for all selected curves.

The calculation of the specific charge from a stripping experiment is done in the action page "Surface Charge calculation", as shown in figure 4.3-5. In order acquire this value, the current response from a background corrected stripping linear sweep voltammetry has to be integrated.

The calculation is performed by selecting the data files of the current channels as well as a background measurement. The resulting I-V curves are shown in graph "G1". In graph "G1", the two vertical marker lines, which can be moved by the mouse, indicate the integration limits. With the help of the data at these marker positions, if required an additional two-point or single vertical background line can be generated and subtracted from the data.

The integrand is shown in graph "G2". Ideally it should have two plateaus at the beginning and at the end. A deviation from this form indicates an uncorrected offset.

A summary of table "T" shows the calculated stripping charges for each current channel as well as the average and the standard deviation of the entire data set. Based on the stripping charge, normalised quantities are automatically calculated as well. Using the defined number for the amount of electrons for the specific stripping reaction, as well as the material factor "surface charge density", the charge density, the charge per gram, the NECAS, the specific surface area and the roughness factor

can be calculated. The table contains all normalisation factors in order to facilitate the post verification of the treated data.

4.3.1.6 Activity page
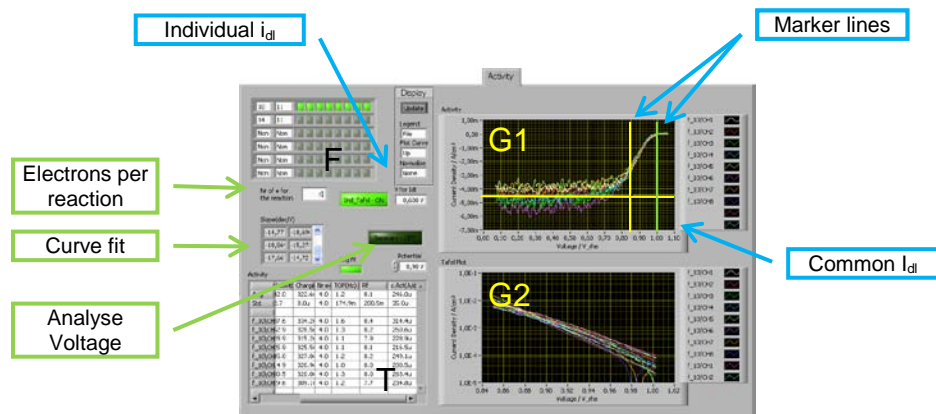
Figure 4.3-6: **Screenshot of the data treatment tool: Activity. The kinetic region is manually set "G1". The Tafel plot of the defined region is shown in "G2" and the calculated activity is shown in "T".**

Figure 4.3-6 shows a screenshot of the action page "Activity", where the reaction activity is calculated. In order to acquire the kinetic activity; the measured data have to be background corrected as well as subsequently corrected for the diffusion limitation.

Similar to the previous case, the data files and current channels containing the data from a stripping and a background measurement are selected. The resulting I-V curves are shown in graph "G1". In graph "G1", the two vertical marker lines indicate the potential range where the diffusion limited current can be extracted. A horizontal line defines the diffusion limited current that will be used for correcting the data. In case the measured diffusion limited currents diverge between the different channels, an individual diffusion limited current has to be used. The individual i_{dl} values are defined as the current at a specific voltage.

The corrected data are shown in the Tafel plot "G2". The potential range is defined by the two markers in the previous graph. An exponential function can be fitted to the data in order to determine the Tafel slope. Lastly, the activity for each channel at a specific voltage is shown in table T. In addition, the normalised activities, i.e. the

specific activity, the mass activity and the TOF values are automatically calculated if the surface charge has previously been acquired.

4.3.1.7 Summary page
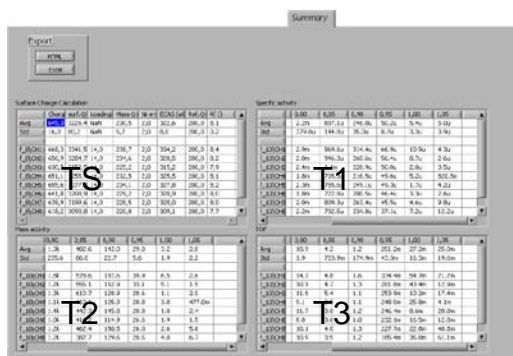
Figure 4.3-7: **Screenshot of the data treatment tool: Summary tab. In tables shows the surface charge calculation "TS" as well as the normalised activities, i.e. the Specific Activity "T1", the Mass Activity "T2" and the TOF "T3".**

The 6th action page, the "Summary" provides an overview of all the calculated characteristic values presented in four tables, as shown in figure 4.3-7. The table TS displays the surface charge calculation. The other three tables exhibit the normalised activities, i.e. the Specific Activity "T1", the Mass Activity "T2" and the TOF "T3". As the activity is a function of potential, the presented activities are given at different potentials, from 0.6 to 1.1 V in 50 mV steps.

For further data treatment, these tables can be exported into excel. Upon a mouse click on "Export Excel", Microsoft excel is launched and a new file is created. The tables are subsequently generated in different work sheets titled accordingly. The specific experimental parameters are exported as well.

The HTML report can be generated by clicking on "Export HTML". The report contains the experimental information followed by the images from the tabs with a highlighted "Summary" as well as the summary tables. An example of a generated report can be seen in figure 4.3-8. Note that the report has been printed in order fit into this document. In its original form it is more compact and would not appear as different pages.
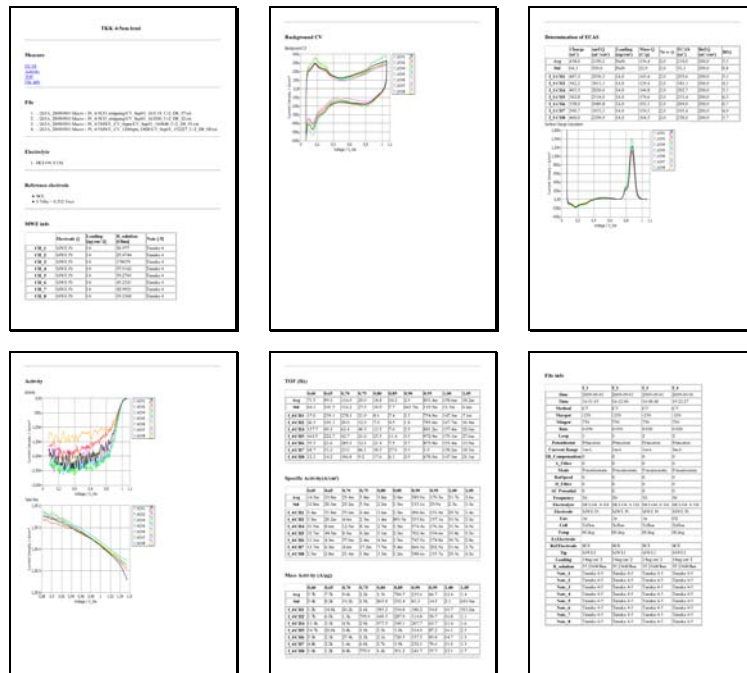
Figure 4.3-8: Screenshot of an example of a generated HTML Report. The report features all graphs and tables generated at the different data treatment tabs. The information of the used data files is also included.

5 The influence of platinum oxide formation on its catalytic properties

5.1 Motivation

As a result of its high catalytic activity towards the oxygen reduction reaction and hydrogen oxidation reaction (HOR) platinum is one of the most studied metals in electrochemistry. Although Pt is considered to be the most active metal for these reactions, the ORR still exhibits a significant overpotential of more than 0.2 V, i.e. oxygen reduction currents are only observed below 1.0 V_{RHE}. In fact the observed overpotential is one of the main inhibitors for large scale applications of low temperature fuel cells as it reduces the efficiency of the conversion of chemical into electrical energy. Thus studies on the nature of the overpotential are both of fundamental as well as applied interest.

In previous experimental investigations of the ORR on Pt based on its pH dependence and the comparison of Tafel slopes it was concluded that the first charge transfer to the oxygen molecule is the rate determining step (rds) [53-55]. Furthermore, it was assumed that at low overpotentials the surface coverage of oxygen intermediates affects the activation energy of the process while at high overpotentials the influence becomes negligible. Later the concept of intermediates affecting the reaction rate was extended to the influence of spectator species, i.e. species not directly involved in the reaction but adsorbed on the surface and thus blocking reaction sites [56]. A typical example for such a spectator species is the co-adsorption of chloride anions from the electrolyte [57]. In this respect the adsorption of OH exhibits a special role in aqueous electrochemistry. OH_{ad} may be formed directly from water and act as a spectator species or it is a reaction intermediate during oxygen reduction. Recent theoretical descriptions of the ORR based on density functional theory (DFT) calculations by Norskov et al. indicate that water dissociation and the ORR are indeed two sides of the same phenomenon [58-59]. Indifferently whether the oxide species (adsorbed oxygen atoms or hydroxyl) originate from water dissociation or oxygen molecules, the strong interaction with platinum at potentials close to the equilibrium impedes the proton and electron transfer. Only by lowering the potential, the stability of the oxygen bond decreases and the ORR may proceed.

As a consequence, in order to probe the ORR, the key is to understand the adsorption of oxygenated species from water, i.e. the Pt oxide formation. Such studies are best performed in alkaline solution, where except for OH no additional anions such as chlorides are present in solution. The correlation between the oxidation of the platinum surface and the measured catalytic activity is demonstrated in figure 5.1-1, where the cyclic voltammogram of polycrystalline Pt recorded in argon saturated 0.1 M KOH solution is compared to the polarization curves recorded in the same solution but saturated by different other gases. Taking the ORR as an example, in accordance with previous reports [60], it is seen that at potentials >0.8 V_{RHE} a clear correlation between the decrease in ORR current and the surface oxidation peak in the CV is evident. A major challenge, however, is the determination of the potential dependent nature and steady-state or equilibrium coverage of surface species. Not only can discrepancies be found in literature if different electrochemical techniques are used [61-62] but also the dependence of the current response on the surface preparation complicates the data interpretation. For that reason probing the free Pt sites, using a catalytic reaction, such as the hydrogen oxidation [63], can give additional insights.
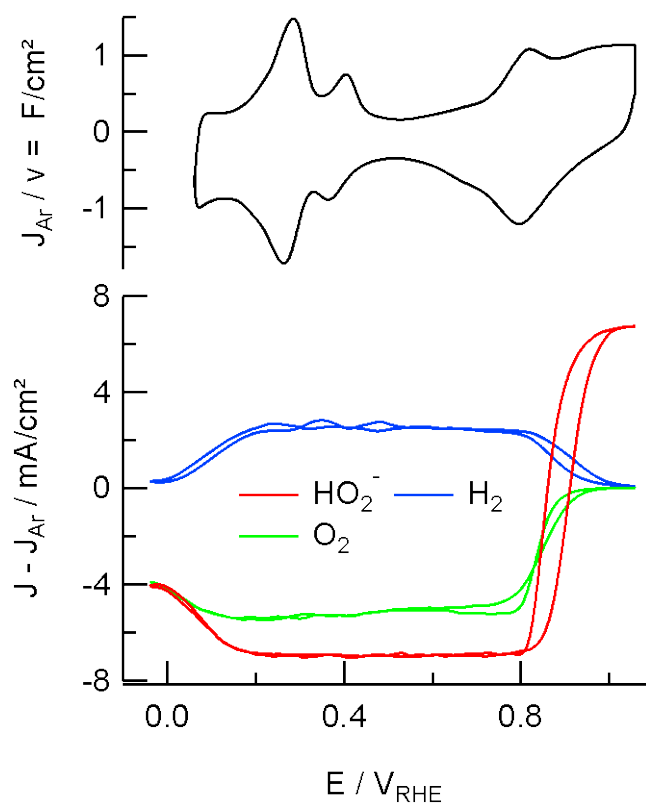
Figure 5.1-1: **Cyclic voltammogram and polarization curves of Pt recorded in 0.1M KOH solution saturated by Ar (black), hydrogen (blue), oxygen (green), and with peroxide added to the solution (red).**

The scope of this part of the thesis was to re-examine the role of surface oxides on the kinetics of several important reactions on platinum in alkaline solution. The hydrogen oxidation reaction, the oxygen reduction reaction as well as the oxidation/reduction of peroxide (POR, PRR) are studied by different electrochemical techniques and the results are compared to each other.

5.2 Experimental details

All electrochemical measurements were conducted in a setup developed in this thesis and described in the previous chapters. The electrolyte solutions 0.1 M $HClO_4$, 0.1 M KOH and 0.1 M KOH containing H_2O_2 were prepared using Millipore water (Resistivity = 18.2 $M\Omega cm^{-1}$, TOC < 5 ppb), concentrated $HClO_4$ (Normatom; VWR, Germany), KOH pellets (Merck, Superpure) and 30% H_2O_2 solution (Merck, analytical grade). During measurements, the electrolyte was saturated with argon, oxygen, or hydrogen, each of purity grade 5.

117

As reference electrode, a Mercury oxide electrode was employed, however, the reversible potential of hydrogen oxidation/reduction was determined for each measurement, and all presented data are given with respect to the reversible hydrogen electrode.

The working electrode used was a PC Pt disk ($\emptyset$ = 5 mm, A = 0.196 cm²) mounted into a Teflon RDE tip. The disk was cleaned by polishing, inserted into a sonic cleaner and finally inserted for 5 min in concentrated $HClO_4$.

Prior to each experimental series, the Pt electrode was cycled in CO saturated perchloric acid (CO annealing) in a separate cell in order to obtain reproducible surface conditions [64]. The electrode was thereafter rinsed in Millipore water and finally inserted into the cell containing KOH solution.

The solution resistance between the working electrode and the Luggin capillary [12] was determined using an AC signal (5 kHz, 5 mV), and thereafter electronically compensated for using the potentiostat´s positive feedback scheme. The resulting effective solution resistance was 2 Ω for each experiment.

5.3 Results

5.3.1 Cyclic voltammetry
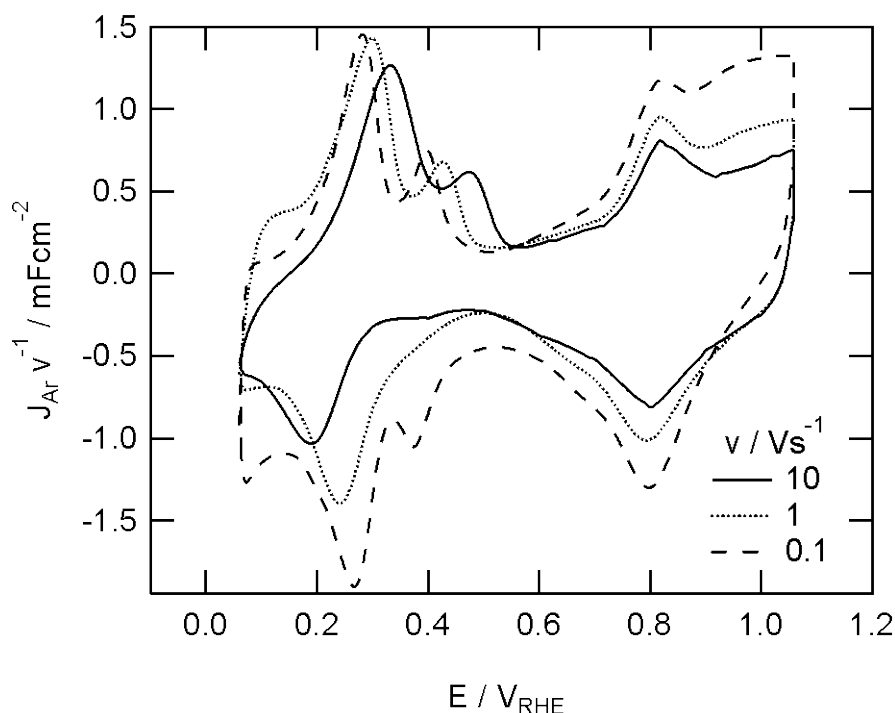
Figure 5.3-1 **Cyclic voltammograms of Pt in Ar saturated solution recorded at different scan rates in 0.1M KOH solution.**

Cyclic voltammetry is a practical tool for a basic characterization of the properties of an electrodes surface. In order to examine adsorption processes and to distinguish them from other faradaic processes, the measured current density J can be normalized to the scan rate v. While the current related to adsorption processes is both proportional to the scan rate and a function of potential, faradaic processes are only a function of potential. Hence by varying the scan rate, information about the dynamics of the surface processes become easily accessible with a minimal distortion from background processes. If such studies are performed using probe reactions serious complications arise as a result of the superposition of different processes in the measured current. Thus for studying the dynamics of the oxide formation/reduction on Pt and its influence on continuous faradaic processes, the current responses from the different surface processes have to be separated.

In figure 5.3-1 CVs of polycrystalline Pt recorded in Argon saturated 0.1 M KOH are shown. At a low scan rate (0.10 V s^{-1}) the well known base voltammogram of

polycrystalline Pt recorded in alkaline electrolyte is observed. In the H_{upd} region between 0.05 and 0.5 V_{RHE} two well defined peaks evolve due to the adsorption/desorption of hydrogen atoms at different facets of the polycrystalline Pt crystal, whereas the pseudocapacity between 0.5 and 0.75 V_{RHE} is traditionally ascribed to charging and de-charging of the electrochemical double layer close to the surface. Beginning at 0.7 V_{RHE} in the positive going sweep, oxygenated species become adsorbed on the surface. In contrast to H_{upd} this process is reported to be irreversible based on the negative shift of the reduction peak in the negative going sweep, especially when scanning to more positive potentials (not shown). However, increasing the scan rate it can clearly be seen that the oxide peak position, both in positive and negative scan direction, is independent of the scan rate up to very high rates ($\leq$10 V s^{-1}). In contrast, the peaks correlating to the H_{upd} process merge with increasing scan rates together and shift to more positive/negative potentials in the positive and negative going sweep, respectively. These observations, which to the best knowledge of the author were not reported previously, suggest that in alkaline solution the initial oxidation of the Pt surface and its reduction are relatively fast processes, whereas the H_{upd} process is comparatively rather sluggish. Note, however, that although the initial oxidation is fast, the magnitude of the peak current decreases as v increases indicating that the equilibrium oxide coverage is not reached instantaneously. It is noteworthy in this respect that these observations can be only obtained if almost a full compensation of the solution resistance in the electrochemical cell is achieved.

5.3.2 Separation of faradaic and capacitive currents
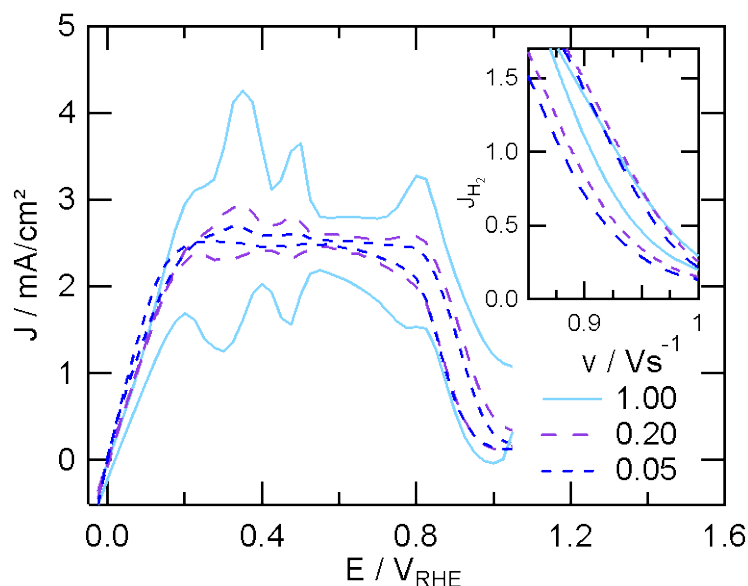
Figure 5.3-2 **Polarisation curves of PC Pt recorded at different sweep rates in hydrogen saturated 0.1 M KOH solution. The inset shows parts of the polarisation curves after subtraction of a CV recorded in Ar saturated solution at an equivalent scan rate.**

As discussed in the introduction of this chapter, an alternative tool for the characterization of Pt surfaces is to probe the influence of adsorption processes on catalytic reactions such as the hydrogen oxidation reaction. While the currents of adsorption/desorption processes scale with the applied scan rate catalytic reactions do not. Thus the current responses from the different surface processes have to be separated. This is demonstrated in figure 5.3-2, where polarization curves recorded in hydrogen saturated solution are compared for different scan rates. At low scan rate (0.05 mV s^{-1}), in the polarization curve mainly the well known characteristics of a continuous faradaic process can be observed, i.e. close to the reversible potential of the HER/HOR (0.00 V$_{RHE}$), the measured current is controlled by the kinetics of the hydrogen oxidation, whereas in the region $0.1 < E < 0.8$ V$_{RHE}$, it is limited by the diffusion of hydrogen to the surface. Above 0.8 V$_{RHE}$ the current decreases until around 1.0 V$_{RHE}$ it almost reached zero, corresponding to the oxidation of the Pt surface indicated in the CV. Note also the hysteresis (i.e. the difference between positive and negative going sweep) in the oxide region, in contrast to the region

121

around the reversible potential. In addition to these faradaic currents, only very small features of the adsorption and desorption of hydrogen, as obeserved in the CV recorded in Ar saturated solution, are discernible in the polarization curve.

Increasing the scan rate, H_{upd} and platinum oxidation features superimposed onto the HOR appear more clearly. If a CV recorded with the same rate in Ar saturated solution is subtracted the surface features can be removed and the activity of the HOR extracted. Focusing on the oxide region as shown in the inset, the resulting positive sweep curves are almost independent of the scan rate. In contrast, the negative sweep curves exhibit a hysteresis which becomes more pronounced as the scan rate decreases. Analogue to the HOR, performing this procedure in O_2 saturated electrolyte leads to similar observations.
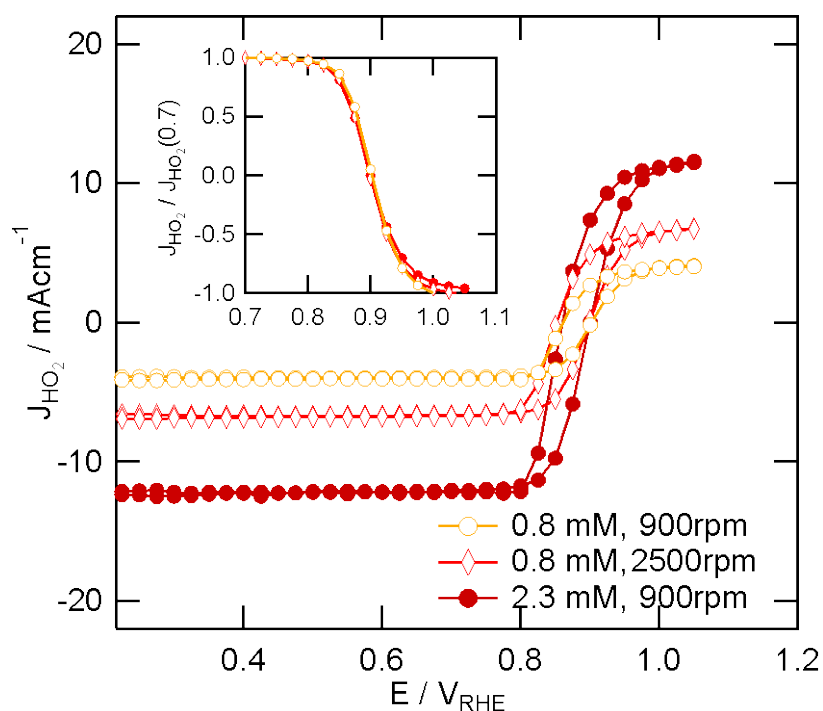
Figure 5.3-3   Polarisation curves of the oxidation and reduction of HO_2^- recorded at different rotation speeds and peroxide concentration in Argon saturated 0.1 M KOH solution. The inset shows the normalised positive going linear sweep voltammetry.

As peroxide is discussed in the literature as a reaction intermediate in the oxygen reduction reaction [65], the reduction/oxidation of hydrogen peroxide was investigated as well. For this purpose H_2O_2 was added to Ar saturated solution and

CVs were recorded at $0.5\,Vs^{-1}$. The resulting background subtracted polarization curves in the positive sweep for different rotation rates demonstrate that in the potential region $< 0.8\,V_{RHE}$, diffusion limited reduction of peroxide occurs ($-i_{dl}$) whereas more positive than $1.0\,V_{RHE}$, the diffusion limited oxidation current (i_{dl}) is measured, which is of the same magnitude as the reduction current, see figure 5.3-3. Focusing on the region where the reduction shifts to the oxidation, i.e. between 0.8 and $1.0\,V_{RHE}$, it can be shown that also in this potential region both processes are diffusion limited. As demonstrated in the inset of figure 5.3-3, where the curves have been normalized to the diffusion limited current at $0.7\,V_{RHE}$, the curves all coincide, although measured with different peroxide concentration and rotation rates. This indicates that the peroxide reaction is no redox-process and that no kinetic information can be extracted from the curves. The potential of zero current (E_z) corresponds to equal oxidation and reduction reaction rates.

5.3.3 Oxide stripping

Apparently, while performing conventional CV, the oxide coverage is not at equilibrium. Decreasing the scan rate to very low values ($< 10\,mV\,s^{-1}$) is not feasible as the measured signal from surface reactions would be both very small and easily be subject to artefacts. Therefore, in order to study the surface oxidation state at equilibrium conditions, a stripping technique is more adequate. By firstly performing chronoamperometry at deposition potentials (E_d) in the oxide potential region for a long enough time period (potential hold of 100s), the equilibrium oxide coverage is reached. The following linear sweep voltammetry (LSV), starting at E_d towards more negative potentials gives a dynamic response to the equilibrium properties of the oxide. We denote this as stripping linear sweep voltammetry (sLSV) in contrast to normal LSV, which has not been preceded by chronoamperometry, and is followed by the subsequent positive going sweep, pLSV.
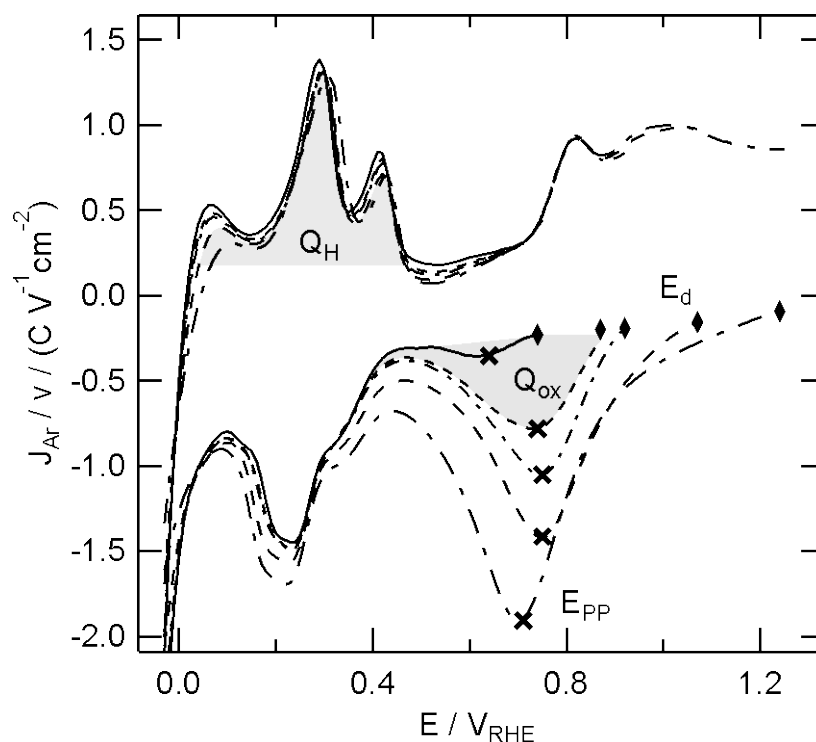
Figure 5.3-4   shows the sLSV and the subsequent pLVS of PC Pt for different deposition potentials recorded at 500mV/s in argon saturated 0.1 M KOH solution. For a better comparison the currents in the plot are normalized to the scan rate and the Pt surface area. Key features have been highlighted: charge integration of the oxide peak (Q_{ox}) and H_{upd} features (Q_H) as well as the oxide peak position (E_{pp}).

The results of the stripping procedure performed on PC Pt in Argon saturated solution are shown in figure 5.3-4. The voltammograms are all recorded at a scan rate of 500 mV s^{-1}. As can be seen the magnitude of the oxide reduction peak, its integrated area (Q_{ox}), as well as its peak potential (E_{pp}) change as a function of the deposition potential E_d, which is in agreement with investigations performed in acid solution [62]. In contrast to the oxide reduction, the total charge determined from integrating the H_{upd} peaks (Q_H) is unchanged indicating reversible behaviour. Interestingly, for a wide range of deposition potentials ($E_d = 0.93 - 1.08$ V$_{RHE}$) the peak potential E_{pp} of the consecutive sLVS reduction curves stays constant (see also figure 5.4-1) indicating a special significance of these two potential values.
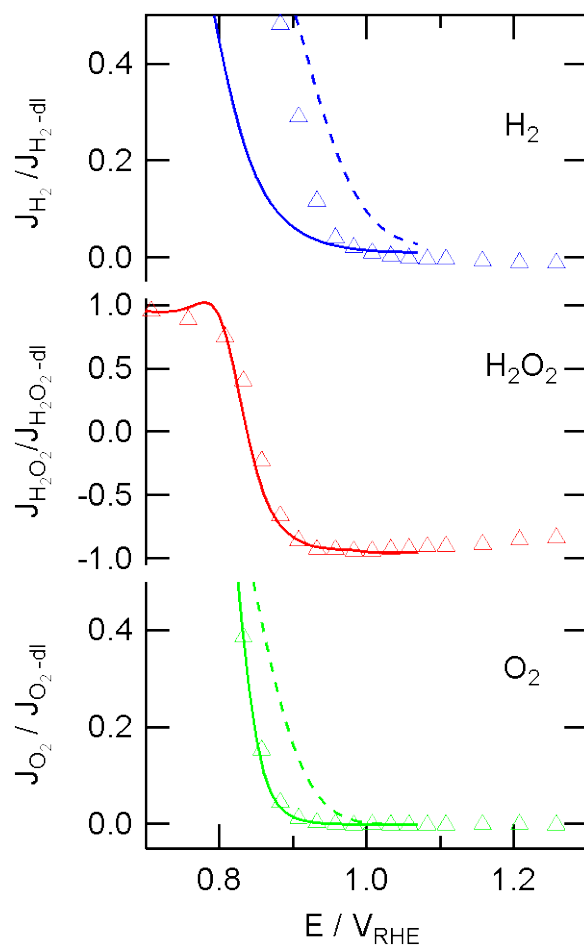
Figure 5.3-5 The influence of the technique on the measured reaction rate of the HOR (blue), the peroxide reaction (red), and the ORR (green); sLVS after potential hold at 1.08 V_{RHE} (solid lines) and concomitant pLSV curves (dashed lines) are plotted together with the current recorded after chronoamperometry (Δ), i.e. the current after a potential hold of 100 s at different potentials. The rotation rate was 1600 rpm, the scan rate of the LSV 500 mVs^{-1}. For better comparison, all currents have been normalised to the respective diffusion limited current.

In order to investigate the influence of oxide formation on the PC Pt surface on its catalytic activity, the HOR and ORR were probed under the same stripping procedure as applied for the argon saturated solution, but in electrolyte solutions saturated with H_2, O_2 instead. Furthermore, the same measurements were performed with hydrogen peroxide added to Ar saturated solution. The results are summarized in figure 5.3-5:

for each reaction three curves are shown, i.e. the sLVS polarization curve (solid lines) after potential hold at 1.08 V_{RHE}, the consecutive pLVS curve (dashed lines), and the current values after potential holds at different potentials for 100 s (chronoamperometry, triangles). In order to simplify their comparison all currents have been normalised to the diffusion limited current of the respective reaction.

At potentials below 0.76 V_{RHE} (not shown) the potential hold does not influence the polarization curves, i.e. the currents of pLSV, sLSV and chronoamperometry all coincide. Thus in KOH solution below 0.76 V_{RHE} no blocking species are adsorbed on the Pt surface. At more positive potentials, however, the potential hold does significantly influence the observed polarization curves indicating the onset of oxide formation. As can be seen, the normalized sLSV polarization curves after the potential hold and the consecutive positive going pLSV scans do not coincide for any of the three reactions, i.e. O_2, H_2, and HO_2^- in line with the previous observation that oxide formation is not an instantaneous process. Notice further, that for the O_2 and HO_2^- reaction the sLSV curves coincide with the chronoamperometric values, whereas for the H_2 oxidation they do not. In addition, the sLSV polarization curves of the O_2 and HO_2^- reaction exhibit the same potential dependency, again, in contrast to the H_2 oxidation reaction. These findings indicate a significant difference between the ORR and peroxide reaction and the HOR. As discussed later in more detail, the difference is that in the O_2 and HO_2^- reaction OH_{ad} is a reaction intermediate, whereas it is not in the HOR.

Additional insight into the influence of the potential prehistory on the reaction dynamics can be obtained by comparing for different deposition potentials E_d of oxide species the half-wave potentials (E_{HW}) of the consecutive polarization curves for the O_2 and H_2 reactions in addition to the potential at zero current (E_z) for the HO_2^- reaction. Given that surface oxides can influence the reaction rate and that oxide formation is not an instantaneous process, the E_{HW} and E_z values obtained in sLSV and the subsequent pLSV can be used as indicators of the oxide state of the surface at the potential E_d.

126
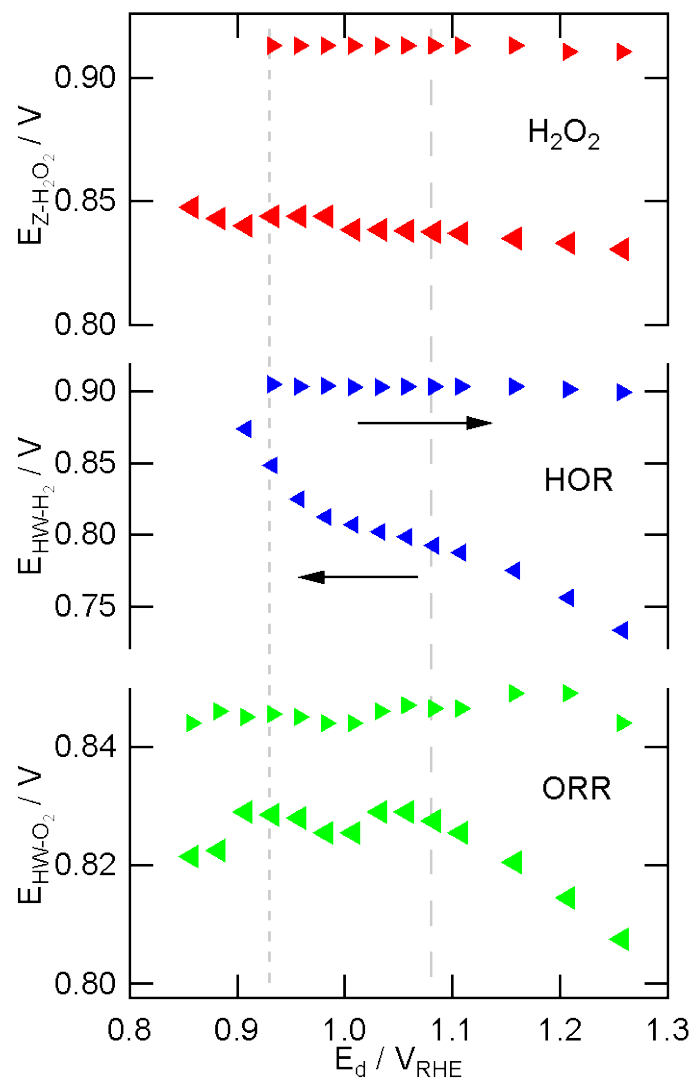
Figure 5.3-6   **Halfwave potentials of HOR and ORR polarization curves as well as the zero crossing potential of HO$_2^-$ as a function of hold potential E$_d$ for sLSV (◄) and subsequent pLSV (►). The gray lines correspond to the proposed potentials of OH and O, respectively, monolayer formation.**

Such plots are shown in figure 5.3-6. It is demonstrated that for all pLSV curves E$_{HW}$ is independent more or less of the deposition potential E$_d$. In other words, the positive going polarization curves of the HOR and ORR are not affected by a previous potential hold. This is actually the reason why in most ORR investigations only the positive going polarization curves are evaluated. Because in contrast, the E$_{HW}$ values of the sLSV curves exhibit a distinctive dependence on the deposition potential. Especially the HOR is highly sensitive to potential holds above 0.93 V$_{RHE}$. The

difference in the half-way potentials of the sLSV and the constant pLVS polarization curves increases with increasing oxide deposition potential. For the ORR, the half-way potentials of the sLSV and pLVS polarization curves do not coincide either, even though a different behaviour is seen. Two potential regions can be distinguished. For deposition potentials between 0.93 and 1.08 V_{RHE} the difference in E_{HW} between the sLSV and pLVS curves is more or less constant, while for E_d values above 1.08 V_{RHE}, E_{HW} decreases in the sLSV curves (and stays constant in the pLSV curves).

In the case of the peroxide reaction, it is seen that the potential of equal peroxide reduction and oxidation rates E_z is different for the pLSV and sLSV curves, however, independent of the chosen E_d.

5.4 Discussion

The presented results clearly indicate that the prehistory of Pt considerably influences the observed reaction rates. In the following the findings will be compared to each other and interpreted.

5.4.1 Hysteresis

Based on the CVs recorded in Ar saturated solution, it is seen that the initial oxidation of the Pt surface is a fast process; no peak shifts are noticeable for the oxidation/reduction process even at scan rates as high as 10 V/s in contrast to the H_{upd} process (see figure 5.3-1). The surface oxidation peak at 0.8 V exhibits reversible behaviour although the peak area decreases with the scan rate. However, once the system prolonged for 100 s at high potentials, the reduction peaks in the concomitant sLSV curves shift significantly (70 mV) towards more negative potentials; even at moderate deposition voltages (see figure 5.3-4).

The probed catalytic reactions show an analogue behaviour. A noticeable dissimilarity can be observed comparing positive and negative scan directions of the polarization curves for the HOR, ORR and peroxide reactions (figure 5.1-1). Although the scan rate has only a small influence on the blockage of the HOR in the positive potential sweep, the hysteresis between negative and positive going polarization curve increases with decreasing the scan rate (figure 5.3-2). Using the stripping procedure and comparing sLSV to pLSV the described effect becomes even more evident (figure 5.3-5 and figure 5.3-6).

5.4.2 H_2 as a probe molecule for the equilibrium oxide coverage

The decrease in the HOR rate on Pt at high potentials is demonstrated in figure 5.1-1. Bao et al. recently interpreted this decrease as a decline in the tunnelling current through a growing isolating oxide layer [63]. However, considering that the HOR is a catalytic reaction and not a Helmholtz reaction, the probing capability of the oxide thickness by the HOR is questionable. Instead, the decrease in the HOR rate can be interpreted as a decrease in available active sites due to blockage of the Pt surface by adsorbed oxygenated species [66]. Hence, the absence of any HOR current indicates a completely blocked surface. This state is reached at a potential of 1.08 V_{RHE}.

The microscopic information provided by the potential dependence of the HOR is however limited. A direct correlation of the measured current to the number of free sites cannot be extracted without the knowledge of the exact oxide growth formation. Such a model is lacking so far. However, a partially blocked surface exhibits a reduced apparent activity regardless of whether the active spots are macro- or microscopic [67]. Assuming that the growth and the reduction of an oxide layer on Pt follow the same mechanism, the half wave potential of different LSV curves corresponds to the same oxide coverage, although the exact value is unknown. The potential difference between the sLSV and pLSV curves therefore displays the difference in available active sites for the reactions.

So far no single electrochemical experiment can determine the equilibrium oxide coverage of PC Pt at a certain potential. However, by combining different methods a clearer picture can be revealed. During a regular CV, the surface state is not at equilibrium, which is obvious from figure 5.3-1 and figure 5.3-2, i.e. the scan rate has a large influence on the current response. For that reason, an adequate analysis can only be given by applying a stripping technique. The key values obtained from these experiments have been summarized in figure 5.4-1.
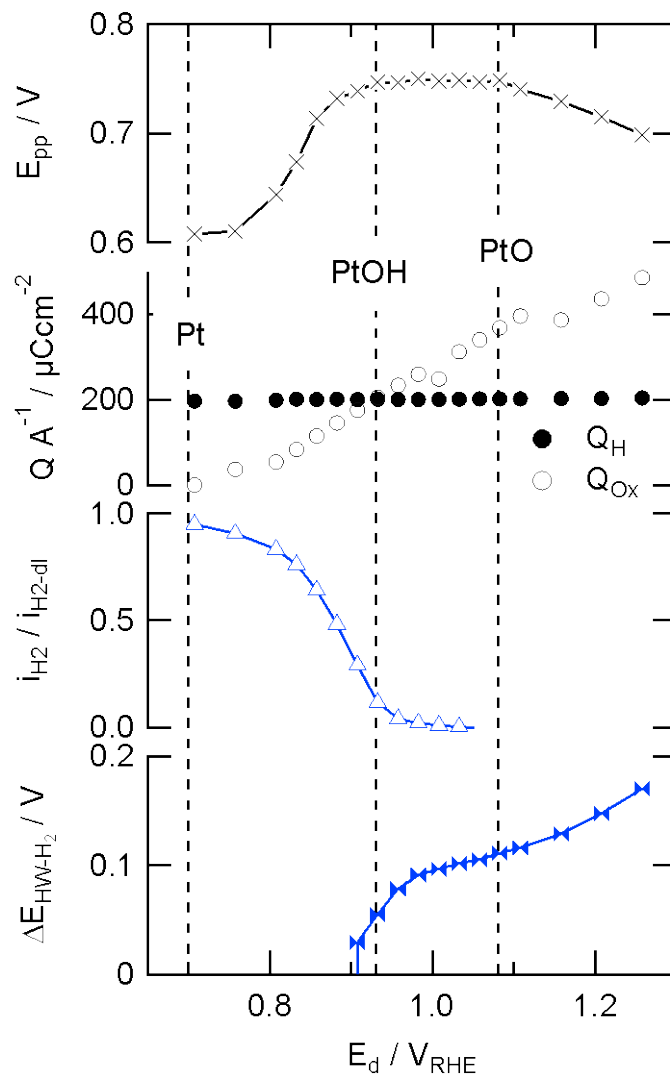
Figure 5.4-1 The peak potential E_{pp} of oxide reduction observed in LSV recorded in Ar saturated electrolyte is compared to the calculated stripping charge of adsorb oxygenated species and H_{upd} obtained in the same measurement as well as to the normalized steady-state HOR current and the difference between the halfwave potentials of sLSV and pLSV measurements in H_2 saturated solution. All values are shown as a function of the deposition potential E_d.

Based on the comparison of the results obtained from different techniques, the equilibrium coverage of oxygenated species on the platinum surface can be divided into 4 potential regions. Focusing firstly on the region above 1.08 V_{RHE}, no HOR rate is measured in this potential region indicating the complete blockage of all Pt sites by

an oxide species. The negative shift of the E_{pp} as the potential increases is a strong indication that a second oxide layer starts to form onto the first monolayer [68]. The stripping charge of the oxide layer increases continuously with E_d and specificly at 1.08 V_{RHE}, a ratio of 2:1 compared to the area under the H_{upd} peaks is found. It can therefore be deduced that PtO is formed, reaching monolayer coverage at 1.08 V_{RHE}. At a more positive potentials multilayers are formed.

Similar findings have been reported using other techniques. Electrochemical quartz-crystal nanoblance EQCN experiments have shown an increase of 16 g/mol e$^-$ in the oxide region [69-70]. The onset of a more stable oxide was also identified by the change of signal stability of the oxide upon exposure to an electron beam [69] as well as clear change of surface morphology of Pt [111] using in situ STM [71].

The nature of the equilibrium oxide layer formed at lower potentials is, however, more intriguing. No stripping peak can be observed for $E_d < 0.7$ V_{RHE}, i.e. the surface is oxide free in this region. At more positive potentials, the stripping charge increases, the peak stripping peak position shifts more positive and the steady state current of the HOR decreases. In particular at $E_d = 0.93$ V_{RHE}, Q_{ox} becomes equivalent to Q_{Hupd} and the HOR reaction is almost totally inhibited. At the same time for $E_d = [0.93-1.08 V_{RHE}]$ E_{pp} is constant. Independent of whether the HOR requires one or two Pt atoms as active site, the blockage exceeds that expected from a PtO species, i.e. a coverage of 50 % based on Q_{ox} [72]. Thus the results are interpreted such that the observed stripping charge is due to the adsorption of OH, which forms a monolayer at 0.93V. Between 0.93-1.08 V_{RHE} PtOH gradual transforms into PtO.

This transition can also be monitored by the difference between the HOR half wave potential in pLSV and sLSV curves (ΔE_{HW-H2}, see figure 5.4-1). At a PtOH surface coverage of ~80% a difference is measurable. At higher potentials the divergence rapidly increases to reach a plateau a mixed coverage of PtO and PtOH. At more potentials where PtO multilayers are formed the difference continues to increase.

These potential regions fit well to results published by Wakisaka et al. They did potential hold experiments on Pt(111) and PC Pt in HF solution with subsequent X-ray photoelectron spectroscopy in a vacuum chamber [73]. Adsorbed species with different bonding energies were ascribed to OH_{ads} and O_{ads}. Their occurrence on the surface was plotted as a function of potential for both Pt(111) and PC Pt surface. The interpretation of which species predominates at what potential corresponds very well

to those proposed for the Pt(111) surface, although a little less to the PC Pt surface, for which an equal adsorption of OH_{ads} and O_{ads} starting at 0.8 V_{RHE} was proposed. This disagreement could be attributed to the fact that in the current study real in-situ investigations were performed and no emersion of the sample out of the electrolyte is necessary like in vacuum studies. Furthermore, the different preparation method of our sample, i.e. CO annealing, is known to reduce surface defects [39].

The results can be summarized in the following red-ox couples:

EC1 $\qquad\qquad\qquad Pt + OH^- \rightleftarrows PtOH + e^- \qquad\qquad$ $E_{1/2}$=0.83 V_{RHE}

EC2 $\qquad\qquad\qquad PtOH \rightleftarrows PtO + H^+ + e^- \qquad\qquad$ $E_{1/2}$=1.01 V_{RHE}
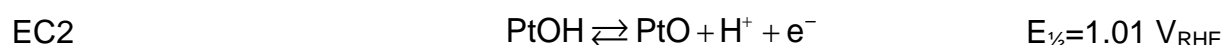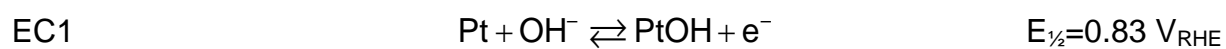
Where $E_{1/2}$ is defined as the potential of a 50% covered PC Pt surface. Note how well the $E_{1/2}$ of EC1 corresponds to the oxide peaks of the CV in figure 5.3-1. The two reactions are compatible with the observation that oxide features for PC Pt appear at the same potential (vs RHE) whether recorded in alkaline or acid solution [74]. In that respect, EC1 is quasi stable intermediate to the full oxidised state of PtO.

$$Pt + H_2O \rightarrow PtO + 2H^+ + e^- \qquad\qquad E_0\text{=}0.98\ V_{RHE}\text{[75]}$$
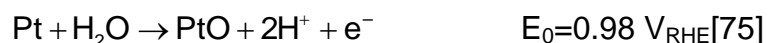
Furthermore, a negative shift of the oxide reduction peak of about 70mV between CV and sLSV can also be observed (see figure 5.3-1 and figure 5.4-1). This can be interpreted in terms that the oxide becomes stabilized given that the system is given enough time to reach equilibrium conditions. Weaver et al. studied the oxide coverage of Pt(111) in vacuum [76]. They proposed that although O_{ad} had a repelling interaction at low coverage, once the oxide coverage exceeded 0.75 ML, the growth of platinum oxide commenced which is energetically more stable than chemisorbed atoms. The peak shift could therefore be due to a similar phase transition of the oxide.

5.4.3 Pt surface oxide under steady state conditions

The reaction pathways of the catalytic ORR and HO_2^- reduction include surface oxide intermediates, thus the surface oxide coverage cannot be considered to be at equilibrium. Indeed, comparing the J-E-characteristics of the different EC techniques used in this work, a different behaviour of these two reactions compared to HOR is observed. As discussed in the previous chapter in figure 5.3-5 it can be seen that for both ORR and HO_2^-, the chronoamperometry curve and that of sLSV measurements

starting from 1.08 V_{RHE} coincide, in contrast to what is found for the HOR. This is more explicitly shown in figure 5.3-6 as E_{HW-O2} and E_z of sLSV are independent of E_d < 1.08 V_{RHE}, in contrast to E_{HW-H2}. Hence, it can be deduce that during the ORR and HO_2^- reaction, PtO is formed at potentials lower than the potential where it is formed from PtOH.

5.4.3.1 HO_2^-

Peroxide is a metastable molecule and in the potential range, where the measured current changes from oxidation to reduction, both reactions are thermodynamically feasible [77]. Interestingly, the results demonstrate that the reaction activity, whether oxidation or reduction, is always diffusion limited even in the mixed region where both reactions occur (see figure 5.3-3). The measured current is therefore the net rate of molecules being oxidized and reduced. Zero current indicates that both rates are identical, i.e. only electroless decomposition of peroxide to oxygen and water occurs.

It is therefore concluded that in the vicinity of PC Pt peroxide is not stable at any potential. The current magnitude and sign change of the net catalytic reaction should therefore be related to the rate difference between oxidative generation and reductive disintegration of surface oxides. This interpretation is supported by the correspondence of E_z in the sLSV curves, i.e. 0.84 V_{RHE} (see figure 5.3-6), to the value of $E_{1/2}$ in equation EC1. Furthermore, in contrast to the ORR and HOR even high deposition potentials do not affect E_z. This implies that during the peroxide reaction, no PtO multilayers are formed, hence PtO is consumed in reaction (C2). Diffusion limited oxidation currents are already reached at 0.93 V_{RHE}. Hence, also OH_{ad} is removed in the reaction scheme (EC3).

From these observations, the following fundametal reactions are proposed which can explain the observed currents at all potentials:

C1 $\qquad\qquad Pt + HO_2^- \rightarrow PtO + OH^-$

C2 $\qquad\qquad PtO + HO_2^- \rightarrow Pt + O_2 + OH^-$

EC1 $\qquad\qquad Pt + OH^- \rightleftarrows PtOH + e^- \qquad\qquad E_{1/2}=0.83\ V_{RHE}$

EC2 $\qquad\qquad PtOH \rightleftarrows PtO + H^+ + e^- \qquad\qquad E_{1/2}=1.01\ V_{RHE}$

EC3 $\qquad\qquad PtOH + O_2H^- \rightarrow Pt + O_2 + H_2O + e^-$
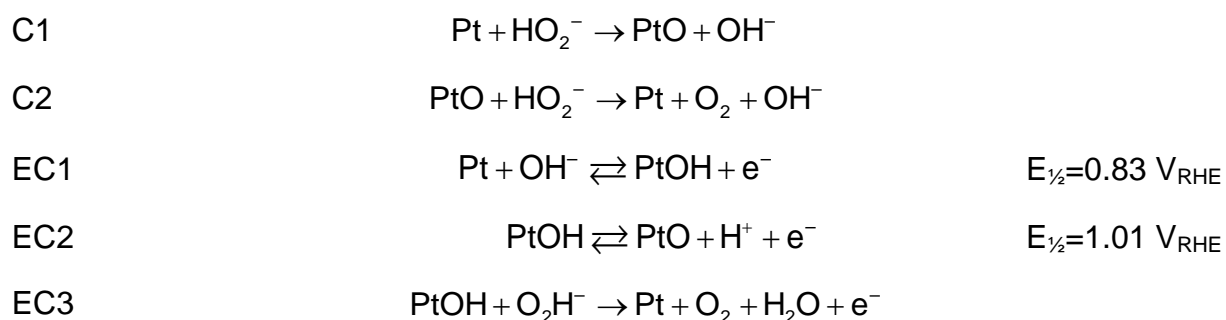
The observed reduction current at potentials E< 0.84 V_{RHE}, is dominated by reactions C1, EC1 and EC2. In the potential range between 0.84 and 1.01 V_{RHE} the observed net oxidation current is given due to reactions EC3 and EC1. At more positive, where PtO starts to be the dominating adsorbed surface species, the oxidation current is due to reactions EC1, EC2, and C2. Peroxide decomposition can be expressed by EC3, EC2 and C1 or by C1 and C2.

5.4.3.2 ORR

As discussed in the previous chapter the overpotential of the ORR on Pt is often correlated to the blocking effect of oxygenated species adsorbed on the surface. These species can originate either from water or from the reactant O_2 and inhibit further oxygen reduction as no free Pt sites are regenerated.

As demonstrated in figure 5.3-5, in a positive going potential sweep at 0.5 Vs^{-1} no ORR activity is detected on Pt above 1.0 V_{RHE}. During such a condition the system is not at steady state. At steady-state conditions ORR activity is observed only below 0.93 V_{RHE}, in analogue with the HOR. Bearing in mind the potential regions of the different surface species from the previous discussion, the ORR only occurs as the surface coverage of oxygenated species becomes less than a monolayer.

Moreover, if multilayer of PtO was formed (E_d > 1.08 V_{RHE}), the half-wave potential of sLSV is negatively shifted (see figure 5.3-6). This indicates that during the sLSV the PtO film temporarily resides on the surface also at more negative potentials and blocks active sites.

Associative pathway

Comparing the peroxide reaction with the ORR as demonstrated in figure 5.3-5, it can be seen that the activity increase of the ORR occurs in the same potential region where the net oxidation of peroxide gradually turns into a net reduction.

Based on these results, the proposed reaction pathway for the reduction of O_2 can be expressed by the reaction EC3, and the reduction of peroxide, i.e. the reactions C1, EC2 and EC1. That is, O_2 is first reduced to peroxide at bare Pt sites. As the peroxide is not stable, the reaction can either proceed back to O_2 or peroxide is reduce further to water and thereby regenerate a free Pt site.

EC3 $\qquad\qquad PtOH + O_2H^- \rightarrow Pt + O_2 + H_2O + e^-$

| C1 | $Pt + HO_2^- \rightarrow PtO + OH^-$ | |

| EC2 | $PtOH \rightleftarrows PtO + H^+ + e^-$ | $E_{1/2} = 1.01\ V_{RHE}$ |

| EC1 | $Pt + OH^- \rightleftarrows PtOH + e^-$ | $E_{1/2} = 0.83\ V_{RHE}$ |
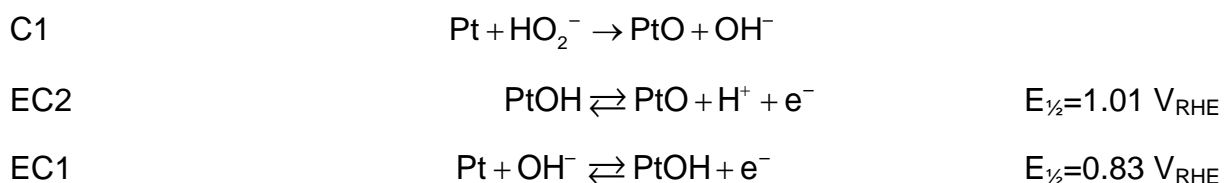
The potential dependency of the measured reduction current is therefore dictated by reaction EC1, which requires the most negative potential for a reduction.

Dissociative pathway

An alternative pathway can be considered, where the first step is given by the dissociative adsorption of O_2 (C3). The following steps are the reduction of the PtO to water by reaction EC2 and EC1.

| C3 | $2Pt + O_2 \rightarrow 2PtO$ | |

| EC2 | $PtOH \rightleftarrows PtO + H^+ + e^-$ | $E_{1/2} = 1.01\ V_{RHE}$ |

| EC1 | $Pt + OH^- \rightleftarrows PtOH + e^-$ | $E_{1/2} = 0.83\ V_{RHE}$ |
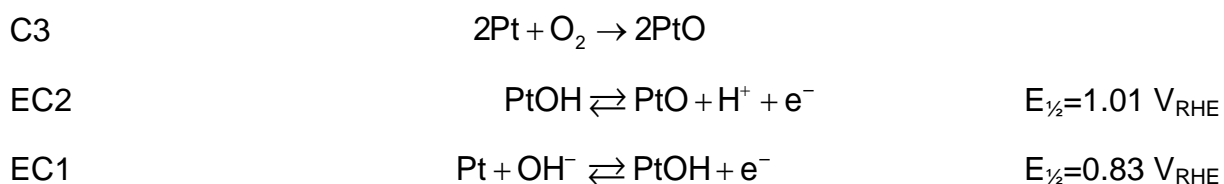
Also in this case EC1 dictates the onset of the measured reduction current. It is therefore not possible from the conducted measurements to distinguish which pathway is the dominating one.

5.5 Conclusion

In this chapter the role of surface oxides on the kinetics of the oxygen reduction reaction, the oxidation/reduction of peroxide and the hydrogen oxidation reaction is studied on PC Pt in alkaline solution.

The results indicate that in alkaline solution, the initial surface oxidation of Pt is a significantly faster reaction than the H_{upd} process. This behaviour, which has not been previously reported, becomes evident in the CVs normalized to the scan rate. While the H_{upd} peaks clearly shift with increasing scan rate, the peak potential of the oxidation peak around 0.8 V_{RHE} exhibits a reversible behaviour up to extremely high scan rates. The peak area, however, is sensitive to the applied scan rate which indicates that the equilibrium coverage is not reached instantaneously. Furthermore, a noticeable dissimilarity can be observed comparing positive and negative scan directions of a polarisation curve of the HOR, ORR and peroxide reactions. Although the scan rate has only a small influence on the blockage of the HOR in a positive sweep, the hysteresis between positive and negative going sweeps increases at

smaller scan rates. Hence, in order to study the correlation between the surface oxidation and catalytic reactions under steady-state conditions, a stripping procedure was used.

By correlating the results from the stripping procedure in Ar and H_2 saturated solution the potential regions where at equilibrium conditions the different oxide species are predominant on the Pt surface could be deduced. The onset of adsorbed oxide species is established at 0.7 V_{RHE} and at 0.93 V_{RHE} the formation of a monolayer of PtOH is completed. Above 0.93 V_{RHE} PtOH transforms into PtO, which completes a monolayer at 1.08 V_{RHE}. At even higher potentials PtO multilayers are formed. PtOH can thus be considered to be an intermediate of PtO.

The same experimental procedure was used to study ORR and HO_2^- at steady-state conditions. It could be shown that at steady-state conditions the decisive reaction of both the reduction of HO_2^- and oxygen is the reduction of PtOH. Furthermore, during these reactions PtO is formed at a potential more negative than the oxidation of PtOH. As the reduction and oxidation of HO_2^- on PC Pt is always diffusion limited it was not possible to distinguish between the two possible reaction pathways of the ORR, the associative and dissociative mechanism.

6 Silver nanoparticles

6.1 Introduction

In order to reduce the costs of fuel cells replacing Pt based catalysts for the oxygen reduction reaction by cheaper materials not containing any precious metals is a strategy pursuit by several research groups. A fundamental difficulty in reaching this goal, however, is how to make a reasonable comparison of the activity of different catalyst classes. The state-of-the-art catalyst in fuel cells consists of nanoparticles platinum dispersed on a conductive chemical inert carbon substrate. Such a catalyst has a significant surface to volume ratio and is more complex to study in comparison to investigations on a flat electrode as introduced in the previous chapter. The active surface area of the catalyst does not correspond to the geometric area, but is proportional to the catalyst mass and the particle size. There are also more practical issues concerning the samples. Loading effects such as activity saturation can be expected for too high loadings. If the diffusion of the reactant is not fast enough, some particles within the catalyst will be inaccessible and thus be inactive as the reactant concentration is zero.

The lack of a common methodology and benchmark activities for the study of platinum high surface area catalysts is pointed out in the review by Gasteiger et al. [5]. The differences of the presented activity results of Pt based catalysts, regardless of being extracted from RDE measurements or membrane electrode assembly (MEA) experiments, is a strong indicator of the relevance of this issue. The importance of benchmark activities and thereby the necessity of a common methodology in catalyst characterization cannot be enough emphasized. If the characteristic properties of a system cannot be reproduced by other research groups, how to make a rational comparison to other systems?

In order to address this issue, Mayrhofer et al. recently proposed a set of practical guidelines [35]. These target the characterization of platinum based catalyst using the RDE. In short, they point out the importance of active sites determination using, in which potential region reasonable measured quantities can be extracted as well as loading effect should be investigated. The guidelines are written with respect to platinum but can be generalized to cover also non-platinum catalysts.

As discussed in the previous chapters, one fundamental problem in the comparison of different catalysts is the definition and determination of the ECA used to evaluate the specific activity ($J_{k:ECA}$); the meaning of real surface area depends on the method of measurement, on the theory of this method, and on the conditions of application of the method [78]. For Pt based catalysts, the ECA is usually determined by the stripping charge of underpotential-deposited hydrogen (H_{upd}) or more accurately by the oxidation of an adsorbed CO monolayer. Both methods assume a one to one ratio of the adsorbates and Pt surface atoms [22]. Furthermore, based on single crystal data by some groups an average number of surface atoms is assumed for polycrystalline Pt equalling a charge value of 210 µC cm^{-1}. The experimental determination of this charge after flame annealing, however, led to an average value of 195 µC cm^{-2} [35].

By comparsion, for non-platinum metal catalysts these rather straightforward methods are in general not feasible. A range of possible alternatives has been reviewed by Trasatti and Petrii [78], suggesting for example under potential deposition (upd) of foreign metals for metal nanoparticles systems. The methodology of metal upd for the ECA determination has already been successfully applied by Green and Kucernak [79] in the case Cu_{upd} on PtRu alloy catalyst. For Ag based catalysts, Pb_{upd} [68] as well as Tl_{upd} [80] are feasible options, both yielding corresponding results.

The scope of this part of the thesis was to thoroughly characterise silver based electrocatalysts for the ORR in alkaline electrolyte. Extending the guidelines for the activity determination by the thin-film RDE technique of Pt based catalysts [35] and applying an active compensation of the solution resistance. In this thesis a silver nanoparticle catalyst and polycrystalline (PC) Ag are characterised in 0.1 M KOH solution. For the determination of the number of electrochemical accessible surface sites an underpotentially deposited lead monolayer is stripped of the catalyst in a linear potential sweep. The obtained results of the ORR activity are compared to those of PC Pt measured in the same electrolyte as well as literature values. Although, nano particlulate silver catalysts and also silver based alloys have been investigated in previous studies, the results could not be compared to benchmark values of platinum due the dissimilar methodologies [30, 81-82].

6.2 Experimental details

The electrolyte solutions: 0.1 M KOH and 0.1 M KOH + 125 µM Pb(NO$_3$)$_2$ were prepared using Millipore water (resistivity = 18.2 MΩ cm^{-1}, TOC < 5 ppb), KOH pellets (Merck, Suprapure) and Lead(II)nitrate salt (Merck, analytical grade). During measurements, the electrolyte was saturated with either argon or oxygen (Airgas, purity grade 5.0). A standard calomel electrode (SCE) was employed as a reference electrode. However, the reversible potential of hydrogen oxidation/reduction was determined for each measurement, and all presented data are given with respect to the reversible hydrogen electrode (RHE). The working electrodes used are Ag, Pt and glassy carbon (GC) discs (each Ø = 5 mm, A = 0.196 cm^2), the sides coated with epoxy-resin (to minimise parasitic currents) and mounted into Teflon RDE tips. The glassy carbon disc was cleaned by polishing, placing into a sonic cleaner and finally placing it for 5 min into concentrated perchloric acid.

Prior to each measurement the solution resistance [12] from the working electrode to the Luggin capillary was determined using an AC signal (5 kHz, 5 mV), and thereafter electronically compensated for by a positive feedback scheme. In our setup, the typical R$_{sol}$ was around 10 Ω; however, in some cases values above 20 Ω were determined, which have a large effect if no compensation scheme is used. The CV and ORR measurements in 0.1 M KOH were conducted in the Pb free cell, prior to the surface area determination per formed in a separate cell, thus preventing any Pb contamination that could affect the activity measurements.

6.2.1 Catalyst samples

The silver catalyst provided in powder form by Umicore AG & Co. KG, has an average particle size of about 100 nm. It was suspended in Millipore water, dispersed by a 2 s-insertion into an ultra sonic cleaner and thereafter kept on rotation by a magnetic stirrer. An aluminium foil covered the glassware in order to protect the silver catalyst from light. By these measures, agglomeration of the particles was reduced and the upper limit of the catalyst solution lifetime was 1 week; however, by keeping the solution longer in the sonic cleaner or unprotected from light, a visible degradation appeared already after a few hours.

The catalyst layers were prepared by pipetting 20–40 µl catalyst solution onto an electrochemically oxidised GC disc (100 mA for 5 min in 2 electrode setup).

Thereafter the electrode tip was put in a light sheltered dryer under N_2-atmosphere. Due to the hydrophilic nature of the oxidised GC reproducible smooth catalyst layers could be produced without the usage of any additives, furthermore the oxidation also enhances the sticking of the silver particles onto the GC [83-84].

In order to exemplify the difference between a successful sample preparation compared to an unsuccessful one, 2 different examples are shown in figure 6.2-1. A clear difference can be seen. The "good" sample has a faint homogenous nuance of gray on the dark black substrate. In contrast, the "bad" sample exhibits strong greyish patterns of darker and lighter areas. A scanning electron microscope (SEM) image of the sample (magnification 3.500x) demonstrates that these gray patterns are agglomerated particles.
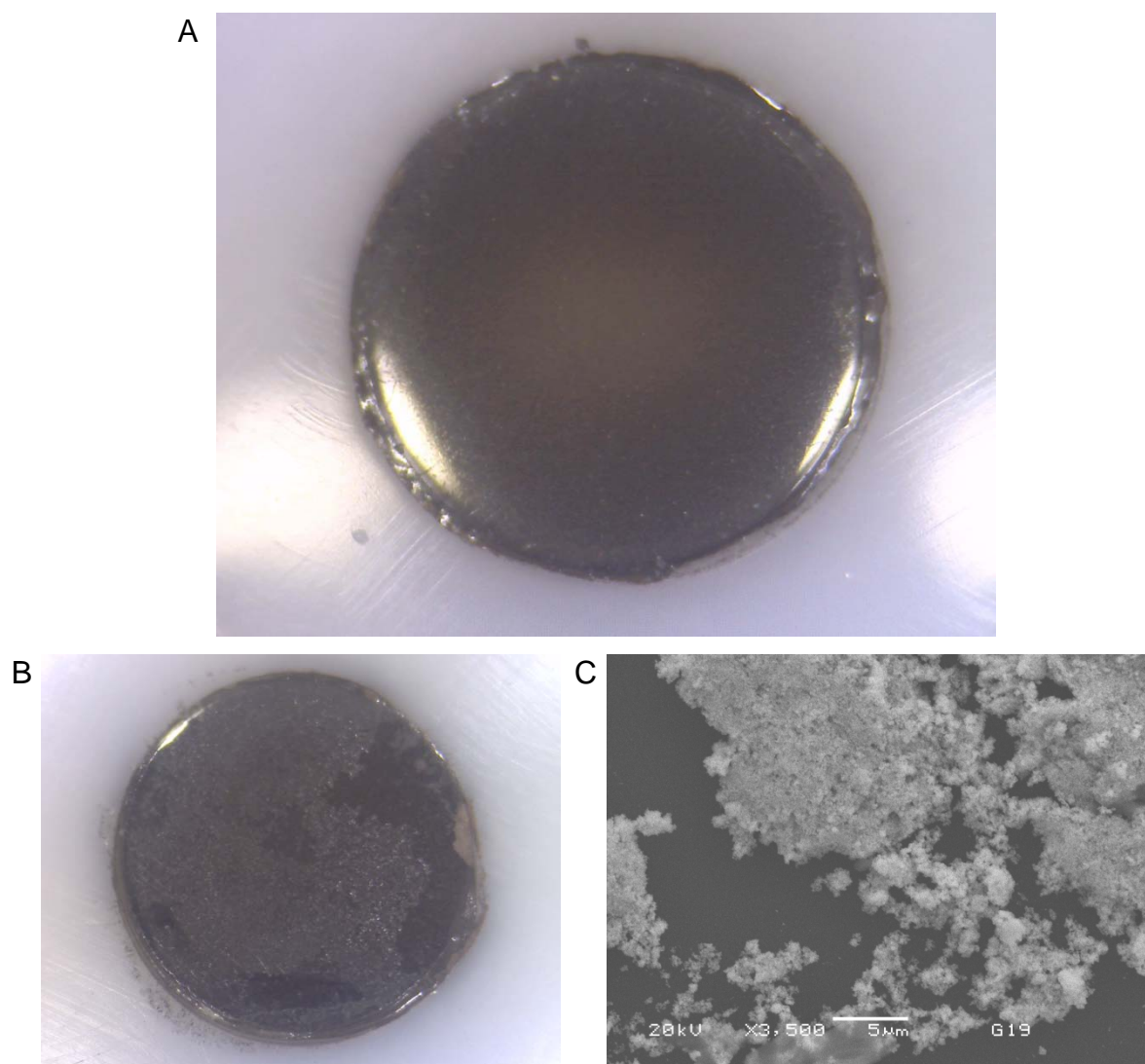
Figure 6.2-1: **Glassy carbon disk electrodes modified by silver particles: A) successful sample, B) abortive sample showing gray patterns.**

C) SEM image of the gray patterns show that they consist of agglomerated particles.

6.3 Results and discussion

Prior to the ORR and surface site determination measurements, the catalyst samples were characterised by cyclic voltammetry in Ar saturated solution. A typical voltammogram is shown in figure 6.3-1.
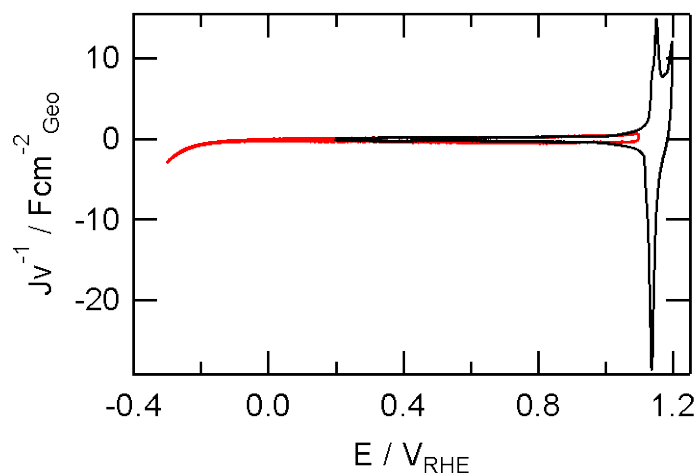
Figure 6.3-1:   Cyclic voltammograms of poly crystalline silver in 0.1 M KOH.

NP Ag and PC Ag exhibit no specific features between 0 and 1.05 V_{RHE}, and mainly capacitive currents are observed in agreement with previous findings [85-87]. The hydrogen evolution reaction occurs at more negative potentials than $-0.3\,V_{RHE}$, whereas at potentials more positive than 1.05 V_{RHE}, large oxide features can be seen. Silver oxide is irreversibly formed, as indicated by a white staining of the PC Ag-electrode. This leads to a roughening of the surface [88-90]. In order to avoid any potential induced changes of the catalyst, the potential window was kept bellow 1.05 V_{RHE}.

6.3.1 Oxygen reduction activity

ORR measurements were conducted in a Pb free cell by recording polarisation curves in oxygen saturated 0.1 M KOH solution between -0.3 and 1.050 V_{RHE}, with active R_{sol}-compensation, see figure 6.3-2. Cycling below 0.0 V_{RHE} results in a considerable increase in the ORR activity, which is associated with the reduction of the Ag surface, as reported previously [8, 91]. The lower potential limit of $-0.3\,V_{RHE}$

was chosen since it leads to a maximised ORR activity of the Ag catalysts, while at the same time avoiding a major detachment of NP Ag from the GC electrode, which was observed at even lower potentials.
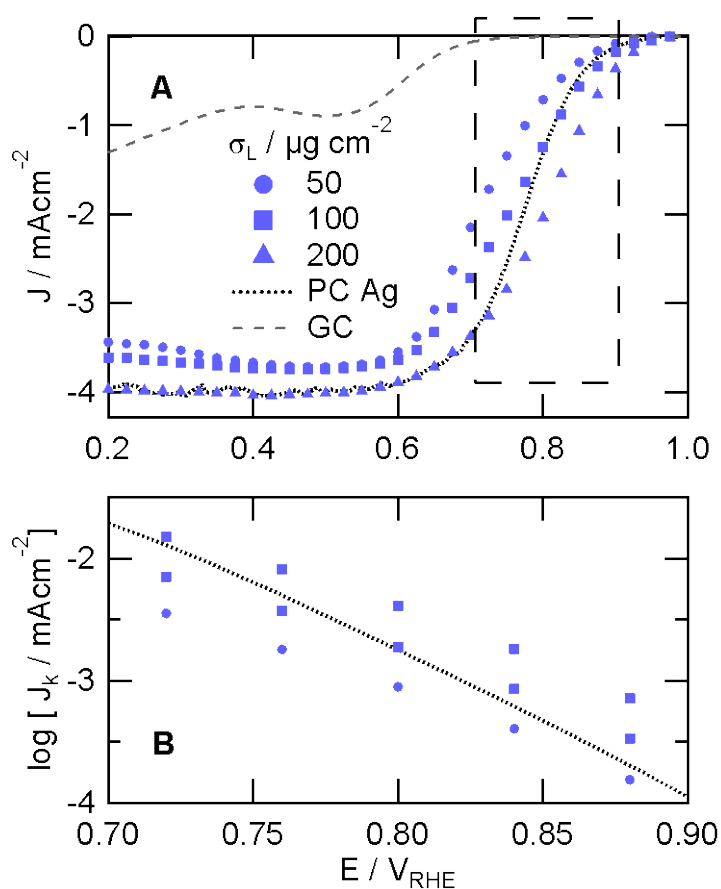
Figure 6.3-2: R_s-compensated and capacitive current corrected polarization curves recorded in oxygen saturated 0.1 M KOH solution at a rotation rate of 900 rpm for NP Ag with 50, 100 and 200 µCcm^{-2} loadings as well as PC Ag and bare GC. The scan rate was 0.1 Vs^{-1}. (B) Tafel plot of total kinetic current densities obtained from the polarization curves shown in (A).

In figure 6.3-2(A) the ORR polarisation curves of NP Ag at three different loadings are compared to the ones of PC Ag and bare GC. In contrast to Pt based catalysts no hysteresis is observed between the positive and negative going scans. In order to extract the faradaic current all polarisation curves are corrected for capacitive currents by subtracting the corresponding blank CV recorded in Ar saturated solution. From figure 6.3-2(A) it is discernable that GC has only a negligible influence on the

142

ORR polarisation curves of NP Ag, since no oxygen reduction occurs above 0.7 V_{RHE}. Furthermore, it can be observed that with increasing catalyst loading, the polarisation curves shift towards higher potentials as expected. This effect was utilised to adjust the potential region for the determination of the ORR activity to potentials relevant for FC applications. In the case of NP Ag, for instance, the kinetic current regime applying a loading of 200 µgcm^{-2} lies above 0.8 V_{RHE} and thus in the potential region of interest. At potentials below 0.6 V_{RHE} the current is limited by diffusion of oxygen towards the electrode surface, and no kinetic data of the oxygen reduction reaction were extracted.
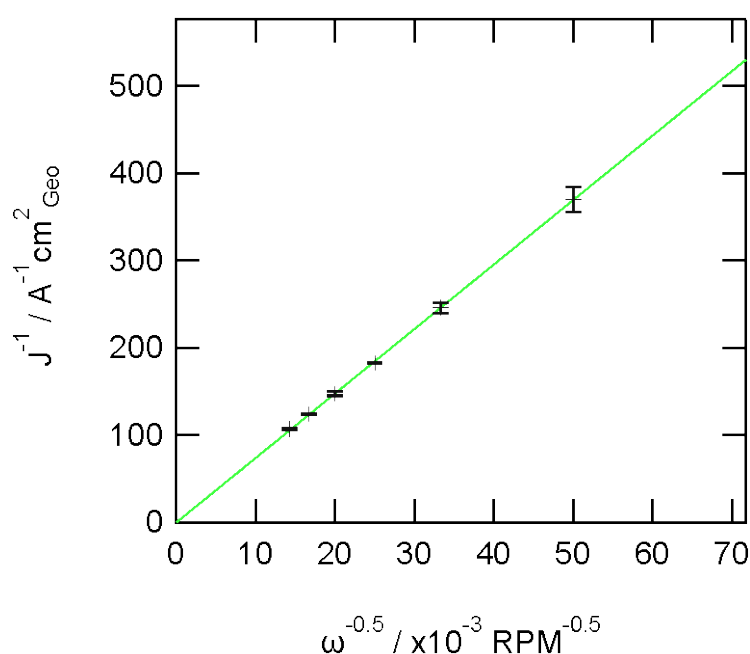
Figure 6.3-3: **Levich plot. The interception of the extrapolated with the origin shows that the current follows the Levich equation.**

The analysis of a Levich plot of J_{dl} at various electrode rotation rates (ω) (see figure 6.3-3) indicates that the current follows the Levich equation and no additional current limitation is active. Given the theoretical value of the diffusion limited current for a four electron process of 4.4 mA cm^{-2} at 900 rpm, calculated using the Levich equation and literature data; i.e. O2-solubility (1.2 × 10^{-6}mol cm^{-3}) [92], O2-diffusion-coefficient (2.0 × 10^{-5}cm s^{-2}) [92] and viscosity of the electrolyte (1.0 × 10^{-2}cm^{2}s^{-1}) [92]; the measured diffusion limited current obtained for a loading of 200 µgcm^{-2} as well as for PC Ag deviates less than 10% from the theoretical value in accordance to

the guidelines for Pt based catalysts [35]. For catalyst loadings of 50 and 100 µgcm^{-2} the diffusion limited currents deviate slightly more from the theoretical value, indicating an incomplete coverage of the GC with Ag particles. In the potential region of mixed diffusion and kinetically controlled current the kinetic oxygen reduction current density, J_k, was calculated and utilised to construct a Tafel plot (log J_k versus E). Figure 6.3-2(B) illustrates the corresponding Tafel plot of the measured data in figure 6.3-2(A). Within a certain potential range, 0.7–0.9 V_{RHE}, the curves for the NP Ag recorded for different catalyst loadings are parallel to each other with a constant Tafel slope of 120 mV dec^{-1}, as determined by a linear regression of the data. The current densities are shifted by the respective factor in the applied loading. This scalability of the kinetic reduction current with the loading is an important prerequisite for a reasonable analysis by the thin-film RDE method. Only then the true catalytic activity of an electrocatalyst towards the ORR, expressed by two equally important characteristics, namely the mass specific activity (in short mass activity) and the surface area specific activity (specific activity), can be determined from the Tafel plot.

6.3.2 Mass Activity

The mass activity ($J_{k:m}$), i.e. the normalisation of the kinetic current to the catalyst loading (σ_L), is especially of economic importance, since it directly indicates the cost of energy conversion related to the deployed amount of catalyst. A scalability of the total kinetic current with the catalyst loading, as obtained for the NP Ag in this study, guarantees that all the catalyst is used in the reaction. The mass activity of the NP Ag catalyst determined by averaging 12 samples of several different loadings in the range from 50 to 200 µgcm^{-2} is plotted in figure 6.3-4. At 0.9 V_{RHE} the mass activity is 2.0 × 10^{-6} A µg^{-1}. The standard deviation of the NP Ag measurements in the potential region of interest is less than 10%. Such a small error in mass activity over a mass span of a factor of 4 additionally proves the full usage of the catalyst.
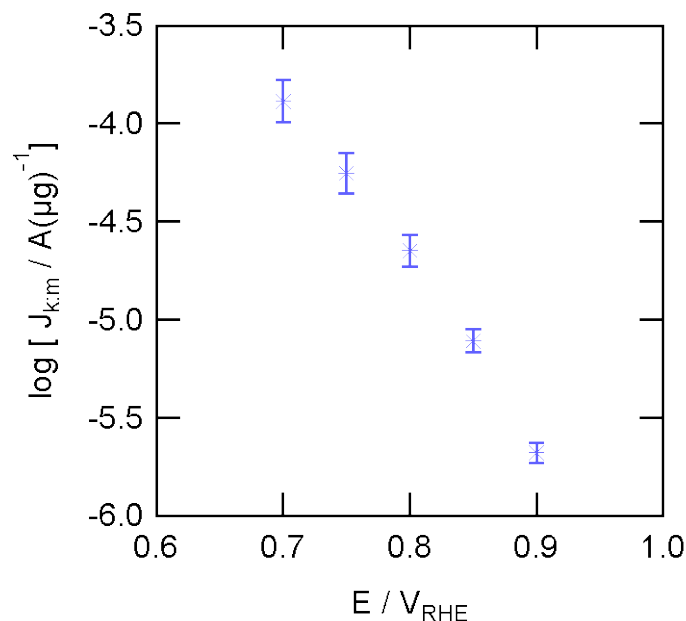
Figure 6.3-4: Tafel plot the kinetic current density of the ORR normalized to the metal loading of NP Ag (mass activity) obtained from 12 independent measurements with different loadings between 50 and 200 µgcm^{-2}.

6.3.3 Determination of Electrochemically Accessible Sites

The standard Pt surface area determination techniques CO and H$_{upd}$ stripping often cannot be applied for non-platinum catalysts, as they are generally inactive towards these reactions. Consequently for each type of catalyst a suitable surface area determination technique has to be explored [78]. For the Ag electrodes in this thesis Pb$_{upd}$ stripping (1), and for additional comparison the reduction of Pb(IV), were implemented.

$$Pb + 3OH^- \rightleftarrows HPbO_2^- + H_2O + 2e^- \qquad (40)$$
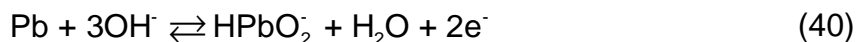
The upd of Pb on Ag has been described before [15, 93]. A monolayer of Pb can be deposited onto an Ag electrode at potentials more positive than expected by the equilibrium potential for bulk deposition. In order to form a complete monolayer of Pb, different deposition potentials were chosen as negative as possible, while at the same time avoiding Pb multilayer deposition. Latter introduces an additional peak in the stripping voltammogram at lower potentials [see figure 6.3-5(A)], and thereby leads to an overestimation of the active surface area. Furthermore, the deposition time t$_d$ was varied in order to allow the system to reach equilibrium [79]. In detail, the

145

optimised E_d was determined by conducting several stripping experiments with several E_ds between 0.2 and 0.5 V_{RHE} and t_ds ranging from 1 to 600 s. The optimised values for PC Ag were a t_d of 300 s and an E_d of 0.23 V_{RHE}, respectively. Using these parameters the Pb stripping charge reached a maximum without any visible Pb bulk deposition [see figure 6.3-5 (A)]. Note, however, that these parameters may differ slightly for different NP Ag catalysts. The number of electrochemically accessible sites (N_{ECAS}) was calculated from the stripping voltammogram assuming a one to one ratio of Pb to Ag atoms. An additional methodology utilising Pb(IV) species was employed to determine the surface charge for comparison.
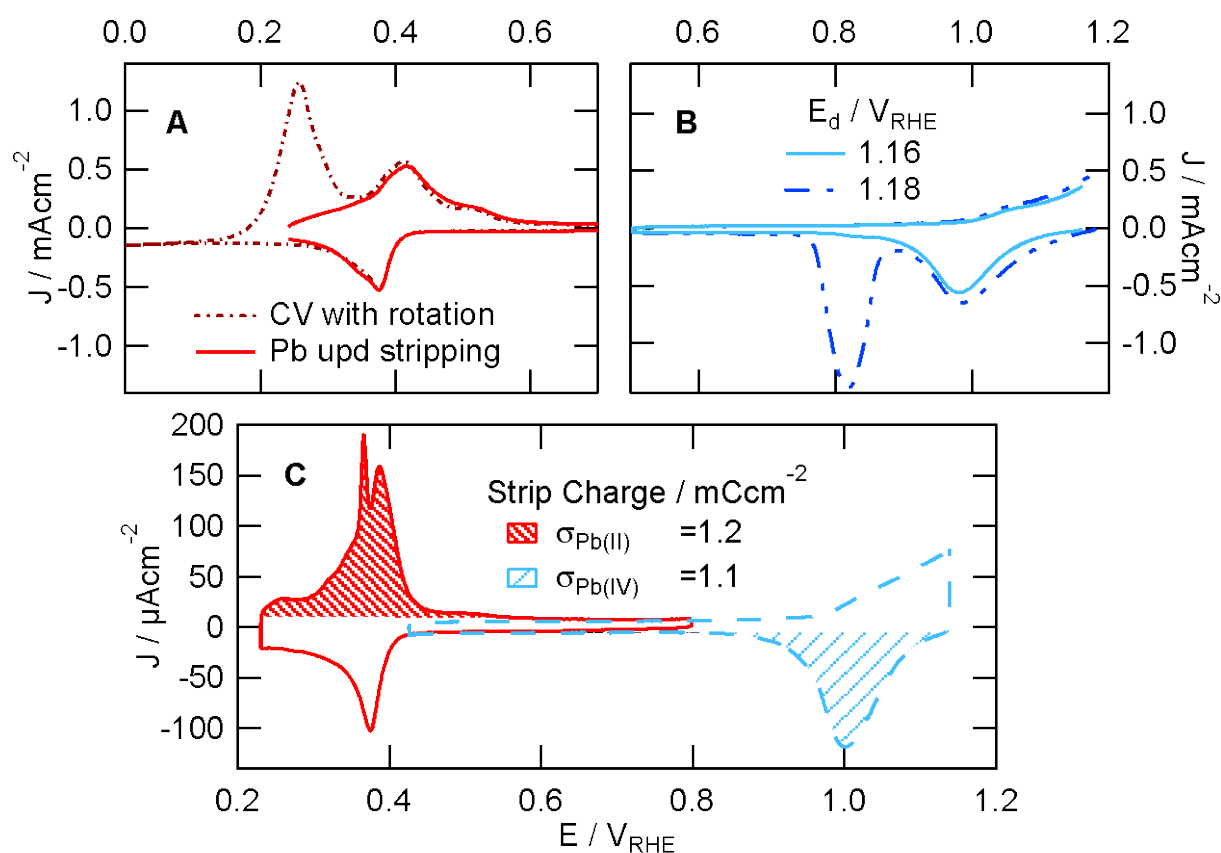
Figure 6.3-5: **Voltammograms of a PC Ag electrode recorded with 0.1 V s^{-1} in Ar-saturated 0.1 M KOH + 125 µM Pb(NO$_3$)$_2$ solution; (A) strip voltammogram after 180 s at Ed = 0.23 V$_{RHE}$ (solid line), consecutive voltammogram recorded with a more negative potential limit and rotation rate of 900 rpm (dotted line). (B) Pb(IV) stripping curves recorded at E$_d$ = 1.160 and 1.180 V$_{RHE}$. (C) Optimized strip voltammogram of Pb upd (left) and Pb(IV)**

(right) at 0.01 Vs^{-1} from NP Ag sample with loading 100 µgcm^{-2}. Shaded areas indicate the corresponding charges.

Pb(IV) forms an adsorbed monolayer on Ag electrodes dependent on the applied E_d in the range of 1.15–1.20 V_{RHE}, and is observed in the negative going sweep by a reduction peak at 0.95 V_{RHE} [see figure 6.3-5(B)]. If the deposition potential is increased beyond 1.19 V_{RHE}, lead-dioxide is formed (2) [75] and a t_d dependent, second reduction peak occurs at 0.75 V_{RHE}.

$$PbO + 2OH^- \rightleftarrows PbO_2 + H_2O + 2e^- \tag{41}$$
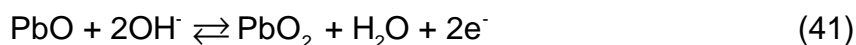
Analogous to the optimisation scheme used in Pb$_{upd}$ stripping, the E_d and t_d parameters for Pb(IV) were found by maximising the monolayer Pb(IV) stripping peak I, without forming the second reduction peak II [figure 6.3-5 (B)]. Pb$_{upd}$ and Pb(IV) stripping measurements on PC Ag reproducibly resulted in a charge density of 450 µCcm^{-2}. This is slightly higher than the values reported in the literature, i.e. 400 µCcm^{-2} for Pb$_{upd}$ [68], and 200 µCcm^{-2} for the one electron process Tl$_{upd}$ [80], which might be due to a slightly roughened electrode surface.

Figure 6.3-5(C) shows the optimised stripping voltammograms of Pb$_{upd}$ and Pb(IV) from a NP Ag sample with 100 µgcm^{-2} loading, resulting in a surface charge density $\sigma_{q,\,Pb}$ = 1.2 mC cm^{-2} and $\sigma_{q,Pb(IV)}$ = 1.1 mC cm^{-2}, respectively. The difference of less than 10% between the two stripping methods is a result of the error in the correction of the capacitive currents and in the selection of the integration limits. Interestingly, it was observed that compared to PC Ag the optimised E_d values for Pb$_{upd}$ are shifted 30 mV more positive, whilst the E_d for Pb(IV) are shifted 30 mV more negative. In further contrast to PC Ag, the stripping charge of NP Ag was found to decrease by ≈5% for consecutive Pb$_{upd}$ stripping measurements, which could be due to a partial detachment of particles. It is noteworthy, that the post-ORR surface areas of the Ag particles in some cases diverted up to 30% from the surface areas determined before measuring the ORR. Since the particles are only attached to the substrate by weak electrostatic forces, these losses might be either due to the rotation during recording the ORR and the cell exchange procedure or due to Ag dissolution. Although both processes are difficult to distinguish during the measurement, the latter process was minimised by limiting the upper potential to 1.05 V_{RHE}, where in the CV still no Ag oxide peaks are detected. In the case of a large discrepancy in the post-ORR surface

area, the data were not further evaluated. That is, the activities of only those measurements were analysed, where the surface area loss within the measurement was negligible.
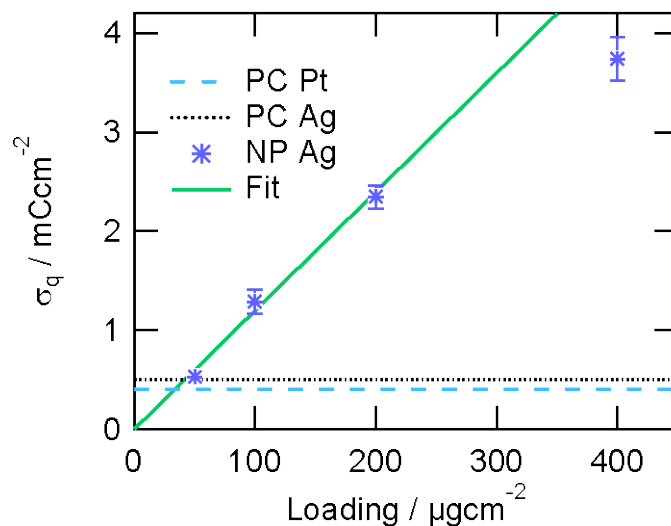
Figure 6.3-6:   **Charge density of NP Ag determined by Pb stripping as a function of the catalyst loadings in several independent measurements according to method described in the text. The dotted black line indicates a linear regression (loading of 400 µgcm^{-2} is not included); the determined slope is 12 C g^{-1}.**

The surface area determination can be applied to probe the full accessibility of the catalyst surface, as proposed in the determination of the mass activity. The results from the stripping experiments as a function of NP Ag loading are shown in figure 6.3-6. It can be seen that σ_q indeed depends linearly on the catalyst loading up to 200 µgcm^{-2}; so all the catalyst is utilised and these samples can be used for determining the specific ORR activities. For higher loadings of 400 µgcm^{-2}, however, the ratio deviates from the linear regression, so that specified mass activities lead to erroneous results and have to be discarded.

6.3.4 Specific Activity/Turnover Frequency

After determining the electrochemically accessible sites, the surface area specific activity of the catalysts can be calculated by assuming a standard charging value per surface area for the material. However, for alloys or the recently reported Fe/N/C type of catalysts [94] the correct standard charging value is often problematic. For

example for a Pt alloy system in alkaline solution the exact surface composition is in general not known and thus a standard value in terms of charge per surface area cannot be given. Instead, a normalisation of the catalytic activity to the implicit charging/decharging value avoids such assumptions, resulting in an activity in the form of a turn over frequency (TOF) [19]. In the presented work both properties were determined; the TOF of the ORR by dividing the number of reacting molecules per unit time (determined by kinetic current) by the number of electrochemically accessible sites (determined by the Pb stripping charge measured after the ORR). The specific activity was calculated by multiplying the TOF value with 400 µCcm^{-2}, i.e. the normalisation constant of a two electron process for the surface area of PC Ag as given in the literature [68]. In figure 6.3-7 the resulting TOF determined from the same 12 samples as in figure 6.3-4 are plotted as a function of potential along with the TOF values obtained for PC Ag and PC Pt. Analogous to the standard deviation of the NP Ag mass activity, the deviation in the potential region of interest is below 10%. Furthermore it can be seen that at 0.9 V_{RHE} the TOF of NP Ag is 0.1 Hz, equivalent to that of PC Ag and one order of magnitude less than PC Pt. At lower potentials, the difference in activity between Pt and Ag increases further due to the different Tafel slopes.
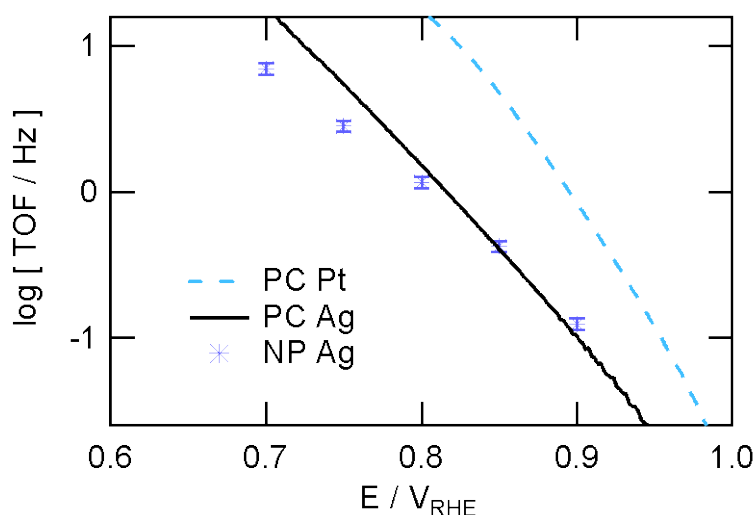

Figure 6.3-7: **Tafel plot of the established turn over frequency of the ORR on NP Ag (markers), PC Ag (solid line) and PC Pt (dashed line) in 0.1 M KOH.**

6.3.5 Comparison

The thorough evaluation of the NP Ag catalyst enables a comparison with activities of PC Pt and Ag from literature. The kinetic parameters of the ORR obtained in this work are summarised in Table 6.3-1 along with values from other references. Although the literature data for the ORR kinetic activity of PC Pt varies significantly, it is one of the most active materials and should serve as a benchmark for any comparison. Note that PC Pt exhibits a hysteresis during ORR in contrast Ag. In general, the forward scan is taken as comparison although it is not under steady state condition. In this work we obtained a TOF of 1 Hz at 0.9 V_{RHE} on PC Pt, and a Tafel slope of 60 mV dec^{-1}; these values compare reasonably well with literature values for Pt PC in perchloric acid electrolyte [5, 35]. Thus results from this work indicate that there is a comparably small difference in the TOF on PC Pt in acid and alkaline solution. However, in the literature one order of magnitude lower TOF values are reported for the ORR in alkaline electrolyte [74, 95-96]. In these previous studies contradictory values of the Tafel slope from 60 [96] up to 120 mV dec^{-1} [74, 95] are determined, demonstrating that even a basic system like PC Pt is subject to inconsistencies. It should be pointed out that latter measurements were performed in standard electrochemical glass cells, allowing impurities from the glass to leach into the alkaline electrolyte [22-23], whose detrimental effects on activity measurements cannot be ruled out.

Comparing the Ag data of this study with the literature, the TOF of PC Ag of 0.1 Hz at 0.9 V_{RHE} is (as for PC Pt) up to one order of magnitude higher than previously reported [8, 91, 97]. Possible reasons for this are the complete reduction of Ag, the R_{sol} compensation and the applied subtraction of the capacitive current. The reduction of silver has an enhancing effect on the ORR and the reduction potential used in this study is more negative than in previous studies. Furthermore, the actual faradaic current at 0.9 V_{RHE} is small; consequently the measured total current is highly subjective to the influence of any capacitive currents, which therefore must be considered. The Tafel slopes obtained for PC Ag correspond well to the literature values for PC Ag [8, 91] and Ag single crystals [97]. Since in contrast to previous studies a compensation of R_{sol} was applied, increased activities and a linear Tafel slope were observed in a potential window of over 200 mV. Different Tafel slopes

obtained in previous studies in a low and a high potential region are most likely an artefact of RDE measurements due to an improper R_{sol} compensation.

Previous studies on Ag nanoparticles have provided unsatisfactorily comparable activities, as the catalyst surface area was not measured, nor was the scalability of the activity with loading investigated [30, 82]. The mass activity for the NP Ag catalyst of this study is 2.0×10^{-6} Aμg^{-1}. Interestingly, the Tafel slope of $\approx$120 mV dec^{-1} for unsupported NP Ag does not correspond to that of PC Ag of 90 mV dec^{-1}, while the TOF at 0.9 V_{RHE} is identical. The reason for this behaviour is still unclear at this point. Comparing Ag to Pt, it is evident that in alkaline solution the TOF on PC Ag at 0.9 V_{RHE} is about one order of magnitude lower than on PC Pt (see Table 6.3-1). The mass activity for the NP Ag catalyst of 2.0×10^{-6} A μg^{-1} is significantly lower than that of a state of the art carbon supported platinum high surface area catalyst. The divergence is partially due to the difference in particle size, i.e. 100 nm for Ag versus sub-10 nm for Pt, and the therefore lower active surface area. So the mass activity of NP Ag could still be increased decisively by further reducing the particle size, as long as no eventually opposing particle size effect as for the ORR on Pt appears [98]. The Tafel slopes for NP Ag and PC Ag are, however, higher than the Tafel slope for Pt, which is clearly a disadvantage at higher overpotentials. Neglecting any other influence, such as long-term stability, required catalyst film thickness in the MEA, etc., the economical conversion efficiency is quite similar. Albeit having one magnitude lower specific activity for ORR than platinum, Ag and alkaline based FCs might be a plausible candidate in future due to their low cost.

Catalyst for ORR	TOF log(TOF/Hz) at 0.9 V_{RHE}	Spec. Activity log($J_{k:ECA}$/Acm^{-2}) at 0.9V_{RHE}	Mass Activity log($J_{k:m}$/Aµg^{-1}) at 0.9V_{RHE}	Tafel Slope (mV/dec)	Reference
Ag(110)	-1.1	-4.4	-	80 (cont. changing)	[97]
Ag(100)	-1.6	-4.7			
PC Ag	-0.9	-4.0	-	90	figure 6.3-7
	-2.0	≈-5		90	[8, 91]
NP Ag	-1.0	-4.0	-5.7	120	Here
PC Pt	-0.1	-3.1	-	60	figure 6.3-7
	0.2	-2.9		60	[35] [a]
	0.6	-2.6		60	[5] [a T]
	-0.9	-4.0		104	[95] [b]
	-0.6	-3.7		120	[74] [b]
	-1.3	-4.4		60	[96] [b]
Pt/HSC-E 45.9% (TKK)	-0.7	-3.7	-4	-	[5] [a T]

Table 6.3-1: **ORR kinetic parameters on bulk Silver (PC Ag), platinum (PC Pt), and nanoparticles of Silver (NP Ag). The TOF from literature source were calculated by dividing the specific area with the charge density of the specific material, i.e. 195 µC/cm² for Platinum [35], 200 µC/cm² for PC Ag [68], 185 µC/cm² for Ag(100) [99] and 140 µC/cm² for Ag(110) [99]. Due to the large scatter of the data and for the sake of an easy comparison, the values are given with an accuracy of only one digit.**

[a] in acid electrolyte

[b] in basic electrolyte

[T] experiment at 60°C

6.4 Conclusion

A standardised ORR thin-film RDE study of a non-platinum catalyst was performed, by applying a similar methodology as for platinum high surface area catalysts reported previously. A silver nanoparticle catalyst supported on glassy carbon was characterised with respect to the number of electrochemically accessible sites and the activity of oxygen reduction in alkaline solution. The full catalyst layer usage was verified by the linear scaling of NECAS and ORR activity with loading up to values of 200 μgcm^{-2}. Due to the loading optimisation and an adequate R_{sol}-compensation, representative activities were obtained with high accuracy at FC relevant potentials. Regarding the activity of the catalysts, no differences were found between the TOF of the NP Ag catalyst and PC Ag. The TOF on NP Ag and PC Ag at 0.9 V_{RHE} is about one order of magnitude less than for PC Pt. Furthermore, it is established that the TOF on PC Pt in 0.1 M KOH and 0.1 M $HClO_4$ do not vary significantly and exhibit the same Tafel slope of 60 mV dec^{-1}.

6.4.1 Guidelines

The following guidelines that can be applied for the characterization of various kinds of catalysts by the thin-film RDE methodology:

G1. The number of electrochemical active sites (N_{ECAS}) has to be determined. The obtained value has to independent of the applied methodology

G2. Capacitive currents must be subtracted for the evaluation of the electrocatalytic activity

G3. Compensation schemes for the solution resistance (R_{sol}) must be used

G4. The diffusion limit current of ORR should be within 10% of the theoretical value

G5. The current at the potential of interest has to be within 10% and 80% of the diffusion limit current, ideally below the half wave potential

G6. The electrode thickness for the thin-layer method should not exceed 0.1 μm

G7. Reaction rate and N_{ECAS} must depend linearly on loading

G8. Normalized activities, i.e. mass activity and turn over frequency, should be expressed in a fuel cell relevant potential window vs. the reversible hydrogen electrode

The first five guidelines are applicable to all activity measurement, whilst the last three are specific for nano-sized catalysts. The measurement of N_{ECAS} (G1) and the subtraction of capacitive currents (G2) enable adequate evaluation and normalization of the activity. (G3) ensures a correct potential determination and application, i.e. minimizes the potential errors due to solution resistance; while (G4) indicates the complete coverage of the GC with the catalyst. The potential window of measurable kinetic currents can be shifted by changing the catalyst loading; thereby avoiding extrapolation errors (G5). The range of useful loadings has an upper limit, since the catalyst layer must be kept thin (G6) in order to avoid any diffusion resistance. At higher loadings the catalyst usage is below 100%, shown by a deviation from the linear activity/N_{ECAS} to loading relation (G7). Lastly, the data should be presented in a manner that enables a straightforward comparison (G8); not only to other RDE measurements, but also to flow cell and actual fuel cell data.

7 Summary

The objectives of this work can be separated into three different topics: the design and development of a state-of-the art electrochemical experiment setup, which is then followed by two separate experimental studies in alkaline electrolyte. These studies demonstrate the capabilities of the experimental setup, and each focus on separate model catalysts. The first study investigated the influence of Pt oxide formation on the measured catalytic activity of FC relevant reactions on polycrystalline Pt in alkaline electrolyte. The second study focused on the characterisation of the ORR for a non-platinum catalyst, in this case Ag, by adapting the established thin-film RDE methodology employed for characterising Pt based electrocatalysts.

A state-of-the-art electrochemical experimental setup comprises of a largely automated setup that allows meticulous control over experimental parameters such as potential, temperature, purging gas and solution convection. In order to realise such a setup, both experimental hardware and software were developed. In particular, a custom built analogue potentiostat optimised for single working electrode measurements was constructed. The potentiostat features R_{sol}-compensation which can be monitored online due to its fully analogue design, allowing the precise current and potential relationship to be measured. In addition, the experimental throughput was enhanced by fabricating a modular add-on device, the MWE, which allows simultaneous electrochemical measurement on up to 8 parallel working electrodes. The MWE device is compatible with any single channel potentiostat, enhancing existing instrumentation. Several Teflon cells were designed for electrochemical investigations in acid and alkaline electrolytes, and were adapted to work using either the RDE or MWE. A gas changer was also assembled, which enabled computer controlled switching of electrolyte purge gas. Furthermore, in order to control the potentiostat and the accessory hardware, several data acquisition software applications were programmed with Labview. These programs feature both manual and text script control over the electrochemical techniques and experimental parameters. Using text script control, standardized measurement protocols consisting of several EC techniques can be executed in order to perform numerous experiments with identical measurement procedures. To allow rapid treatment, analysis and

comparison of electrochemical data, a custom data treatment program was also created.

Once the electrochemical setup was established, the role of surface oxides on the kinetics of the ORR, the oxidation/reduction of peroxide and the HOR was studied on PC Pt in alkaline electrolyte. This is of fundamental interest because a significant change in ORR activity occurs in the same potential region as the onset of Pt oxide formation. Although Pt surface oxidation is relatively fast in alkaline solution, the coverage could not be considered to be at equilibrium during the course of a CV. Therefore, a stripping procedure was used in order to probe the role of the equilibrium coverage of surface oxides on the measured activity. By correlating the key observations of the stripping procedure (stripping peak potential and charge) in Ar, with the activity and halfwave potential of the HOR as function of the deposition potential, the potential regions in which the different Pt oxide spectator species predominate could be deduced. This experimental procedure was then applied to the study of the ORR and HO_2^- reduction reactions. In doing so, it was shown experimentally that at steady-state PtOH is not simply a spectator species, but is directly involved in the ORR and HO_2^- reduction reaction pathway. During these reactions, PtO species are formed at potentials more negative than that required to oxidise PtOH, and consequently the PtO is quickly reduced to PtOH. This causes the number of OH species on the Pt surface to increase, shifting the coverage away from equilibrium and driving the reduction of the PtOH surface species to H_2O freeing a Pt site. It was not, however, possible to distinguish between the two possible ORR mechanisms, either associative or dissociative using this technique because the reduction and oxidation of HO_2^- on PC Pt is always diffusion limited.

In the second study, a methodology was developed in order to determine the ORR activity of a non-platinum catalyst using the thin-film RDE technique. Here, a Ag nanoparticle catalyst deposited onto a glassy carbon substrate was first characterised in terms of the NECAS using the upd of Pb. The catalyst utilisation was assessed and verified by scaling the NECAS and ORR activity with catalyst loading up to values of 200 μg cm^{-2}. Once an appropriate loading was established, both the TOF, mass and specific activity of Ag nanoparticles towards the ORR in alkaline solution could be precisely determined at FC relevant potentials. No difference was observed between the ORR activity of the NP Ag catalyst and model PC Ag

electrode. Furthermore, the ORR TOF on Ag at 0.9 V_{RHE} (0.1 Hz) is approximately one order of magnitude less than on PC Pt. Finally, a set of methodology guidelines were recommended for future characterisation of both Pt and non-Pt nanoparticle catalysts, in order to facilitate meaningful activity comparisons between different types of catalysts.

To summarise, the state-of-the-art electrochemical setup developed in this work allows precise study and characterisation of various electrodes using a variety of EC techniques under controlled experimental conditions. Its effectiveness was demonstrated by the experimental elucidation of the role of PtOH species on the measured catalytic activity of the ORR. Finally, a methodology to characterise the catalytic activity of a non-Pt catalyst towards the ORR was developed.

8 List of References

1. Ro, S.T. and J.L. Sohn, *Some issues on performance analysis of fuel cells in thermodynamic point of view.* Journal of Power Sources, 2007. **167**(2): p. 295-301.
2. Gewirth, A.A. and M.S. Thorum, *Electroreduction of Dioxygen for Fuel-Cell Applications: Materials and Challenges.* Inorganic Chemistry, 2010. **49**(8): p. 3557-3566.
3. Rakopoulos, C.D. and E.G. Giakoumis, *Second-law analyses applied to internal combustion engines operation.* Progress in Energy and Combustion Science, 2006. **32**(1): p. 2-47.
4. U.S. Department of Energy. *Fuel Cell Technology Challenges.* 2008; Available from: http://www1.eere.energy.gov/hydrogenandfuelcells/fuelcells/fc_challenges.html.
5. Gasteiger, H.A., et al., *Activity benchmarks and requirements for Pt, Pt-alloy, and non-Pt oxygen reduction catalysts for PEMFCs.* Applied Catalysis B: Environmental, 2005. **56**(1-2): p. 9-35.
6. Chen, S., et al., *Enhanced Activity for Oxygen Reduction Reaction on "Pt3Co" Nanoparticles: Direct Evidence of Percolated and Sandwich-Segregation Structures.* Journal of the American Chemical Society, 2008. **130**(42): p. 13818-13819.
7. Mayrhofer, K.J.J., et al., *Degradation of Carbon-Supported Pt Bimetallic Nanoparticles by Surface Segregation.* Journal of the American Chemical Society, 2009. **131**(45): p. 16348-16349.
8. Sepa, D., M. Vojnovic, and Damjanov.A, *Oxygen Reduction at Silver Electrodes in Alkaline Solutions.* Electrochimica Acta, 1970. **15**(8): p. 1355.
9. Calegaro, M.L., F.H.B. Lima, and E.A. Ticianelli, *Oxygen reduction reaction on nanosized manganese oxide particles dispersed on carbon in alkaline solutions.* Journal of Power Sources, 2006. **158**(1): p. 735-739.
10. Yeager, E., *Electrocatalysts for O2 reduction.* Electrochimica Acta, 1984. **29**(11): p. 1527-1537.
11. Wang, G., et al., *Developing a polysulfone-based alkaline anion exchange membrane for improved ionic conductivity.* Journal of Membrane Science, 2009. **332**(1-2): p. 63-68.
12. Oelßner, W., F. Berthold, and U. Guth, *The iR drop - well-known but often underestimated in electrochemical polarization measurements and corrosion testing.* Materials and Corrosion, 2006. **57**(6): p. 455-466.
13. Bard, A.J. and L.R. Faulkner, *Electrochemical Methods: Fundamentals and Applications, 2nd ed.* 2nd ed. 2001, New York: John Wiley & Sons. 833.
14. Scherson, D.A., et al., *Extensions of the Koutecky--Levich Equation to Channel Electrodes.* Electrochemical and Solid-State Letters, 2008. **11**(2): p. F1-F4.
15. Kirowa-Eisner, E., D. Tzur, and E. Gileadi, *Underpotential dissolution of metals under conditions of partial mass-transport control.* Journal of Electroanalytical Chemistry, 2008. **621**(2): p. 146-158.
16. Haber, F., Zeitschrift für Physikalische Chemie, 1900. **32**: p. 207.

17. Barnartt, S., *Magnitude of IR-Drop Corrections in Electrode Polarization Measurements Made with a Luggin-Haber Capillary.* Journal of The Electrochemical Society, 1961. **108**(1): p. 102-104.

18. Machado, S.A.S., A.A. Tanaka, and E.R. Gonzalez, *Underpotential deposition of copper and its influence in the oxygen reduction on platinum.* Electrochimica Acta, 1991. **36**(8): p. 1325-1331.

19. Burwell, R.L.J., *Manual of Symbols and Terminology for Physicochemical Quantities and Units - Appendix II. Definitions, Terminology and Symbols in Colloid and Surface Chemistry. Part II: Heterogeneous Catalysis.* Pure and Applied Chemistry, 1976. **46**(1): p. 71-90.

20. Gamry Instruments. *Electrochemical Cells.* 2010; Available from: http://www.gamry.com.

21. Mahoney, L.A., J. O'Dea, and J.G. Osteryoung, *Determination of charge transfer kinetic parameters using an automated flow system.* Journal of Electroanalytical Chemistry, 1994. **366**(1-2): p. 81-92.

22. Mayrhofer, K.J.J., G.K.H. Wiberg, and M. Arenz, *Impact of Glass Corrosion on the Electrocatalysis on Pt Electrodes in Alkaline Electrolyte.* Journal of The Electrochemical Society, 2008. **155**(1): p. P1-P5.

23. Mayrhofer, K.J.J., et al., *Analysis of the Impact of Individual Glass Constituents on Electrocatalysis on Pt Electrodes in Alkaline Solution.* Journal of The Electrochemical Society, 2008. **155**(6): p. P78-P81.

24. Gohr, H., M. Mirnik, and C.A. Schiller, *Distortions of high frequency electrode impedance : Their causes and how to avoid them.* Journal of Electroanalytical Chemistry, 1984. **180**(1-2): p. 273-285.

25. Mayrhofer, K.J.J., et al., *An Electrochemical Cell Configuration Incorporating an Ion Conducting Membrane Separator between Reference and Working Electrode.* International Journal of Electrochemical Science, 2009. **4**(1): p. 1-8.

26. HENGSTLER GmbH. *Temperature Controller grado 901.* 2010; Available from: http://www.hengstler.com.

27. Nordling, C. and J. Österman, *Physics Handbook, 6th Edition.* 6 ed. 1999, Lund: Studentlitteratur AB.

28. Princeton Applied Research. *Potential Error Correction (iR Compensation)* Technical Note; 101:[Available from: http://new.ametek.com/content-manager/files/PAR/086.pdf.

29. Princeton Applied Research. *Model 263A, Potentiostat/Galvanostat, Users Guide.* Available from: http://www.artisan-scientific.com/info/PAR_263A_Users_Manual.pdf.

30. Demarconnay, L., C. Coutanceau, and J.M. Léger, *Electroreduction of dioxygen (ORR) in alkaline medium on Ag/C and Pt/C nanostructured catalysts--effect of the presence of methanol.* Electrochimica Acta, 2004. **49**(25): p. 4513-4521.

31. Cummings, T.E., M.A. Jensen, and P.J. Elving, *Construction, operation and evaluation of a rapid-response potentiostat.* Electrochimica Acta, 1978. **23**(11): p. 1173-1184.

32. Southhampton Electrochemistry Group, *Instrumental Methods in Electrochemistry.* Ellis Horwood, ed. T.J. Kemp. 1990, London.

33. Carter, B. and T.R. Brown, *Handbook of operational amplifier applications*, in *Application Report - SBOA092A.* 2001, Texas Instruments Inc.: Dallas.

34. Horowitz, P. and W. Hill, *The art of electronics, 2nd Edition.* 2nd ed. 1989, Cambridge: Cambridge Press.

35. Mayrhofer, K.J.J., et al., *Measurement of oxygen reduction activities via the rotating disc electrode method: From Pt model surfaces to carbon-supported high surface area catalysts.* Electrochimica Acta, 2008. **53**(7): p. 3181-3188.

36. Uniscan Instruments Ltd. *PG580RM - Multi - Channel Potentiostat - Galvanostat.* 2010; Available from: http://www.uniscan.com/multichannel_potentiostats.html.

37. Scribner Associates Inc. *Multi-Channel Potentiostat Model 445.* 2010; Available from: http://www.scribner.com/multi-channel-potentiostat-model-445.html.

38. Joffe, E.B. and K.-S. Lock, *Grounds for Grounding: A Circuit to System Handbook.* 2010, Hoboken, New Jersey: John Wiley & Sons, Inc. 1064.

39. Arenz, M., et al., *The Effect of the Particle Size on the Kinetics of CO Electrooxidation on High Surface Area Pt Catalysts.* Journal of the American Chemical Society, 2005. **127**(18): p. 6819-6829.

40. Chan, F., J. Cao, and Y. Sun, *High-level abstractions for message-passing parallel programming.* Parallel Computing, 2003. **29**(11-12): p. 1589-1621.

41. Johnston, W.M., J.R.P. Hanna, and R.J. Millar, *Advances in dataflow programming languages.* ACM Comput. Surv., 2004. **36**(1): p. 1-34.

42. Hinchey, M.G., *Visual methods in real-time programming.* Control Engineering Practice, 1995. **3**(6): p. 837-842.

43. National Intrument Corporation. Available from: http://www.ni.com.

44. Belletti, A., R. Borromei, and G. Ingletto, *Teaching Physical Chemistry Experiments with a Computer Simulation by LabVIEW.* Journal of Chemical Education, 2006. **83**(9): p. 1353.

45. Elliott, C., et al., *National Instruments LabVIEW: A Programming Environment for Laboratory Automation and Measurement.* Journal of the Association for Laboratory Automation, 2007. **12**(1): p. 17-24.

46. Muyskens, M.A., et al., *Data Acquisition in the Chemistry Laboratory Using LabVIEW Software.* Journal of Chemical Education, 1996. **73**(12): p. 1112.

47. Economou, A., et al., *A "virtual" electroanalytical instrument for square wave voltammetry.* Analytica Chimica Acta, 2002. **467**(1-2): p. 179-188.

48. Bitter, R., T. Mohiuddin, and M. Nawrocki, *Chapter 9. Multithreading in LabVIEW*, in *LabVIEW: Advanced Programming Techniques, SECOND EDITION.* 2007, CRC Press. p. 397–442.

49. WaveMetrics Inc. *Igor.* Available from: http://www.wavemetrics.com/.

50. OriginLab Corporation. *Origin.* Available from: http://www.originlab.com/.

51. Microsoft Corporation. *Excel.* Available from: http://office.microsoft.com/en-gb/excel.

52. Hitachi Display Products Group. *LCD screen: TX43D55VM0BAA.* 2010 [cited 2010; Available from: http://www.hitachi-displays-eu.com/.

53. Damjanovic, A. and V. Brusic, *Electrode kinetics of oxygen reduction on oxide-free platinum electrodes.* Electrochimica Acta, 1967. **12**(6): p. 615-628.

54. Damjanovic, A., M.A. Genshaw, and J.O.M. Bockris, *The Mechanism of Oxygen Reduction at Platinum in Alkaline Solutions with Special Reference to H[sub 2]O[sub 2].* Journal of The Electrochemical Society, 1967. **114**(11): p. 1107-1112.

55. Sepa, D.B., M.V. Vojnovic, and A. Damjanovic, *Reaction intermediates as a controlling factor in the kinetics and mechanism of oxygen reduction at platinum electrodes.* Electrochimica Acta, 1981. **26**(6): p. 781-793.

56. Conway, B.E., *Electrochemical oxide film formation at noble metals as a surface-chemical process.* Progress in Surface Science, 1995. **49**(4): p. 331-452.

57. Markovic, N.M., et al., *Oxygen reduction reaction on Pt(111): effects of bromide.* Journal of Electroanalytical Chemistry, 1999. **467**(1-2): p. 157-163.

58. Norskov, J.K., et al., *Origin of the Overpotential for Oxygen Reduction at a Fuel-Cell Cathode.* The Journal of Physical Chemistry B, 2004. **108**(46): p. 17886-17892.

59. Hansen, H.A., J. Rossmeisl, and J.K. Norskov, *Surface Pourbaix diagrams and oxygen reduction activity of Pt, Ag and Ni(111) surfaces studied by DFT.* Physical Chemistry Chemical Physics, 2008. **10**(25): p. 3722-3730.

60. Markovic, N.M. and P.N. Ross, *Surface science studies of model fuel cell electrocatalysts.* Surface Science Reports, 2002. **45**(4-6): p. 117-229.

61. Angerstein-Kozlowska, H., B.E. Conway, and W.B.A. Sharp, *The real condition of electrochemically oxidized platinum surfaces: Part I. Resolution of component processes.* Journal of Electroanalytical Chemistry, 1973. **43**(1): p. 9-36.

62. Biegler, T. and R. Woods, *Limiting oxygen coverage on smooth platinum anodes in acid solution.* Journal of Electroanalytical Chemistry, 1969. **20**(1): p. 73-78.

63. Bao, J. and D.D. Macdonald, *Oxidation of hydrogen on oxidized platinum: Part I: The tunneling current.* Journal of Electroanalytical Chemistry, 2007. **600**(1): p. 205-216.

64. Mayrhofer, K.J.J., et al., *Non-destructive transmission electron microscopy study of catalyst degradation under electrochemical treatment.* Journal of Power Sources, 2008. **185**(2): p. 734-739.

65. Damjanovic, A., M.A. Genshaw, and J.O.M. Bockris, *Distinction between Intermediates Produced in Main and Side Electrodic Reactions.* The Journal of Chemical Physics, 1966. **45**(11): p. 4057-4059.

66. Markovic, N.M., H.A. Gasteiger, and P.N. Ross, *Oxygen Reduction on Platinum Low-Index Single-Crystal Surfaces in Alkaline Solution: Rotating Ring DiskPt(hkl) Studies.* J. Phys. Chem., 1996. **100**(16): p. 6715-6721.

67. Scheller, F., et al., *Gesetzmässigkeit für den Diffusionsgrenzstrom an teilweise blockierten Modellelektroden.* Journal of Electroanalytical Chemistry, 1968. **19**(3): p. 187-198.

68. Kirowa-Eisner, E., et al., *Thermodynamics and kinetics of upd of lead on polycrystalline silver and gold.* Journal of Electroanalytical Chemistry, 2003. **552**: p. 171-183.

69. Jerkiewicz, G., et al., *Surface-oxide growth at platinum electrodes in aqueous H2SO4: Reexamination of its mechanism through combined cyclic-voltammetry, electrochemical quartz-crystal nanobalance, and Auger electron spectroscopy measurements.* Electrochimica Acta, 2004. **49**(9-10): p. 1451-1459.

70. Xia, S.J. and V.I. Birss, *In situ mass and ellipsometric study of hydrous oxide film growth on Pt in alkaline solutions.* Electrochimica Acta, 2000. **45**(22-23): p. 3659-3673.

71. Wakisaka, M., et al., *In situ STM observation of morphological changes of the Pt(111) electrode surface during potential cycling in 10 mM HF solution.* Physical Chemistry Chemical Physics, 2010. **12**(16): p. 4184-4190.

72. Zhang, T. and A.B. Anderson, *Hydrogen Oxidation and Evolution on Platinum Electrodes in Base: Theoretical Study.* The Journal of Physical Chemistry C, 2007. **111**(24): p. 8644-8648.

73. Wakisaka, M., et al., *Identification and Quantification of Oxygen Species Adsorbed on Pt(111) Single-Crystal and Polycrystalline Pt Electrodes by Photoelectron Spectroscopy.* Langmuir, 2009. **25**(4): p. 1897-1900.

74. Hsueh, K.L., E.R. Gonzalez, and S. Srinivasan, *Electrolyte effects on oxygen reduction kinetics at platinum: A rotating ring-disc electrode analysis.* Electrochimica Acta, 1983. **28**(5): p. 691-697.

75. Pourbaix, M., *Atlas of Electrochemical Equilibria in Aqueous Solutions.* 1966, Oxford: Pergamon Press Ltd.

76. Weaver, J.F., J.-J. Chen, and A.L. Gerrard, *Oxidation of Pt(1 1 1) by gas-phase oxygen atoms.* Surface Science, 2005. **592**(1-3): p. 83-103.

77. Bianchi, G., F. Mazza, and T. Mussini, *Catalytic decomposition of acid hydrogen peroxide solutions on platinum, iridium, palladium and gold surfaces.* Electrochimica Acta, 1962. **7**(4): p. 457-473.

78. Trasatti, S. and O.A. Petrii, *Real surface area measurements in electrochemistry.* Pure & Appl. Chern., Vol. 63, No. 5, pp. 71 1-734, 1991, 1991. **63**(5): p. 711-734.

79. Green, C.L. and A. Kucernak, *Determination of the Platinum and Ruthenium Surface Areas in Platinum–Ruthenium Alloy Electrocatalysts by Underpotential Deposition of Copper. I. Unsupported Catalysts.* The Journal of Physical Chemistry B, 2002. **106**(5): p. 1036-1047.

80. Daujotis, V. and E. Gaidamauskas, *Effect of anions on the underpotential deposition of thallium(I) on polycrystalline silver.* Journal of Electroanalytical Chemistry, 1998. **446**(1-2): p. 151-157.

81. Lima, F.H.B., J.F.R. de Castro, and E.A. Ticianelli, *Silver-cobalt bimetallic particles for oxygen reduction in alkaline media.* Journal of Power Sources, 2006. **161**(2): p. 806-812.

82. Chatenet, M., et al., *Oxygen reduction on silver catalysts in solutions containing various concentrations of sodium hydroxide – comparison with platinum.* Journal of Applied Electrochemistry, 2002. **32**(10): p. 1131-1140.

83. Shin, H. and C. Kang, *Adhesion of Gold Nanoparticles on an Electrochemically Pretreated Glassy Carbon Electrode.* Analytical Sciences, 2003. **19**(12): p. 1667-1670.

84. Vleeming, J.H., et al., *Graphite-Supported Platinum Catalysts: Effects of Gas and Aqueous Phase Treatments.* Journal of Catalysis, 1997. **166**(2): p. 148-159.

85. Droog, J.M.M., P.T. Alderliesten, and G.A. Bootsma, *Initial stages of anodic oxidation of silver in sodium hydroxide solution studied by potential sweep voltammetry and ellipsometry.* Journal of Electroanalytical Chemistry, 1979. **99**(2): p. 173-186.

86. Jovic, B.M., V.D. Jovic, and G.R. Stafford, *Cyclic voltammetry on Ag(111) and Ag(100) faces in sodium hydroxide solutions.* Electrochemistry Communications, 1999. **1**(6): p. 247-251.

87. Giles, R.D. and J.A. Harrison, *Potentiodynamic sweep measurements of the anodic oxidation of silver in alkaline solutions.* Journal of Electroanalytical Chemistry, 1970. **27**(1): p. 161-163.

88.   Tae Uk, H. and C. Won Sub, *The Mechanism of Silver(I) Oxide to Silver(II) Oxide Formation on Polycrystalline Silver Electrodes in 8 M KOH Solution.* Journal of The Electrochemical Society, 2005. **152**(5): p. A996-A1000.

89.   Tae Uk, H. and C. Won Sub, *Mechanism of Silver(I) Oxide Formation on Polycrystalline Silver Electrodes in 8 M KOH Solution.* Journal of The Electrochemical Society, 2005. **152**(1): p. A179-A185.

90.   Murray, B.J., et al., *Shape- and Size-Selective Electrochemical Synthesis of Dispersed Silver(I) Oxide Colloids.* Nano Lett., 2005. **5**(11): p. 2319-2324.

91.   Hurlen, T., Y.L. Sandler, and E.A. Pantier, *Reactions of oxygen and hydrogen peroxide at silver electrodes in alkaline solutions.* Electrochimica Acta, 1966. **11**(10): p. 1463-1473.

92.   Davis, R.E., G.L. Horvath, and C.W. Tobias, *The solubility and diffusion coefficient of oxygen in potassium hydroxide solutions.* Electrochimica Acta, 1967. **12**(3): p. 287-297.

93.   Kirowa-Eisner, E., R. Gepshtein, and E. Gileadi, *Effect of diffusion in underpotential deposition: Simulated and experimental results.* Journal of Electroanalytical Chemistry, 2005. **583**(2): p. 273-285.

94.   Lefevre, M., et al., *Iron-Based Catalysts with Improved Oxygen Reduction Activity in Polymer Electrolyte Fuel Cells.* Science, 2009. **324**(5923): p. 71-74.

95.   Couturier, G., et al., *Electrocatalysis of the hydrogen oxidation and of the oxygen reduction reactions of Pt and some alloys in alkaline medium.* Electrochimica Acta, 1987. **32**(7): p. 995-1005.

96.   Tammeveski, K., et al., *Electrochemical reduction of oxygen on thin-film Pt electrodes in 0.1 M KOH.* Electrochimica Acta, 1997. **42**(5): p. 893-897.

97.   Blizanac, B.B., P.N. Ross, and N.M. Markovic, *Oxygen Reduction on Silver Low-Index Single-Crystal Surfaces in Alkaline Solution: Rotating Ring DiskAg(hkl) Studies.* J. Phys. Chem. B, 2006. **110**(10): p. 4735-4741.

98.   Mayrhofer, K.J.J., et al., *The Impact of Geometric and Surface Electronic Properties of Pt-Catalysts on the Particle Size Effect in Electrocatalysis.* The Journal of Physical Chemistry B, 2005. **109**(30): p. 14433-14440.

99.   Dickertmann, D., F.D. Koppitz, and J.W. Schultze, *Eine methode zum ausschluss von randeffekten bei elektrochemischen messungen an einkristallen : Test anhand der adsorptionssysteme Ag/Pb2+ und Au/Cu2+.* Electrochimica Acta, 1976. **21**(11): p. 967-971.

9 Acknowledgment

10 Appendix

Statement (Erklärung)

Hiermit bestätige Ich, dass die der Fakultät für Chemie der Technischen Universität München zur Promotionsprüfung vorgelegt Arbeit mit dem Title:

The development of a state-of-the-art experimental setup demonstrated by the investigation of fuel cell reactions in alkaline electrolyte

im Lehrstuhl für Physikalische Chemie unter Anleitung und Betreuung durch Dr. M. Arenz ohne sonstige Hilfe erstellt und bei der Abfassung nur die gemäß § 6 Abs. 5 angegebene Hilfsmittle benutzt worden sind.

Die Dissertation in keinem anderen Prüfungsverfahren als Prüfungsleistung vorgelegt.

München, den 13.08.2010

Gustav Wiberg

Curriculum Vitae

Gustav K. H. Wiberg

Erikastr. 3, 80939 Munich, Germany

+49-17665-308204, +49-89-289-13394 (Office)

gustav.wiberg@gmail.com

Personal Information

Date of Birth	4th of March 1981
Place of Birth	Mölndal, Sweden
Nationality	Swedish

Academic Background

Oct. 2006 - Pres.	Technische Universität München, Munich, Germany **PhD** in Physical Chemistry Supervisor: Matthias Arenz
Sep. 2001 - Oct. 2006	Chalmers University of Technology, Göteborg, Sweden **Master of Science** (Civilingenjör) in Engineering Physics Master thesis: "Electrodeposition of Ni and Co/Cu Nanowires inside Microwave Connector for Magnetisation Dynamics Measurements" Supervisors: Jean-Philippe Ansermet (EPFL), Maj Hanson (Chalmers)
Sep. 2004 - Aug. 2005	École Polytechnique Fédérale de Lausanne (EPFL), Switzerland 4th year abroad, Exchange program between Chalmers and EPFL
Jan.-May 2001	Université de Droit, d'Economie et des Sciences d'Aix-Marseille, Institut d'Etudes Francaises pour Etudiants Etrangers, Aix-en-Provence, France French grammar, history and translation
Aug.-Dec.-2000	Dublin City University Language Services, Dublin, Ireland Cambridge's Certificate of Proficiency in English
June 2000	Fässbergsgymnasiet, Möndal, Sweden Graduation from "Natur"(Science)-program

Professional History

Aug. 2006 – Pres.	PhD student Physical Chemistry, Technische Universität München, Munich, Germany
April 2006 – Oct.2006	Intern, Linde AG, Munich, Germany
Aug. 2005 – Sep. 2005	Paramedic, Göteborgs Stad AB – Göteborg, Sweden
June 2004 – Aug. 2004	Paramedic, Göteborgs Stad AB – Göteborg, Sweden
June 2003 – Aug. 2003	Paramedic, Göteborgs Stad AB – Göteborg, Sweden

Pedagogical Merits

2007-2009	Laboratory assistant in the course "Physikalische Chemie I+II"

Publications and Presentations

Articles

1. "Investigation of the Oxygen Reduction Activity of non-Platinum Catalysts - a RDE Methodology"
   Wiberg, G. K. H.; Mayhofer, K.; Arenz, M. *ECS Transactions* **2009**, *19, 37.*

2. "Fuel cell catalyst degradation on the nanoscale",
   Mayrhofer, K. J. J.; Meier, J. C.; Ashton, S. J.; Wiberg, G. K. H.; Kraus, F.; Hanzlik, M.; Arenz, M. *Electrochemistry Communications* **2008**, *10*, 1144.

3. "Non-destructive transmission electron microscopy study of catalyst degradation under electrochemical treatment"
   Mayrhofer, K. J. J.; Ashton, S. J.; Meier, J. C.; Wiberg, G. K. H.; Hanzlik, M.; Arenz, M. *Journal of Power Sources* **2008**, *185*, 734.

4. "Analysis of the Impact of Individual Glass Constituents on Electrocatalysis on Pt Electrodes in Alkaline Solution"
   Mayrhofer, K. J. J.; Crampton, A. S.; Wiberg, G. K. H.; Arenz, M. *Journal of The Electrochemical Society* **2008**, *155*, P78.

5. "Impact of Glass Corrosion on the Electrocatalysis on Pt Electrodes in Alkaline Electrolyte"
   Mayrhofer, K. J. J.; Wiberg, G. K. H.; Arenz, M. *Journal of The Electrochemical Society* **2008**, *155*, P1.

Conference abstract

6. "Investigation of the Oxygen Reduction Reaction Activity of Non-platinum Catalyst: A RDE Methodology". Presentation at 216th ECS Meeting in Vienna. Austria, **2009**,
   Wiberg, G. K. H.; Mayhofer, K. J. J.; Arenz M

7. "Electroreduction of oxygen (ORR) in alkaline medium on silver nano particles" Poster presentation at "Electrochemistry: Crossing Boundaries" meeting in Giessen, Germany, **2008**
   Wiberg, G. K. H.; Mayhofer, K. J. J.; Arenz M

8. "Electrocatalysis on Size-Selected Cluster". Poster presentation at the "Symposium on Size Selected Clusters" in Brand, Austria, **2007**,
   Mayrhofer, K. J. J.; Wiberg, G. K. H.; Arenz, M